

# First-principles electronic theory of non-collinear magnetic order in transition-metal nanowires

submitted by

**Muhammad Tanveer**

Lahore, Pakistan

Dissertation to fulfil the requirement for the doctoral degree

Doktor der Naturwissenschaften

(Dr. rer. nat)

Department of Theoretical Physics

Faculty of Mathematics and Natural Sciences

University of Kassel, Germany

Supervisor:

Prof. Dr. Gustavo M. Pastor

Submission date: August 2014

Defence date: 9<sup>th</sup> december 2014

# Ehrenwörtliche Erklärung

Hiermit versichere ich, dass ich die vorliegende Dissertation selbstständig, ohne unerlaubte Hilfe Dritter angefertigt und andere als die in der Dissertation angegebenen Hilfsmittel nicht benutzt habe. Alle Stellen, die wörtlich oder sinngemäß aus veröffentlichten oder unveröffentlichten Schriften entnommen sind, habe ich als solche kenntlich gemacht. Dritte waren an der inhaltlich-materiellen Erstellung der Dissertation nicht beteiligt; insbesondere habe ich hierfür nicht die Hilfe eines Promotions beraters in Anspruch genommen. Kein Teil dieser Arbeit ist in einem anderen Promotions- oder Habilitationsverfahren verwendet worden.

Muhammad Tanveer

August 2014, Kassel

*To my mother, brothers and sisters, and my  
nephew M. Sajid*

---

## Abstract

The structural, electronic and magnetic properties of one-dimensional  $3d$  transition-metal (TM) monoatomic chains having linear, zigzag and ladder geometries are investigated in the frame-work of first-principles density-functional theory. The stability of long-range magnetic order along the nanowires is determined by computing the corresponding frozen-magnon dispersion relations as a function of the "spin-wave" vector  $\vec{q}$ . First, we show that the ground-state magnetic orders of V, Mn and Fe linear chains at the equilibrium interatomic distances are non-collinear (NC) spin-density waves (SDWs) with characteristic equilibrium wave vectors  $\vec{q}$  that depend on the composition and interatomic distance. The electronic and magnetic properties of these novel spin-spiral structures are discussed from a local perspective by analyzing the spin-polarized electronic densities of states, the local magnetic moments and the spin-density distributions for representative values  $\vec{q}$ . Second, we investigate the stability of NC spin arrangements in Fe zigzag chains and ladders. We find that the non-collinear SDWs are remarkably stable in the biatomic chains (square ladder), whereas ferromagnetic order ( $q = 0$ ) dominates in zigzag chains (triangular ladders). The different magnetic structures are interpreted in terms of the corresponding effective exchange interactions  $J_{ij}$  between the local magnetic moments  $\mu_i$  and  $\mu_j$  at atoms  $i$  and  $j$ . The effective couplings are derived by fitting a classical Heisenberg model to the *ab initio* magnon dispersion relations. In addition they are analyzed in the framework of general magnetic phase diagrams having arbitrary first, second, and third nearest-neighbor (NN) interactions  $J_{ij}$ .

The effect of external electric fields (EFs) on the stability of NC magnetic order has been quantified for representative monoatomic free-standing and deposited chains. We find that an external EF, which is applied perpendicular to the chains, favors non-collinear order in V chains, whereas it stabilizes the ferromagnetic (FM) order in Fe chains. Moreover, our calculations reveal a change in the magnetic order of V chains deposited on the Cu(110) surface in the presence of external EFs. In this case the NC spiral order, which was unstable in the absence of EF, becomes the most favorable one when perpendicular fields of the order of  $0.1 \text{ V/\AA}$  are applied.

As a final application of the theory we study the magnetic interactions within monoatomic TM chains deposited on graphene sheets. One observes that even weak chain substrate hybridizations can modify the magnetic order. Mn and Fe chains show incommensurable NC spin configurations. Remarkably, V chains show a transition from a spiral magnetic order in the freestanding geometry to FM order when they are deposited on a graphene sheet. Some TM-terminated zigzag graphene-nanoribbons, for example V and Fe terminated nanoribbons, also show NC spin configurations. Finally, the magnetic anisotropy energies (MAEs) of TM chains on graphene are investigated. It is shown that Co and Fe chains exhibit significant MAEs and orbital magnetic moments with in-plane easy magnetization axis. The remarkable changes in the magnetic properties of chains on graphene are correlated to charge transfers from the TMs to NN carbon atoms. Goals and limitations of this study and the resulting perspectives of future investigations are discussed.

## Zusammenfassung

In dieser Arbeit werden die elektronischen und magnetischen Eigenschaften von eindimensionalen monoatomaren  $3d$  Übergangsmetall-Ketten mit linearer, 'zigzag' und Leiter-Geometrie im Rahmen der *ab initio* Dichtefunktionaltheorie untersucht. Die Stabilität der langreichweitigen magnetischen Ordnung entlang der Nanoketten wird bestimmt durch Berechnung der Dispersionsrelationen fixierter Magnonen als Funktion des Spinwellenvektors  $\vec{q}$ . Als erstes zeigen wir, dass die magnetische Ordnung des Grundzustands der vollständig relaxierten linearen V-, Mn- und Fe-Ketten nichtkollineare (NC) Spindichtewellen (SDW) sind. Die zugehörigen charakteristischen Gleichgewichts-Wellenvektoren  $\vec{q}$  hängen von der Komposition und der interatomaren Abstände ab. Die elektronischen und magnetischen Eigenschaften dieser neuartigen spiralen Spinstrukturen werden aus der lokalen Perspektive diskutiert unter Berücksichtigung der spinpolarisierten elektronischen Zustandsdichten, der lokalen magnetischen Momente und der Spindichteverteilung für repräsentative Werte von  $\vec{q}$ . Als zweites wird die Stabilität der NC Spin-Anordnungen in Fe-Ketten mit zigzag und Leiter-Geometrie untersucht. Wir zeigen, dass die nichtkollinearen SDW in zweiatomigen Ketten (quadratische Leiter-Geometrie) bemerkenswert stabil sind, während die ferromagnetische Ordnung ( $q = 0$ ) in den zigzag Ketten (dreieckige Leiter-Geometrie) dominiert.

Die verschiedenen magnetischen Strukturen werden mittels der effektiven Austauschwechselwirkungen  $J_{ij}$  zwischen den lokalen magnetischen Momenten  $\mu_i$  und  $\mu_j$  an Atomen  $i$  und  $j$  diskutiert. Die effektiven Kopplungen werden durch Anpassung eines klassischen Heisenberg-Modells an die *ab-initio* Magnon-Dispersionsrelationen abgeleitet. Außerdem werden die magnetischen Strukturen im Rahmen allgemeiner magnetischer Phasendiagramme als Funktion erst-, zweit- und drittnächster Nachbar (NN) Wechselwirkungen  $J_{ij}$  analysiert.

Die Wirkung äußerer elektrischer Felder (EF) auf die Stabilität von NC magnetischen Ordnungen konnte für repräsentative monoatomare freistehende und deponierte Ketten quantitativ bestimmt werden. Es wird gezeigt, dass in V-Ketten ein externes senkrecht zu den Ketten angelegtes EF eine nichtkollineare Ordnung begünstigt, während es in Fe-Ketten die ferromagnetische (FM) Ordnung stabilisiert. Darüberhinaus zeigen unsere Berechnungen eine Änderung der magnetischen Ordnung von V-Ketten deponiert auf Cu(110) Oberflächen in Anwesenheit eines äußeren EF. In diesem Fall wird die für monoatomare V-Ketten instabile spirale Ordnung bei Anlegen eines senkrechten externen EF der Größe  $0.1 \text{ V/\AA}$  die energetisch günstigste.

Als eine Anwendung der Theorie haben wir die magnetischen Wechselwirkungen innerhalb monoatomarer Übergangsmetall-Ketten deponiert auf Graphen studiert. Wir haben festgestellt, dass selbst schwache Hybridisierungen zwischen Kette und Substrat die magnetische Ordnung der Kettenatome modifizieren können. Mn- und Fe-Ketten zeigen inkommensurable NC-Spinkonfigurationen. Auffällig ist der Übergang in V von einer spiralen magnetischen Ordnung in freistehenden Ketten zu einer FM Ordnung in Ketten, die auf Graphenmonolagen deponiert werden. Einige Übergangsmetall-Graphen-zigzag-Nanobänder, wie z.B. V-

und Fe-Nanobänder, zeigen ebenfalls NC-Spinkonfigurationen.

Ergänzend werden die magnetischen Anisotropieenergien (MAE) von Übergangsmetall-Ketten auf Graphen untersucht. Unsere Berechnungen zeigen, dass Co- und Fe-Ketten signifikante MAE und Bahndrehimpulse besitzen, wobei die leichte Magnetisierungsachse entlang der Kettenrichtung orientiert ist. Die bemerkenswerten Änderungen der magnetischen Eigenschaften von Ketten auf Graphen werden dem Ladungstransfer von den Übergangsmetallen zu den NN C-Atomen zugeordnet. Abschließend werden die Grenzen dieser Studie und die sich ergebenden Perspektiven für zukünftige Untersuchungen diskutiert.

## Acknowledgement

At the end of my work i would like to thank all those who have supported me during my PhD studies:

First of all I would like to thank Prof. Gustavo M. Pastor whose guidance in this work and opportunity to make my PhD at University of Kassel. Special thanks to Prof. J. Dorantes-Dávila for helpful discussions, encouragement on my ideas, and pleasant time in Kassel.

I thank Dr. P. Ruiz-Díaz who always welcome my technical problems whenever I needed. I am very grateful to Dr J. Luis Ricardo Chavez for useful discussions. Many thanks to Dr. Waldemar Töws who helped me in reading and improving some part of my thesis. Special thanks to my colleague Lucila M. Juárez for her great company and my group members for the great time.

I would like to acknowledge our secretaries Andrea Wecker and Katherina Wedemeyer for their invaluable help on all the administrative tasks.

I acknowledge the to IT-service center of University of Kassel for computational facilities and the Deutscher Akademischer Austauschdienst (DAAD) for financial support during my studies.

The last, but most important one is my dear mother, I would like to thank for her prayers and patience. I also thank my sister (Dr. I. Khanum) for financial and moral support, especially in the beginning of my PhD study.





# Contents

	<b>Page</b>
<b>Contents</b>	<b>x</b>
<b>List of Figures</b>	<b>x</b>
<b>List of Tables</b>	<b>xiv</b>
<b>1 Introduction</b>	<b>1</b>
<b>2 The quantum many-body problem</b>	<b>9</b>
2.1 Historical background . . . . .	9
2.2 Density functional theory: Fundamental concepts . . . . .	12
2.2.1 The Hohenberg-Kohn theorems . . . . .	13
2.2.2 The Kohn-Sham method . . . . .	14
2.2.3 Exchange and correlational functionals . . . . .	17
2.3 Numerical implementation of DFT . . . . .	21
2.3.1 Planewaves and Bloch theorem . . . . .	21
2.3.2 Pseudopotentials: Numerical methods of solving the Kohn-sham equations . . . . .	22
2.3.3 The Hellmann-Feynman theorem . . . . .	25

2.4	Calculation Tool . . . . .	26
<b>3</b>	<b>Theory of magnetism in transition metal nanostructures</b>	<b>29</b>
3.1	Noncollinear magnetic order in density functional theory . . . . .	29
3.1.1	Spin spiral . . . . .	30
3.1.2	Constrained magnetic moments . . . . .	32
3.1.3	Generalized Bloch theorem . . . . .	33
3.2	The classical Heisenberg model . . . . .	34
3.2.1	Effective interactions between local magnetic moments . . . . .	35
3.2.2	Magnetic phase diagrams . . . . .	36
3.3	Spin-orbit interaction . . . . .	39
3.3.1	Magnetic anisotropy energy . . . . .	40
3.4	External electric fields . . . . .	41
3.5	Technical details . . . . .	43
<b>4</b>	<b>Spiral spin-density waves in 3d transition-metal monoatomic chains</b>	<b>45</b>
4.1	Introduction . . . . .	45
4.2	Simulation model and Computational details . . . . .	47
4.3	Interplay between magnetic and electronic properties . . . . .	49
4.3.1	V monoatomic chains . . . . .	49
4.3.2	Mn monoatomic chains . . . . .	54
4.3.3	Fe monoatomic chains . . . . .	58
4.4	Magnetic phase diagrams . . . . .	64
4.5	Conclusions . . . . .	66
<b>5</b>	<b>Noncollinear magnetic orders and spin-wave spectra of Fe chains</b>	<b>69</b>
5.1	Introduction . . . . .	69
5.2	Models of SDWs in chains and ladders . . . . .	71

---

5.2.1	Structural properties . . . . .	72
5.2.2	Spin-density wave spectra . . . . .	74
5.2.3	Local electronic structure . . . . .	76
5.2.4	Effective magnetic interactions . . . . .	82
5.3	Summary . . . . .	85
<b>6</b>	<b>Tuning spin-density waves in chains by means of external electric fields</b>	<b>87</b>
6.1	Introduction . . . . .	87
6.2	Theoretical background . . . . .	89
6.2.1	Electronic calculations . . . . .	89
6.3	Spin-density wave spectra . . . . .	90
6.3.1	Vanadium chains . . . . .	90
6.3.2	Iron chains . . . . .	96
6.4	Vanadium chains deposited on Cu(110) surface . . . . .	99
6.4.1	Charge and magnetization densities . . . . .	101
6.5	Conclusion . . . . .	103
<b>7</b>	<b>Noncollinear magnetism in 3d transition metal chains on graphene</b>	<b>105</b>
7.1	Introduction . . . . .	106
7.2	Computational details . . . . .	108
7.3	Structural and electronic properties of TM chains deposited on the graphene and terminated nanoribbons . . . . .	111
7.4	Spin-density wave spectra . . . . .	117
7.4.1	Vanadium chains . . . . .	117
7.4.2	Maganese chains . . . . .	119
7.4.3	Iron chains . . . . .	119
7.5	Spin-orbit coupling effects . . . . .	122

7.6 Conclusions . . . . . 124

**Bibliography** . . . . . **125**

# List of Figures

1.1	STM image of finite biatomic Fe chains on the $(5 \times 1)$ -Ir surface . . . .	2
1.2	STM image of linear Mn chains containing 10 atoms on an insulating .	3
1.3	Spin-resolved STM image of spin spiral density wave in bi-atomic Fe chains . . . . .	5
2.1	Illustration of the spatial coordinates of the electrons and nuclei . . . .	10
3.1	Illustration of a spin spirals with spin-rotation axis perpendicular . . . .	31
3.2	Illustration of two different possibilities of flat spiral spin-density wave in a linear chain having a wave vector $\vec{q} = (0, 0, \pi/2a)$ : (a) using a large	34
3.3	Magnetic phase diagram of the 1D Heisenberg model having first and second NN interactions $J_{01}$ and $J_{02}$ , . . . . .	37
3.4	Magnetic phase diagram of the 1D Heisenberg model having first, second and third NN interactions $J_{01}$ , $J_{02}$ and $J_{03}$ , . . . . .	38
3.5	Magnetization $\vec{M}$ direction in terms of the polar angle $\theta$ and azimuthal	40
3.6	Illustration of a unit cell under the influence of the external electric field	42
4.1	Illustration of a spiral spin-density wave having a wave vector $\vec{q} = (0, 0, \pi/4a)$ with periodic length $ \lambda  = 8a$ . . . . .	48
4.2	(a) Frozen-magnon dispersion relation $\Delta E(q) = E(q) - E(0)$ of infinite V chains. The symbols refer to the <i>ab initio</i> results and the . . . . .	50
4.3	The variation of the magnitude of the local magnetic moments $\mu$ . . . .	51

4.4	Local $d$ -electron density of states (DOS) $\rho_{i\sigma}^d(\varepsilon)$ of free-standing V chains having NN distance . . . . .	52
4.5	The magnetization density $\vec{m}$ profile of spin spiral structure with wave vector . . . . .	54
4.6	(a) Frozen-magnon dispersion relation $\Delta E(q) = E(q) - E(0)$ of infinite Mn chains . . . . .	55
4.7	Local $d$ -electron density of states $\rho_{i\sigma}^d(\varepsilon)$ of free-standing Mn chains at a NN distance $a = 2.5 \text{ \AA}$ , . . . . .	57
4.8	Integrated density of states (DOS) of free-standing Mn monoatomic chains	58
4.9	(a) Frozen-magnon dispersion relation $\Delta E(q) = E(q) - E(0)$ of infinite Fe	59
4.10	The variation of the magnitude of the local magnetic moments $\mu$ . . . . .	60
4.11	Local $d$ -electron density of states (DOS) $\rho_{i\sigma}^d(\varepsilon)$ of free-standing Fe chains having NN distance $a = 2.25 \text{ \AA}$ . . . . .	61
4.12	The first and third panels display the $x$ - and $z$ -components of magnetization density ( $m_x$ and $m_z$ ) . . . . .	63
4.13	Magnetic phase diagram of the classical one-dimensional Heisenberg model with first and second NN interactions $J_{01}$ and $J_{02}$ . . . . .	64
4.14	Magnetic phase diagram of the classical Heisenberg model having first, second, and third NN interactions $J_{01}$ , $J_{02}$ and $J_{03}$ . . . . .	65
5.1	Illustration of the wire structures and magnetic orders corresponding to a spin-wave vector $\vec{q} = (0, 0, \pi/4a)$ : (a) linear chain . . . . .	72
5.2	(a) Binding energy of zig-zag (ZZ) Fe chains as a function of the lattice parameter $a$ . . . . .	74
5.3	Frozen-magnon dispersion relation $\Delta E(q) = E(q) - E(0)$ (upper panels) and local magnetic moments $\mu$ . . . . .	75
5.4	Local $d$ -electron density of states (DOS) $\rho_{i\sigma}^d(\varepsilon)$ of free-standing zig-zag (ZZ) Fe chains with periodic noncollinear (PNC) . . . . .	78
5.5	Local $d$ -electron density of states (DOS) $\rho_{i\sigma}^d(\varepsilon)$ of free-standing zig-zag (ZZ) Fe chains with alternative noncollinear (ANC) . . . . .	79
5.6	Local $d$ -electron density of states (DOS) $\rho_{i\sigma}^d(\varepsilon)$ of free-standing Fe rectangular ladders (RLs) at the equilibrium lattice . . . . .	80

5.7	Effective exchange interactions $J_{0\delta}$ in Fe wires between a local moment $\hat{\mu}_0$ its $\delta$ th nearest neighbors . . . . .	83
5.8	Magnetic phase diagram of the classical one-dimensional Heisenberg model with first and second NN interactions . . . . .	84
6.1	Illustration of the geometry and coordinate system for a spin spiral having $\vec{q} = (\pi/4a, 0, 0)$ . The uniform electric field $E_z$ . . . . .	89
6.2	Binding energy $E_B$ of one-dimensional V chains in the presence of the electric field . . . . .	91
6.3	(a) Magnon dispersion relation $\Delta E(q) = E(q) - E(0)$ in V chains for different values of the applied electric field. The lattice parameter $a = 2.6 \text{ \AA}$ . . . . .	92
6.4	a) Magnon dispersion relation $\Delta E(q) = E(q) - E(0)$ in V chains for different values of the applied electric field. The lattice parameter $a = 2.05 \text{ \AA}$ . . . . .	93
6.5	Spin-polarized 3d-electron local density of states (DOS) of V chains at the FM equilibrium NN distance $2.6 \text{ \AA}$ . . . . .	94
6.6	(a) Magnon dispersion relation $\Delta E(q) = E(q) - E(0)$ in Fe chains . . . . .	96
6.7	The local magnetic moment $\mu$ within WS as a function of the electric field. . . . .	97
6.8	Spin-polarized 3d-electron local density of states (DOS) of Fe chains at . . . . .	98
6.9	Effective exchange couplings $J_{0\delta}$ between the local magnetic moments in V chains deposited on the Cu(110) . . . . .	100
6.10	Spin-polarized 3d local density of states (DOS) of V chains deposited on the Cu(110) . . . . .	101
6.11	Difference between the spatial distribution of the screening charge densities: (a) $\Delta\rho = \rho(-0.75) - \rho(0)$ . . . . .	102
6.12	Average screened charge density difference, $\Delta\rho_{\text{avg}} = \rho(E_z) - \rho(0)$ , in a . . . . .	103
7.1	Relaxed atomic structures of TM chains deposited on a graphene sheet: I side view . . . . .	109

---

7.2	The variation of binding energy $E_B$ of TM chains at different adsorption positions such as . . . . .	112
7.3	Total and local $d$ -electron density of states $\rho_{i\sigma}^d(\varepsilon)$ of a V chain . . . . .	115
7.4	Total and local $d$ -electron density of states $\rho_{i\sigma}^d(\varepsilon)$ of Fe and Co chains . . . . .	116
7.5	Frozen-magnon dispersion relation of a V chain on the graphene . . . . .	118
7.6	Frozen-magnon dispersion relation of a Mn chain on the graphene . . . . .	120
7.7	Frozen-magnon dispersion relation of a Fe chain on the graphene . . . . .	121



# List of Tables

7.I	Magnetic orders (FM and AF), distances between the TM chains and carbon atoms of graphene $d_{TM-C}$ , local moments $\mu$ of . . . . .	114
7.II	Magnetic order, magnetic anisotropy energies $\Delta E^{xz}$ and $\Delta E^{yz}$ , spin and orbital moments of $3d$ TM chains . . . . .	123



# Introduction

Over the past two decades, a significant experimental and theoretical effort has been devoted to understand the magnetism of the low-dimensional nanostructures such as small particles, one-dimensional (1D) atomic wires [1–4] and two-dimensional (2D) islands of various sizes grown on magnetic and nonmagnetic substrates [5–7]. The electronic and magnetic properties of these nanostructures are quite different from those of bulk solid materials because of the reduction in coordination number and dimensionality, as well as consequence of size-effects [8–12]. Therefore, one can expect a variety of new potential technological applications in high-density magnetic recording, memory storage, magnetic tunnel junctions (MTJ) and spintronic devices [13,14]. Experimentally, the fabrication of low-dimensional nanostructures is obviously a very challenging task. Modern methods to prepare such magnetic systems have made it possible to investigate the influence of reduced dimensionality on the magnetic properties. In fact, there are many techniques to construct low-dimensional nanostructures on metal surface. In particular one should mention scanning-tunneling-microscopy (STM) tip-manipulation [15], self-organization processes on vicinal and flat surfaces [1], and break junctions.

In a pioneering experiment, Gambardella *et al.* have grown self-organized monoatomic Co wires at step edges of the Pt(997) vicinal surface [1]. One of the STM images of such chains is reproduced in Fig. 1.1 (a). X-ray magnetic circular dichroism (XMCD) spectra have been recorded in order to explore the magnitude of both spin and orbital magnetic moments. They demonstrated long-range ferromagnetic (FM) order in Co chains below a blocking temperature  $T_B = 15$  K. The stability of FM order was explained by the large observed values of the magnetocrystalline anisotropy energy (MAE) of the order of 2 meV/Co atom. Moreover, important enhancements of the local spin moments at the Co atoms, from  $\mu_s = 1.57 \mu_B$  (bulk) to  $2.08 \mu_B$ , and of the

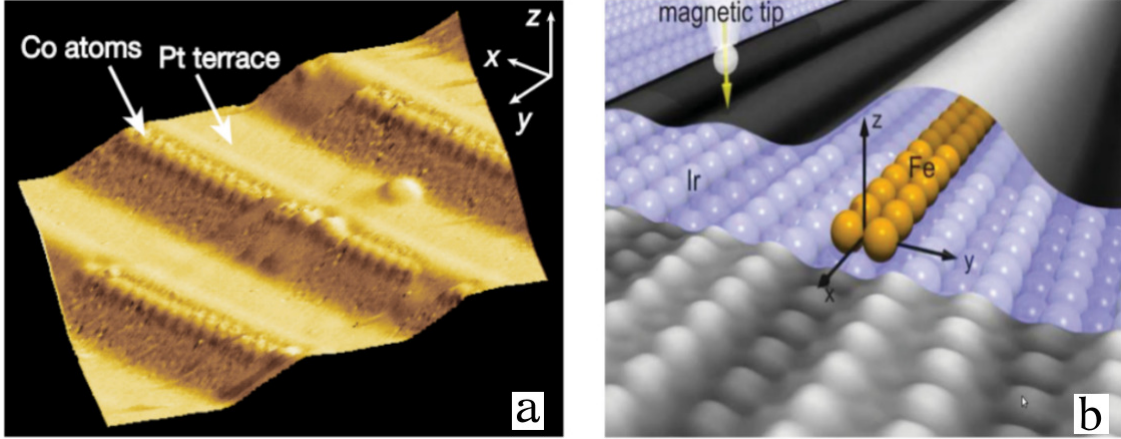


**Figure 1.1:** (a) STM image of finite biatomic Fe chains on the  $(5 \times 1)$ -Ir surface (after Ref. [1]). (b) Illustration of the magnetic order investigation of magnetic chains by using spin-polarized STM with a magnetic tip (after Ref. [36]).

local orbital moments, from  $\mu_L = 0.14 \mu_B$  (bulk) to  $0.68 \mu_B$ , were also reported. This enhancement of the local moments is attributed to the narrow  $d$ -bands of the chains as a result of localized electronic structure, which leads to a high density of electronic states near the Fermi energy. One observes that the local moments are largest for the monoatomic chains and decrease rapidly with chain width. Furthermore, increasing the lateral width of Co the chains or stripes can result in a remarkable discontinuous changes in the orientation of the easy axis, as predicted in Ref. [4].

A theoretical study N. D. Mermin and H. Wagner has shown, in the limit of Heisenberg model, that no finite-range exchange interactions can lead to long-range magnetic order in one- and two-dimensional systems at any non-zero temperature [16, 17]. However, ferromagnetism in 1D can be metastable, provided that large magnetic anisotropy energies create barriers, which effectively block the thermal fluctuations of the local moments. From a technological perspective, one of the most important and challenging problems is to understand and control how to enhance the blocking temperature of nanostructures, in order to utilize them for practical applications such as recording or storage media devices at room temperature. Additional anisotropic contributions arising from the spin orbit coupling (SOC) are needed in order to stabilize the orientation of the magnetization against thermal fluctuations. A sufficiently large value of the MAE is therefore plays a crucial role for the stability of long-range magnetic orders in 1D magnetic systems.

A further remarkable experimental study is found in Ref. [18], where linear chains having one to ten Mn atoms were constructed by using STM one-by-one atom manipulation on the  $\text{Cu}_2\text{N}/\text{Cu}(001)$  surface [see Fig. 1.2]. Spin-excitation spectra were detected by tunnelling spectroscopy and reported an AFM coupling between the Mn

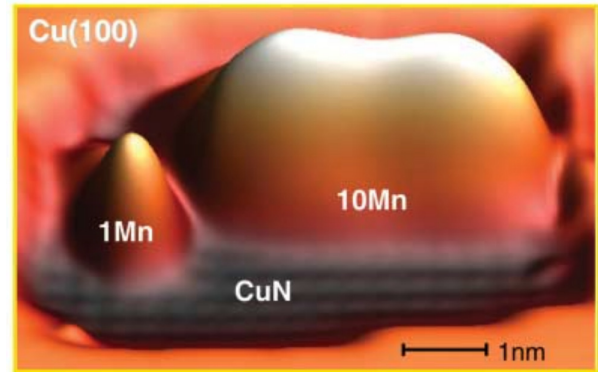


**Figure 1.2:** STM image of linear Mn chains containing 10 atoms on an insulating CuN/Cu(001) surface (after Ref. [18]).

atoms. Another experimental technique, which produces one-dimensional atomic-size chains is the so-called break junctions or mechanically controllable break junctions. In these experiments, two electrodes, which are initially in contact are pulled apart with an STM-tip. Alternatively two nano-islands on the substrates are pulling apart. In this way, it is possible to form a freestanding 1D chain or nanocontact consisting only of a few atoms (namely, 5–10 atoms). By using this method, successful chain formation has been demonstrated for late  $4d$  and  $5d$  TM elements [19].

These experimental investigations performed on atom-by-atom engineered structures have revealed a number of amazing effects such as the enhancement of orbital magnetism and magnetic anisotropy [1–4], long range magnetic order of monoatomic chains and adatoms, magnetization-reversal and spin-reorientation transitions in deposited clusters [6, 20, 21], as well as non-collinear spin arrangements, quantum confinement and self-alignment of local moments in nanowires [9–11].

Besides the well-known collinear magnetic spin configurations (e.g., ferro-, ferri- and antiferromagnetic order) a large variety of more complex noncollinear spin arrangements such as *spin spirals* and *skyrmions* can exist in solids and low-dimensional systems. Noncollinear spin arrangements are often the result of frustrations such as antiferromagnetic (AF) nearest-neighbor (NN) interactions in non-bipartite lattices or competing FM and AF interactions between atoms at different distances. Fe and Cr compounds are most prominent examples of noncollinear magnetic structure in itinerant-electron magnetic materials [22–25]. The magnetic order of Fe structures depends sensitivity on the geometrical arrangement of the Fe atoms and their environment. For instance, body-centered cubic (bcc)  $\alpha$ -Fe exhibits a spontaneous ferromagnetic order which is due to the parallel alignment of unpaired spins. In contrast, the fcc  $\gamma$  phase of Fe is a highly frustrated magnetic structure with a complex noncollinear configuration. Moreover, the ground-state magnetic order of  $\gamma$ -Fe is know to depend crucially on the lattice parameter [26].

A significant effort have been dedicated to study NC magnetism in low-dimensional nanostructures due to their fundamental interest and potential technological application. For instance, in 2D systems Mn monolayers on Ag(111) and Cr monolayers on Pd(111) show stable  $120^\circ$  Néel-phase structures due to the topological frustration on triangular lattices. Furthermore, a direct observation of the spiral magnetic order at the interface of Mn/W(100) monolayers has been investigated by using spin-polarized STM. The results suggest that the antisymmetric Dzyaloshinskii-Moriya interaction (DMI), induced by spin-orbit coupling, is a driving force for the stability of spiral magnetic structures [27]. Another studies revealed that the magnetic structure of a Mn monolayer deposited on a Fe(100)-substrate exhibits a NC spin spiral phase due to the competition between the AF coupling within the Mn-monolayer and the FM coupling at the Fe/Mn interface. Indeed, thicker Mn monolayers are coupled antiferromagnetically. In this case of NC order derives from the competing exchange interactions between the monolayer and the substrate moments, which extends over a macroscopic area [28]. Furthermore, Nakamura *et al.* predicted the formation of SDWs in free-standing Fe(110) monolayers [29].

The noncollinear structures of magnetic domain walls (DWs) are an important features of any FM materials, which have always attracted considerable experimental and theoretical attention, ever since the pioneering works of Bloch and Néel [30, 31]. Understanding the physics of noncollinear structures and DWs is crucial to numerous applications, particularly in memory devices such as hard disk, magnetic random access memory (RAM), magnetic race-track memory and spin-electronics devices, where the presence of a DW cannot be disjoined from the stored information itself. Therefore recently, the interest in noncollinear magnetism at surfaces and interfaces has increased because of their potential technological importance. Moreover, the symmetry breaking and the enhanced SOC arising from a reduced dimensionality are expected to give rise to noncollinear magnetism with new and exotic features differing from those of bulk. However, little is known quantitatively, about the detailed complexity of the spin-spiral structures in thin films. NC spiral or chiral magnetism was recently explored in domains walls i.e., in Ni/Fe/Cu(991) [32], Fe/W(110) [33], Co/Pt(111) [34], and Co/Pt [35].

Very recently, an experimental investigation by using a spin-polarized STM magnetic tip under an out-of-plane magnetic field of  $B = 2$  T at 8 K, revealed that finite Fe biatomic chains on  $(5 \times 1)$ -reconstructed Ir(001) surface, show spiral magnetic ground states [36]. The three-dimensional representation of the spin spiral in biatomic Fe chains with local magnetic moment periodicity of about three-interatomic distances ( $120^\circ$  angle between adjacent moments) is shown in Fig. 1.3 (c). This system has been further investigated in the framework of DFT in order to understand the origin of this remarkable magnetic structure. Both studies concluded that the antisymmetric

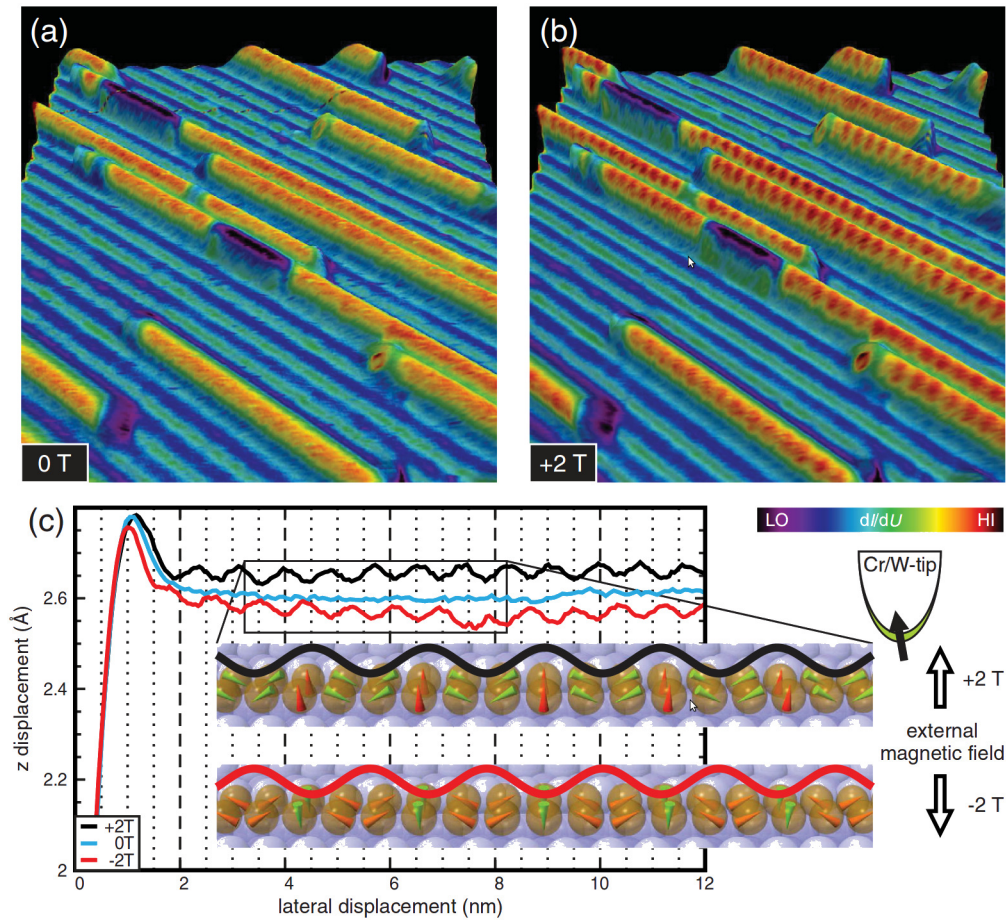


**Figure 1.3:** Spin-resolved STM image of a bi-atomic Fe chains grown on the  $(5 \times 1)$ -reconstructed Ir(001) surface. Three-dimensional representation of spin spiral density wave in biatomic Fe chains with a magnetic periodicity of about three-interatomic distances ( $120^\circ$  angle between adjacent moments). The images of the nanowires are taken in an external magnetic field  $B = 0$  T and  $B = 2$  T, respectively. This figure has been taken from Ref. [36].

Dzyaloshinskii-Moriya (DM) interactions [37–39] is the driving force behind the formation of the spin spiral. Two STM images of the Fe chains are displayed in Fig. 1.3 (a)-(b) in which the spins are correlated with a nearly fixed vector spin chirality with different values of external magnetic fields  $B$ . At  $B = 0$  T, the authors do not find any preferred magnetic direction for the spins due to thermal and dynamic fluctuations, whereas a periodic spiral magnetic patterns is observed for  $B = \pm 2$  T. Indeed, it is necessary to introduce small a value of magnetic field in order to quench the thermal fluctuations occurring in the chains with a finite numbers of Fe atoms. From a technological point of view, both infinite and finite Fe chains deposited on a metal surface could be useful for transmitting bits of magnetic information.

A significant understanding of the experimental results on 1D systems has been obtained in the framework of density-functional theory (DFT). In very recent years, a number of *ab initio* calculations using DFT seem to be successful for the description of the structural, electronic and magnetic properties of complex NC magnetic structures. For instance, Lounis *et al.* [8], using both *ab initio* results and the solution of a classical Heisenberg model, have reported the complex magnetic order in Mn-chains on a Ni(001) substrate. They found that the system is magnetically frustrated, which originates from the competing interactions between the AF coupling within the Mn-chain atoms and the FM coupling of the chain atoms with the substrate. This leads to an even-odd effect in which the magnetic ground state crucially depends on the parity of the number of Mn atoms in the linear chain. Even numbers of atoms in the linear chain exhibit the noncollinear magnetic configuration, whereas odd numbers of atoms yield a completely different magnetic order, such as collinear ferrimagnetic alignment. Very recently, theoretical investigations have been performed on the magnetic ordering of Mn nanostructures deposited on the Fe(110) substrate including the SOC interactions [7]. The authors found that long Mn wires are magnetically frustrated with a number of novel magnetic structures including helical spin spirals.

Zelený *et al.* investigated from a theoretical prospective the magnetic properties of one-dimensional Mn nanostructures with geometries varying between the straight line wire to nanorods [40]. They found that the ground-state magnetic order in monoatomic Mn chains is noncollinear as a result of competing short-range and long-range AF interactions. Saubanère *et al.* obtained that also V wires develop spontaneously a spiral SDWs, provided that the NN distance  $a$  is not too large ( $a < 2.55 \text{ \AA}$ ) [41]. In this case noncollinearity is mainly the consequence of competing FM and AF couplings between first and second NNs. Tung and Guo extended the previous studies in several respects, showing in particular that V, Mn and Fe chains have a stable spin-spiral order at the equilibrium bond length, while the local moments in Cr, Co and Ni chains remain collinear [42]. As in the previous example, the magnetic couplings between first and second NNs are found to be frustrated. More recently, Schubert *et al.* performed *ab initio* studies of noncollinear magnetism in freestanding and supported Mn chains [43]. Varying the number of the  $3d$  electrons they observe a smooth transition from AF order in pure Cr chains, through noncollinear order in Mn-rich chains, to a FM behavior in the case of pure Fe chains. In addition, supported Mn chains were found to be AF on Pd(110), whereas a weak noncollinear order is found on Cu(110) and Ag(110).

The hybridizations induced by deposition on a substrate may indeed change the magnetic couplings found in idealized monoatomic chains. Despite their potential importance, these effects are often neglected in the pioneering theoretical studies, since they represent a serious numerical challenge. Moreover, the 1D limit is a subject of



---

fundamental interest on its own. Consequently, significant research efforts are being devoted to approach the 1D behavior as closely as possible from an experimental perspective. Several works have considered the effects of substrate hybridizations on the magnetism of deposited wires [4, 36, 43–45]. In some cases, the magnetic order of the free-standing geometry is preserved after deposition, indicating that the low-dimensionality of the wire dominates over the substrate effects. In other cases, even a weak chain-surface hybridization is sufficient to drastically modify the coupling along the wire. Changes in the magnetic order from FM to AF coupling have been observed, depending on the specific structural arrangement [45].

Previous studies show that the type of substrate has a crucial influence on the magnetic order. In this context the magnetic order of TM chains on graphene is particularly interesting. Graphene is often used as a substrate due to its high room-temperature carrier-mobility [46], quantum Hall effect [47, 48] and easy growth. In addition, it is a promising candidate for the technological applications [46, 49–51]. For this reason, it is important to understand the magnetic behavior of TM wires deposited on a graphene sheet, which is relevant for recording media, magnetic inks, and magneto-electronic devices.

However, very few studies have been devoted to the stability of NC magnetic configurations in  $3d$  TM chains. It is the main goal of the present work to investigate the ground-state magnetic orders in low-dimensional systems giving a special attention to spiral SDWs in  $3d$  TM monoatomic chains from a first principles perspective. The remainder of the thesis is arranged as follows. Chapter 2 reviews the main concepts of DFT as introduced by Hohenberg, Kohn and Sham. The main approximations to the exchange and correlation functionals are described namely the local density approximation (LDA) and the generalized gradient approximation (GGA), which are applicable to the metallic systems studied in the present work. Finally, we discuss the implementation of DFT with various functionals in the Vienna *ab initio* simulation package (VASP). This code solves the Kohn-Sham (KS) equations using a plane-wave basis-set. The interaction between the valence electrons and core electrons is described by the projector augmented-wave (PAW) method.

In chapter 3 we give a short introduction of the theory of noncollinear magnetism and related elementary magnetic models. These models provide a basis for understanding the *ab initio* results. For instance, the classical Heisenberg model provides a variety of magnetic orders depends on the values of the exchange interaction  $J_{ij}$  between the local moments: collinear (FM and AF) and noncollinear orders corresponding to different strengths, signs and ranges of the parameter  $J_{ij}$ . Later on, we discuss the theory of the magnetic anisotropy energy (MAE) which is important for the stability of the magnetization direction against thermal fluctuations at finite temperatures. The final

part of this chapter deals with the effects of external electric field on the magnetic properties.

In chapter 4 we investigate the stability of various collinear and noncollinear magnetic orders by computing the frozen-magnon dispersion relations as a function of spin-wave vector  $\vec{q}$  for freestanding V, Mn, and Fe monoatomic wires. The effect of changes in the interatomic distances are considered. In order to analyze the magnetic ground states from the local prospective, the effective exchange interactions  $J_{ij}$  between the local magnetic moments are derived from the *ab initio* calculations. The results are analyzed in the framework of the classical Heisenberg model. At the end of this chapter, the magnetic phase diagrams in the vicinity of the *ab initio* derived exchange interactions are displayed, which provide a comprehensive picture of the stability of spiral SDWs in nanowires.

Symmetry and dimensionality are known to play an important role in determining the magnetic properties of TM, especially in low-dimensional, systems. Therefore, in chapter 5 we explore the ground-state magnetic properties of wires having linear, zigzag, and rectangular geometries by calculating the corresponding frozen-magnon dispersion relations as a function of spin-wave vector  $\vec{q}$ . Emphasis is given here to Fe nanowires as representative example. In chapter 6 we present the effect of an external electric field on the stability of NC magnetism in freestanding V, Mn and Fe nanowires. In addition, the effects of wire-substrate hybridization on the magnetic order of V chains deposited on Cu(110) surface are discussed.

In chapter 7 we focus on the structural, electronic, and magnetic properties of V, Cr, Mn, Fe and Co monoatomic chains deposited on a graphene sheet together with TM-terminated graphene nanoribbons (GrNRs). First, we explore the structural stability of nanowires at various positions on the graphene sheet. We find that Cr and Mn chains on graphene prefer the AF solution, while V, Fe and Co chains favor the FM order. These collinear calculations are however not conclusive in order to determine the ground-state magnetic arrangements. Therefore, we also performed noncollinear calculations and analyze the magnon dispersion relations.

Our results show that the ground-state magnetic orders of Mn and Fe chains on the graphene sheet are in fact spiral SDWs. In the case of TM-terminated GrNRs, the NC magnetic arrangements are found to be more stable in the case of V- and Fe-terminated nanoribbons. In the last part of this chapter, the spin-orbit effects are explored.

Finally, the present discussion is closed in chapter 8 with a brief summary of main conclusions and a brief outlook on challenging future developments.

# The quantum many-body problem

## 2.1 Historical background

The quantum mechanical state of a solid containing a large number of interacting particles is completely described by the many-body wavefunction  $\psi$ , which depends on the coordinates each particle.

However, the wavefunction of the system is a very complicated mathematical object which holds a large amount of information. Therefore, an exact or analytical calculation of  $\psi$  is in general impractical. In principle  $\psi$  may be obtained from the time-independent many-body Schrödinger equation, which can be written as

$$\hat{H}\psi = \varepsilon\psi, \quad (2.1)$$

where  $\hat{H}$  is the Hamiltonian,  $\psi = \psi(\vec{X}, \vec{R})$  is the electron and nuclei wavefunction, and  $\varepsilon$  is the total energy of the system. Here,  $\vec{X} = (\vec{r}_1\sigma_1, \vec{r}_2\sigma_2, \dots, \vec{r}_N\sigma_N)$  defines the spatial and spin coordinates of all electrons and  $\vec{R} = (\vec{R}_1, \vec{R}_2, \dots, \vec{R}_M)$  represents the coordinates of all nuclei. The wavefunction  $\psi$  of the system depends in total on  $4N + 3M$  variables with  $N$  being the number of electrons and  $M$  the total number of nuclei.

The total Hamiltonian operator  $\hat{H}$  for the system of  $M$  nuclei and  $N$  electrons [see Fig. 2.1] with pair interactions between the components is spin independent. It is given by:

$$\hat{H} = \hat{T}_N + \hat{T}_e + \hat{V}_{Ne} + \hat{V}_{NN} + \hat{V}_{ee} \quad (2.2)$$

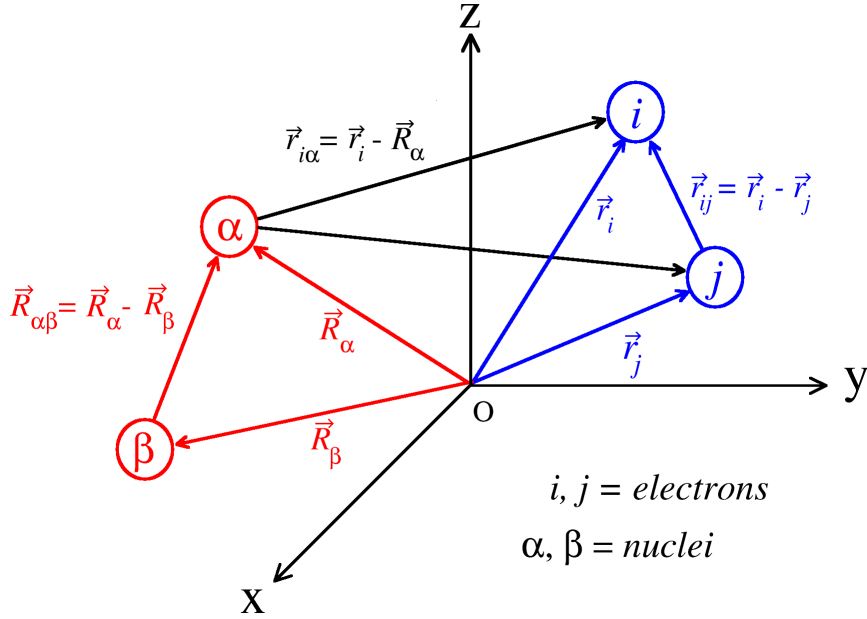


**Figure 2.1:** Illustration of the spatial coordinates of the electrons and nuclei in the system.

or<sup>1</sup>

$$\begin{aligned}
 \hat{H} = & - \sum_{\alpha=1}^M \frac{1}{2M_{\alpha}} \nabla_{\vec{R}_{\alpha}}^2 - \frac{1}{2} \sum_{i=1}^N \nabla_{\vec{r}_i}^2 - \sum_{\alpha=1}^M \sum_{i=1}^N \frac{Z_{\alpha}}{|\vec{r}_{i\alpha}|} \\
 & + \sum_{\alpha=1}^M \sum_{\beta>\alpha}^M \frac{Z_{\alpha}Z_{\beta}}{|\vec{R}_{\alpha\beta}|} + \sum_{i=1}^N \sum_{j>i}^N \frac{1}{|\vec{r}_{ij}|}, \quad (2.3)
 \end{aligned}$$

Here, the first two terms in Eq. (2.3) are the kinetic energy of the nuclei ( $\hat{T}_N$ ) and the electrons ( $\hat{T}_e$ ), respectively. The other three terms are Coulomb energies associated to the nucleus-electron attraction  $\hat{V}_{Ne}$ , the nucleus-nucleus repulsion  $\hat{V}_{NN}$ , and the electron-electron repulsion  $\hat{V}_{ee}$ , respectively. Unfortunately, it is impossible to solve the Schrödinger equation [Eq. (2.1)] exactly due to the large number of variables on which the wave function depends. For a system with  $M$  nuclei and  $N$  electrons, we have  $3M+4N$  variables, i.e. 3 position coordinates for each particle and in addition one spin coordinate for each electron. Therefore, it is unavoidable to make approximations for both the Hamiltonian and the many-body wavefunction  $\psi$ .

The first major simplification is the *Born-Oppenheimer (BO) approximation* or *adiabatic approximation* [52], which allows us to decouple the electronic and ionic degrees

<sup>1</sup>For simplicity we have used the atomic units i.e.,  $m_e = \hbar = e^2/(4\pi\epsilon_0) = 1$ . Then, the energy is given in Hartrees.

of freedom. This is justified by the large difference in mass between the electrons  $m_e$  and the ions  $M_\alpha$ . The electrons are  $10^3$  to  $10^5$  times lighter than the nuclei [52] and, therefore, the electrons move much faster than the nuclei. Consequently, the electronic and nuclear motions are decoupled within the BO approximation. Thus, the full Hamiltonian  $\hat{H}$  in Eq. (2.1) of the system can be split into two parts: electronic part  $\hat{H}_e = \hat{T}_e + \hat{V}_{Ne} + \hat{V}_{NN} + \hat{V}_{ee}$  and ionic or nuclear kinetic energy  $\hat{T}_N$ . Of course, the electronic Hamiltonian  $\hat{H}_e$  depends on the ionic coordinates  $\vec{R}_\alpha$ . However, in order to solve the electronic problem, the heavy ions are considered to be fixed particles at positions  $\vec{R}_\alpha$ . Then,  $\vec{R}_\alpha$  are treated as external parameters in  $\hat{H}_e$ , not as dynamic variables. Correspondingly, the total wavefunction  $\psi$  is also split into the following form:

$$\psi(\vec{X}, \vec{R}) = \psi_{e,\vec{R}}(\vec{X}) \chi_N(\vec{R}) \quad (2.4)$$

where  $\psi_{e,\vec{R}}(\vec{X})$  is the wave function of electrons with current nuclei positions  $\vec{R}$ , and  $\chi_N(\vec{R})$  is the wave function of nuclei. Here,  $\vec{R}$  and  $\vec{X}$  are collected all-nuclear and all-electronic coordinates, respectively.

The electronic wavefunction  $\psi_{e,\vec{R}}(\vec{X})$  is obtained by solving the schrödinger equation for the subsystem of the electronic part

$$\hat{H}_e \psi_{e,\vec{R}}(\vec{X}) = E(\vec{R}) \psi_{e,\vec{R}}(\vec{X}) \quad (2.5)$$

where

$$\hat{H}_e = -\frac{1}{2} \sum_{i=1}^N \nabla_{\vec{r}_i}^2 - \sum_{\alpha=1}^M \sum_{i=1}^N \frac{Z_\alpha}{|\vec{r}_{i\alpha}|} + \sum_{i=1}^N \sum_{j>i}^N \frac{1}{|\vec{r}_{ij}|} + \sum_{\alpha=1}^M \sum_{\beta>\alpha}^M \frac{Z_\alpha Z_\beta}{|\vec{R}_{\alpha\beta}|} \quad (2.6)$$

The energy  $E = E(\vec{R})$  depends on the fixed positions  $\vec{R}$  of the nuclei. Notice that the  $E$  not only include the pure electronic energy  $E_e = \langle \hat{T}_e + \hat{V}_{Ne} + \hat{V}_{ee} \rangle$  but the ion-ion repulsive energy  $E_{NN} = \langle \hat{V}_{NN} \rangle$ , which is a constant quantity for give static coordinates  $\vec{R}$ , i.e.,  $E = E_e + E_{NN}$ . Knowing the eigenenergies  $E(\vec{R})$  as a function of  $\vec{R}$ , in the second step of *BO* approximation the motion of nuclei are considered as moving within the potential  $E(\vec{R})$ . For this reason,  $E(\vec{R})$  is also referred to as the potential energy surface (PES). By solving the schrödinger equation

$$\left\{ \hat{T}_n + E(\vec{R}) \right\} \chi_N(\vec{R}) = \varepsilon \chi_N(\vec{R}) \quad (2.7)$$

One can in principle obtain the wavefunction  $\chi_N(\vec{R})$  of the nuclei.

It is clear that the *BO* approximation decreases the number of variables to be treated simultaneously from  $4N + 3M$  in Eq. (2.1) to  $4N$  in the electronic problem

Eq. (2.5) and  $3M$  in the nuclear problem Eq. (2.7). However, in this work we are not interested in the properties of the nuclear system except for the equilibrium bond lengths. These quantities can be directly read out from the minima of the PES and do not require a quantum mechanical treatment of the nuclear problem. In this sense, the *BO* approximation reduces the number of variables to be treated explicitly quantum mechanically to  $4N$  coordinates of the electronic system. Still, we need further approximations in order to reduce the computational burden for most practical systems. One fundamental approach to solve the electronic Schrödinger equation Eq. (2.5) numerically is the Hartree-Fock (HF) approximation [53], which transforms the many-body problem into a single-particle problem by approximating the many-body wave function  $\psi_e(\vec{r}_i\sigma_i)$  with an antisymmetrized product of single-particle wavefunctions. This product is usually referred to as a Slater determinant [54]. This ensures the antisymmetry of the wave function and the fulfillment of the Pauli principle. The HF potential approach includes the classical Coulomb energy  $E_H$  and a quantum mechanical contribution to energy known as exchange energy  $E_x$ . However, this approximation does not account for the electronic correlation. Although the latter is often smaller than the other two, it is well known that  $E_c$  is crucial to obtain accurate results. Therefore, the original Hartree-Fock approximation needs to be improved in order to take into account the correlation energy.

The most popular alternative approach to the electronic structure is density-functional theory (DFT). This remarkable theory replaces the complicated  $N$ -electron wave function and the associated Schrödinger equation by a formulation based on a much simpler mathematical object, namely the spin-polarized electron density  $n(\vec{r}, \sigma)$ . The basic of the DFT described in the following section 2.2.

## 2.2 Density functional theory: Fundamental concepts

Density-functional theory is presently the most versatile and powerful quantum mechanical approach to the many body problem, which allows us to describe larger and larger systems, as accurate as far the theory can go. This theory is based on a reputable paper of Hohenberg and Kohn, who demonstrated the existence of a bijective mapping between the ground-state density  $n(\vec{r})$  and the ground-state wavefunction [55]. Consequently, the ground-state energy and all other ground-state properties of the system (e.g. cohesive energy, lattice constant, etc.) are functionals of the ground-state electron density [56]. This implies that the much more manageable ground-state electron density  $n(\vec{r})$  replaces the wavefunction as the fundamental unknown of the problem.

This idea has been proven to be excellent and computationally simpler in all respects. Then, for the purpose of the practical calculations Kohn and Sham [57] how to replace the evaluation of the functionals of the many-electron problem into in principle exact set of self-consistent *one-electron equations*. They derived eigenvalue equations from the variational approach which are analogous to the HF equations but exact. These so-called KS equations are actually simpler to solve than the HF ones.

DFT deals with systems of identical particles [58], basically fermions, providing a simple method for describing the effects of exchange and correlation in an inhomogeneous electron gas. The minimum of the total energy  $E[n]$  as a functional of  $n(\vec{r})$  gives access to the exact energy of the system. The electronic density that yields the minimum of  $E[n]$  is in principle the exact ground-state density  $n(\vec{r})$ .

DFT has proved to be highly successful in describing structural and electronic properties of molecules and solids (including glasses and liquids) and its application to diverse systems continues to grow speedily. There are state-of-the-art applications of DFT in a wide variety of areas, including magnetism, catalysis, surface science, nanomaterials, biomaterials and geophysics [59]. DFT has been applied to degenerate ground-states [60], spin-polarized ground states [60,61], quantum Hall effect [62], etc. However, in some special cases DFT predicts fictitious results. For instance, DFT has limited accuracy in the calculation of excited states. A particularly famous example is the underestimation of band gaps in semiconductors and insulating materials [56].

Among the failures of DFT, with the functionals known nowadays, one should mention the description of weak van der Waals (vdW) forces between closed-shells systems. Although progress has been recently made on this subject [63], these more subtle problems are still beyond the reach of simple approximations to DFT. Another usual problem is that the binding energies obtained within the LDA are overestimated, as compared to experimental values. In order to get more accurate results, one needs to use well-behaved gradient-corrected functionals or include the weak vdW interactions additionally. Another field in which simple DFT approximations often fail concerns strongly correlated materials, such as NiO and FeO which are predicted to be metals by LDA-DFT in contrast to the experimental behavior, which is that of antiferromagnetic insulators [64].

### 2.2.1 The Hohenberg-Kohn theorems

DFT is based upon two remarkable theorems first demonstrated by Hohenberg and Kohn (HK) in 1964 [55]. The fundamental break through of these theorems is to formulate density functional theory as an exact theory of many-body systems.

**Theorem 1** (existence theorem)

The total energy of a many electron system in an external potential  $V_{ext}(\vec{r})$  is a unique functional of the electron charge density  $n(\vec{r})$ .

Since from the N-electron system  $V_{ext}(\vec{r})$  determines completely the system under study, i.e., the Hamiltonian,  $n(\vec{r})$  also determine the ground-state wavefunction and all other electronic properties of the ground-state such as ground-state energy. One may therefore write the energy as a function of  $n(\vec{r})$ .

$$E[n(\vec{r})] = F_{HK}[n(\vec{r})] + \int n(\vec{r}) V_{ext}(\vec{r}) d^3\vec{r} \quad (2.8)$$

where  $F_{HK} = \langle \psi[n] | \hat{T}_e + \hat{V}_{ee} | \psi[n] \rangle$  is the universal Hohenberg-Kohn functional representing the sum of kinetic and coulomb energies, while the second term describes the interaction with the external potential. For a given  $V_{ext}(\vec{r})$  an important energy minimization principle is provided by the second KH theorem.

**Theorem 2** (variational principle)

In the ground-state, the energy functional  $E[n(\vec{r})]$  has its minimum relative to all variations of the density.

$$E[n(\vec{r})] = \min E[n(\vec{r})] \iff \left. \frac{\delta E[n(\vec{r})]}{\delta n(\vec{r})} \right|_{n(\vec{r})=n_0(\vec{r})} = 0 \quad (2.9)$$

Despite the general validity of the Hohenberg-Kohn theorems, they do not provide us with any useful computational scheme for calculating the ground-state density, because the exact form of the functional  $F_{HK}[n(\vec{r})]$  is unknown. About one year later, Kohn and Sham developed an important scheme for carrying out DFT calculations, which offers a way for getting  $E[n(\vec{r})]$ , which is formally exact provided that one has access to  $F_{HK}[n(\vec{r})]$ . In other words, once the Kohn-Sham method is set, all the approximation of the theory can be traced back to the approximation of the universal functional  $F_{HK}$ . Knowing that  $F_{HK}$  is universal i.e., independent of the system under study, one may hope that simple approximation are possible.

**2.2.2 The Kohn-Sham method**

Kohn and Sham (KS) reformulated the problem in a simpler, more explicit, form and thus opened the way to practical applications of DFT. The KS formulation is based on mapping the full interacting electronic system onto a fictitious non-interacting system,



so that the minimization of  $E[n]$  with respect to  $n(\vec{r})$  can be transformed into a set of self-consistent single-particle equations.

The KS scheme replaces the difficult interacting many-particles system by an auxiliary system of non-interacting particles moving within the potential  $V_s$  in such a way that the ground-state density  $n_s(\vec{r})$  of the single-particle system matches exactly the ground-state density  $n(\vec{r})$  of the interacting system. The auxiliary single-particle Schrödinger equation is given by

$$\left(-\frac{1}{2}\nabla^2 + V_s(\vec{r})\right) \psi_i(\vec{r}) = \varepsilon_i \psi_i(\vec{r}). \quad (2.10)$$

Since the ground-state density of the auxiliary system of  $N$  non-interacting electrons is a single Slater determinant, its density is given by a sum over the  $N$  lowest occupied KS orbital densities  $|\psi(\vec{r})|$

$$n(\vec{r}) = \sum_{i=1}^N |\psi_i(\vec{r})|^2. \quad (2.11)$$

The crucial idea of the KS method is to approximate the kinetic energy of the interacting system  $T_s[n]$  by the kinetic energy of the non-interacting electrons occupying KS orbitals  $\psi_i(\vec{r})$ :

$$T_s[n] = \sum_i \int \psi_i^*(\vec{r}) \left(-\frac{1}{2}\nabla^2\right) \psi_i(\vec{r}) d\vec{r}. \quad (2.12)$$

This has been found to be a very accurate approximation. Then, the KS total energy functional for a set of occupied electronic states  $\psi_i$  can be written as

$$E[n] = T_s[n] + E_H[n] + E_{xc}[n] + E_{ext}[n]. \quad (2.13)$$

Here,  $E_H[n]$  is the classical Hartree electron-electron repulsion

$$E_H[n] = \int \int \frac{n(\vec{r})n(\vec{r}')}{|\vec{r} - \vec{r}'|} d\vec{r} d\vec{r}' \quad (2.14)$$

and  $E_{ext}[n]$  takes into account the interaction between the electrons and the external field  $V_{ext}(\vec{r})$  generated by the ions or by any other source:

$$E_{ext}[n] = \int V_{ext}(\vec{r}) n(\vec{r}) d\vec{r}. \quad (2.15)$$

All other contribution to the total energy are described by so-called *exchange* and *correlation energy*  $E_{xc}[n]$ , written as

$$E_{xc}[n] = F_{HK}[n] - T_s[n] - F_H[n] \quad (2.16)$$

If the *exchange* and *correlation energy* would be known, one would be able to calculate the ground state energy and density of the many-body electron system exactly by solving the single-particle KS equations self-consistently.

According to the Hohenberg-Kohn theorem, the density  $n(\vec{r})$  that minimizes the functional  $E[n]$  is the ground-state density. Taking the variation of Eq. (2.13) with respect to the particle density leads to a set of self-consistent one-electron equations for the orbitals  $\psi_i(\vec{r})$ . The resulting KS equations are given by

$$\left( -\frac{1}{2}\nabla^2 + \int \frac{n(\vec{r}')}{|\vec{r} - \vec{r}'|} d^3r' + V_{ext}(\vec{r}) + \frac{\delta E_{xc}[n(\vec{r})]}{\delta n(\vec{r})} \right) \psi_i(\vec{r}) = \varepsilon_i \psi_i(\vec{r}). \quad (2.17)$$

The KS equations describe electrons moving in the one-electron potential

$$V_{eff}(\vec{r}) = V_{ext}(\vec{r}) + \int \frac{n(\vec{r}')}{|\vec{r} - \vec{r}'|} d^3r' + V_{xc}[n(\vec{r})], \quad (2.18)$$

where

$$V_{xc}[n(\vec{r})] = \frac{\delta E_{xc}[n(\vec{r})]}{\delta n(\vec{r})}. \quad (2.19)$$

is the functional derivative of the exchange-correlation energy  $E_{xc}$  with respect to the density.  $V_{eff}(\vec{r})$  is nothing but the effective potential  $V_s(\vec{r})$  required in order that the non-interacting system yields the exact ground-state  $n(\vec{r})$ .

The KS equations must be solved self-consistently. One first chooses an initial trial shape of the function  $n(\vec{r})$  and substitutes it into Eq. (2.18) in order to find  $V_{eff}(\vec{r})$ . One then solves Eq. (2.10) for the single-particle wavefunctions  $\psi_i(\vec{r})$  and uses Eq. (2.11) to find the next iteration for  $n(\vec{r})$ . The solution for  $n(\vec{r})$  has been found when this procedure has been repeated a sufficient number of times so that no further changes occur in the charge density  $n(\vec{r})$ . Then, the resulting  $\phi_i(\vec{r})$  not only satisfy the Schrödinger equation for the reference non-interacting electrons, but also the derived  $n(\vec{r})$  coincides with the exact ground state density of the interacting system.

### 2.2.3 Exchange and correlational functionals

The KS density-functional theory [57] is widely used for self-consistent field electronic-structure calculations of the ground-state properties of atoms, molecules, and solids. As described above, the crucial contributions of the exchange and correlation are incorporated by means of the exchange-correlation energy functional  $E_{xc}[n]$  or, equivalently, its functional derivative  $V_{xc}[n]$ . In general, the functional of  $E_{xc}[n]$  is given by integral form

$$E_{xc}[n] \equiv \int n(\vec{r}) \varepsilon_{xc}(n(\vec{r}), \nabla n(\vec{r}), \dots) d\vec{r} \quad (2.20)$$

where exchange-correlation energy density  $\varepsilon_{xc}$  is same function of  $n(\vec{r})$  at position  $\vec{r}$ , its equivalent  $\nabla n(\vec{r})$ , and so forth. One expect that  $E_{xc}[n(\vec{r})]$  or its functional derivate  $V_{xc}[n(\vec{r})]$  can be written as an expansion over the gradients to arbitrary order of the density:

$$V_{xc}[n(\vec{r})] = V_{xc}[n(\vec{r}), \nabla n(\vec{r}), \nabla(\nabla n(\vec{r})), \dots]. \quad (2.21)$$

In other words, the general value of exchange-correlation energy potential  $V_{xc}$  at the point  $\vec{r}$  depends not only on the value of the density at that position  $\vec{r}$ , but also on the variations of  $n(\vec{r})$  around  $\vec{r}$ .

However, the exact form of the potentials  $E_{xc}[n]$  and  $V_{xc}[n]$  are unknown. For this reason, approximations to the exchange-correlation potential  $V_{xc}[n]$  as a function of the electron density  $n(\vec{r})$  are involved in DFT applications. In fact, these approximations turn out to be the central importance for the accuracy of the DFT calculations. Probably the simplest way is to approximate the  $V_{xc}[n]$  for homogeneous electron gas, which is know and depends only on the value of the density  $n(\vec{r})$  at position  $\vec{r}$ . This lead to the LDA in which gradient and high-orders contributions of the density to the potential  $V_{xc}$  are neglected. For non-homogeneous systems having a non-uniform electron density the LDA can be improved by including density gradients  $\nabla n(\vec{r})$  in the expansion of the  $V_{xc}[n(\vec{r})]$  given by Eq. (2.21). This contribution allows us to take into account the effects of density gradients on the XC energy, but of course it also makes the solution of the DFT equations more difficult to solve.

Some of the main XC functionals, beside the LDA, are the following:

- The generalized gradient approximation (GGA) in which the dependence on the gradient of the density is taken into account.

- The meta-GGA, usually more accurate than the GGA, which includes the density, the gradient of the density and the Laplacian of the density in the expansion of  $E_{xc}$ .
- The hybrid functionals, in which exchange HF-like contributions to  $E_{xc}$  are added.

### The local density approximation

The LDA is the oldest and most simplest approximation to quantify the exchange and correlation energy. It was proposed by Hohenberg and Kohn in 1965 [57]. The LDA is based upon the simple idea of using the known exchange-correlation energy at a point  $\vec{r}$  of the homogeneous electron gas, also for the realistic inhomogeneous electron gas by setting the density of the homogeneous gas equal to the local density of the inhomogeneous system. Consequently, the approximation to the XC is written as

$$E_{xc}^{LDA}[n] \equiv \int \varepsilon_{xc}^{LDA}(\vec{r}) n(\vec{r}) d\vec{r}, \quad (2.22)$$

where

$$\varepsilon_{xc}^{LDA}(\vec{r}) = \varepsilon_{xc}^{hom}[n(\vec{r})] \quad (2.23)$$

denotes the exchange and correlation energy density of the homogeneous electron gas.  $\varepsilon_{xc}(\vec{r})$  can be split into an exchange and a correlation contribution as

$$\varepsilon_{xc}^{LDA}(\vec{r}) = \varepsilon_x^{hom}(\vec{r}) + \varepsilon_c^{hom}(\vec{r}) \quad (2.24)$$

The exchange part  $\varepsilon_x^{hom}(\vec{r})$  represents the exchange energy of a homogeneous electron gas having the density  $n(\vec{r})$ . It was originally derived by Bloch and Dirac in the late 1920 [65] and is given by

$$\varepsilon_x^{hom}(\vec{r}) = -\frac{3}{4} \left( \frac{3n(\vec{r})}{\pi} \right)^{\frac{1}{3}}. \quad (2.25)$$

For the correlation part  $\varepsilon_c^{hom}(\vec{r})$ , there is no simple explicit expression. However, highly accurate results from quantum Monte Carlo techniques were found by Ceperley and later Alder [66] and parametrized by Perdew and Zunger [67].

### Spin polarization

The extension of density functional theory to include the effects of spin polarization is called spin-density functional theory. In magnetic systems this is used together with

the local-spin-density approximation, often referred to as the LSDA [68], in which the exchange correlation potential depends not only on the local electron density but also on the local spin density (the difference between the electron density of spin-up  $n_\uparrow$  and spin-down  $n_\downarrow$  electrons with  $n = n_\uparrow - n_\downarrow$ ). This method can be used to perform realistic calculations of electronic band structure and obtain quantitative information concerning the spin density of real systems. The form of the local spin-density approximation is written as

$$E_{xc}^{LSDA}[n(\vec{r})] \equiv \int \varepsilon_{xc}[n_\uparrow(\vec{r}), n_\downarrow(\vec{r})] n(\vec{r}) d\vec{r}. \quad (2.26)$$

For the exchange energy, the exact result (not just for local density approximations) is known in terms of the spin-unpolarized functional

$$E_x[n_\uparrow, n_\downarrow] = \frac{1}{2}(E_x[2n_\uparrow] + E_x[2n_\downarrow]). \quad (2.27)$$

The spin-dependence of the correlation energy density is approximated by introducing the relative spin-polarization

$$P = \frac{n_\uparrow(\vec{r}) - n_\downarrow(\vec{r})}{n_\uparrow(\vec{r}) + n_\downarrow(\vec{r})}. \quad (2.28)$$

The spin-polarization value  $P = 0$  corresponds to the spin-unpolarized (non-magnetic) case with equal contributions of spin-up and spin down electrons densities, i.e., ( $n_\uparrow = n_\downarrow$ ), whereas  $P = \pm 1$  corresponds to the fully spin polarized (ferromagnetic) situation where one spin density vanish.

By construction LDA is obviously *exact* for the special case of a uniform electron gas. Therefore, at first sight one might expect LDA to be accurate when the length scale over which  $n(\vec{r})$  varies is very large [61]. In other words, one could expect the LDA to be a good approximation only for slowly varying densities. However, the LDA has been proven to yield very good results in many applications, even for atomic systems where the hypothesis of a slowly varying density evidently violated [69]. This is due to the fact that the LDA satisfies a number of exact global features, such as the sum rule for the exchange and correlation hole. However, the LDA also has several important failures. For example, the LDA systematically underestimates the band gap in semiconductors. In the case of Ge the calculated band gap is even negative, which erroneously indicates that Ge should be a metal [69]. Also, LDA overestimates the cohesive energies and bond strengths in molecules and solids often by 20% and even more. As a consequence bond lengths are often underestimated.

Moreover, this approximation works very well for metals, but not so well for localized systems. This is because the Coulomb energy represents the response of a particular electron to the electron density, but the density is due to all electrons, including the particular electron. So electron self-interaction are unavoidably, but mistakenly included. This is not so bad for the metal where any given electron is just one part of the vast conduction electron ocean., but disastrous in a localized systems in which a particular state may be occupied by only on electron.

### The generalized gradient approximation

A simple extension to the LDA or LSDA is the *generalized gradient approximation*. The GGA exchange and correlation functionals yield much better atomic energies and binding energies the LDA at a modest additional computational cost. In particular, they yield a good description of the Hydrogen bond, thus opening the way to calculations for systems such as water, in which Hydrogen bonds play a crucial role.

For non-uniform electron densities, the XC energy deviates significantly from the result of uniform electron gas. The GGA exchange-correlation functional explicitly depends on the gradient of the electron density in order to correct (improve) this deviation. The energy functional is conveniently written in terms of an analytical function known as the exchange enhancement factor,  $F_{xc}[n(\vec{r}), \nabla n(\vec{r})]$ , which modifies the LDA XC energy density  $\varepsilon_{xc}^{hom}[n(\vec{r})]$  of the homogeneous electron gas [61]:

$$E_{XC}^{GGA}[n(\vec{r})] = \int n(\vec{r}) \varepsilon_{xc}^{hom}[n(\vec{r})] F_{xc}[n(\vec{r}), \nabla n(\vec{r})] d\vec{r} \quad (2.29)$$

In recent years, several GGA implementations have shown their high efficiency and therefore become a standard choice for calculations. The most widely used XC functionals involving gradients of  $n(\vec{r})$  have been proposed by Perdew and Wang (PW86) [70], Perdew and Wang (PW91) [71], Perdew, Burke and Enzerhof (PBE) [72], Hammer, Hansen and Norskov (RPBE) [73]. The *meta*-GGA functional is in principle more accurate than the GGA, because it includes more expansion terms depending on the density, its gradient and its Laplacian. In the present calculations, we have used the **PW91** functionals [71], because these functionals are appropriate and yield more accurate results for the present system.

## 2.3 Numerical implementation of DFT

### 2.3.1 Planewaves and Bloch theorem

In order to perform DFT calculations for periodic systems (i.e., 1D wires, stripes, films and solids), we take advantage of the fact that the ions are arranged in a regular periodic ways in one or more directions. This means that the external potential felt by the electrons will be also periodic with respect to translations along any multiple of the crystal unit cell extension  $\vec{R}_i = \sum_j m_j \vec{a}_j$ , where  $m_j \in \mathbb{Z}$  and  $\vec{a}_j$  are the basis vectors spanning over the regular Bravais lattice.

The *Bloch theorem* [74] states that the electronic wavefunction in a periodic solid can be written as the product of a plane-wave of wave vector  $\vec{k}$  within the first Brillouin zone times an appropriate lattice-periodic function  $u_{n\vec{k}}(\vec{r})$ :

$$\psi_{n\vec{k}}(\vec{r}) = e^{i\vec{k}\cdot\vec{r}} u_{n\vec{k}}(\vec{r}), \quad (2.30)$$

Here,  $n$  refer to band index and  $u_{n\vec{k}}(\vec{r})$  satisfies

$$u_{n\vec{k}}(\vec{r} + \vec{R}_i) = u_{n\vec{k}}(\vec{r}) \quad (2.31)$$

for all real-space lattice vectors  $\vec{R}_i$  (vectors of the crystal lattice) or the length of the unit cell. This implies that under the lattice translational operator  $T_{\vec{R}_i}$ , the *Bloch functions* transform according to the expression

$$T_{\vec{R}_i} \psi_{n\vec{k}}(\vec{r}) = \psi_{n\vec{k}}(\vec{r} + \vec{R}_i) = e^{i\vec{k}\cdot\vec{R}_i} \psi_{n\vec{k}}(\vec{r}) \quad (2.32)$$

*Bloch functions*  $\psi_{n\vec{k}}$  and their eigenvalues are periodic in  $\vec{k}$ -space,

$$\psi_{n\vec{k}+\vec{G}}(\vec{r}) = \psi_{n\vec{k}}(\vec{r}) E_{\vec{k}+\vec{G}}(\vec{r}) = E_{n\vec{k}}(\vec{r}). \quad (2.33)$$

where  $\vec{G}$  is an arbitrary reciprocal lattice vector defined by  $\vec{G} \cdot \vec{R}_i = 2\pi l$ , where  $l$  is an integer and ensures that  $e^{i\vec{G}\cdot\vec{R}_i} = 1$  for each  $\vec{G}$  and  $\vec{R}_i$ . The electron wavefunctions may therefore be written as a linear combination of plane waves:

$$\psi_{n\vec{k}}(\vec{r}) = \sum_{\vec{G}} c_{\vec{k}+\vec{G}} \cdot e^{i(\vec{k}+\vec{G})\cdot\vec{r}} \quad (2.34)$$

It is possible to use a plane wave basis set with pseudopotential: an effective potential that "mimics" the effect of an nucleus and the core electrons on valence electrons. The true electronic valence orbitals are replaced by pseudo-orbitals that do not have the orthogonality wiggles close to the nuclei, which are typical for true orbitals. As a consequence, they are well described by a much smaller number of plane waves.

### 2.3.2 Pseudopotentials: Numerical methods of solving the Kohn-sham equations

To compute the electronic structure of a system using the DFT method, the Kohn-Sham equations in a single unit cell have to be solved in some efficient numerical way. One of the central issues concerning efficiency is the rather different behavior of the electronic wavefunction at different distances from the atomic nuclei i.e., the different behavior of the outer valance electrons and the inner core states. Indeed, the KS orbitals of the relevant valence electrons and, in particular localized atomic wavefunctions of the core electrons (i.e., the  $1s$ ,  $2s$ ,  $2p$ , orbitals of the TMs considered in this works) the valence wavefunctions oscillate rapidly in the core region. This makes it very challenging to describe them precisely without involving extremely large basis sets. The core electrons are located very near to the atomic nucleus and therefore do not contribute to the chemical bond formation and to magnetism. It is clear that focusing on the valence states significantly reduces the actual computational time.

The pseudopotential method is an attempt to handle the complicated effects resulting from the orthogonality of the valance electron with respect to the core electron orbitals by introducing an effective potential. In this method, a smooth potential is constructed in order to reproduce the effect of the core on the remaining valence electrons. In this was the KS equations apply only to the valence electrons and the true atomic orbitals are replaced by pseudo-orbitals which do not have the orthogonality wiggles close to the nuclei. Consequently, they are well described by a much small number of plane waves and the computation time is significantly reduced. However, this simplification has mainly two major drawbacks. First, all information on the full wavefunction close to the atomic nuclei is lost. This degrades and renders impossible the calculation of certain properties which depend on the density of KS orbitals in the core region (e.g., electric field gradients, hyperfine parameters, etc). A second major limitation is that there is no systematic way to construct reliable transferable pseudopotentials.

Another commonly used scheme is to consider all-electrons. Thus, all the information about the wavefunction is available. This method is often but not necessary connected to the frozen-core approximation, in which the core orbitals are computed



once for the isolated atoms and kept fixed. This is justified by the fact that the core states do not participate in the formation of chemical bonds. One of the most important all-electron approaches is the augmented plane-wave method (APW) introduced by Slater in 1937 [54]. In this approach the space is divided into two regions: spheres around each core, in which the wavefunctions are taken as some atomic-like partial waves, and the interstitial region, in which a plane-wave basis is used. The partial waves and envelope functions are then matched at the boundaries of the spheres.

A spread approach in this context is the PAW method proposed by P. Blöchl in 1994 [75]. This is an extension to both the APW and pseudopotential methods, which can be retrieved by well-defined approximations. The PAW method unifies all electron and pseudopotential approaches. The different shape or behavior of the wavefunctions in different regions points towards the need of a proper partitioning of the space around the nuclei. The PAW method takes into account this and separates the wavefunction in two parts: a partial wave expansion within an atom-centered sphere, and an envelope function outside. The two parts are then matched smoothly at the sphere edge.

The characteristics of the KS orbitals are very different in different regions of space. They are smooth in the core region, but near the nuclei they show rapid oscillations, which are very demanding on the numerical representation of the wave functions. In order to solve this problem, we consider a linear unitary transformation  $\mathcal{T}$  which maps pseudo or auxiliary smooth wavefunctions  $|\tilde{\psi}\rangle$  to the physically relevant all-electron Kohn-Sham single particle wavefunctions  $|\psi\rangle$ :

$$|\psi_n\rangle = \mathcal{T} |\tilde{\psi}_n\rangle. \quad (2.35)$$

The tilde refers to the representation of auxiliary smooth wavefunctions and  $n$  labels the quantum-state, including the band index, spin and  $\vec{k}$ -vector index. The transformation  $\mathcal{T}$  modifies the *smooth auxiliary or pseudo wavefunction* close to the nuclei (in each atomic region), and it built the *all-electron wavefunction* with its correct nodal structure. Therefore, one can write the transformation

$$\mathcal{T} = 1 + \sum_a \mathcal{T}_a \quad (2.36)$$

as the identity plus a sum of atomic contributions  $\mathcal{T}_a$ , where each  $\mathcal{T}_a$  adds the difference between the true and the pseudo wavefunction only within the core region of a atom. P. Blöchl proposed three kind of wavefunctions in order to explain  $\mathcal{T}_a$ . Within the augmentation region  $\Omega_a$ , every *pseudo wavefunction* can be expanded into partial waves  $\phi_{i,a}$  as

$$|\tilde{\psi}\rangle = \sum_i c_{i,a} |\tilde{\phi}_{i,a}\rangle, \quad (2.37)$$

within  $\Omega_a$ . Similarly, the *all-electron wavefunction* has the form

$$|\psi\rangle = \sum_i c_{i,a} |\phi_{i,a}\rangle, \quad (2.38)$$

within  $\Omega_a$ . Hence, we can express the true wavefunction as

$$|\psi\rangle = |\tilde{\psi}\rangle - \sum_i c_{i,a} |\tilde{\phi}_{i,a}\rangle + \sum_i c_{i,a} |\phi_{i,a}\rangle. \quad (2.39)$$

Since  $\hat{\mathcal{T}}$  is linear, the coefficients of the pseudo wavefunction  $|\tilde{\psi}\rangle$  must be linear functionals, i.e., scalar products

$$c_{i,a} = \langle \tilde{p}_{i,a} | \tilde{\psi} \rangle, \quad (2.40)$$

where the projector functions  $\tilde{p}_{i,a}$  are fixed.

Since there is zero overlap between different augmentation spheres, the one-center expansion of a real pseudo wavefunction  $\sum_i \langle \tilde{p}_{i,a} | \tilde{\psi} \rangle |\tilde{\phi}_{i,a}\rangle$  has to be identical to  $|\tilde{\phi}_{i,a}\rangle$  inside the augmentation sphere. This is equivalent to referring the completeness relation

$$\sum_i |\tilde{\phi}_{i,a}\rangle \langle \tilde{p}_{i,a}| = 1 \quad (2.41)$$

within  $\Omega_a$ , which in turn implies

$$\langle \tilde{p}_{i_1,a} | \tilde{\phi}_{i_2,a} \rangle = \delta_{i_1,i_2}, \quad (2.42)$$

within  $\Omega_a$ . In other words the pseudo functions and the partial waves are mutually orthonormal within the augmentation sphere. Finally, by inserting Eq. (2.40) into Eq. (2.39) we obtain a closed form for the transformation operator

$$(2.43)$$

which permits us to obtain the true, all-electron, Kohn-Sham wavefunction  $\psi(\vec{r})$  as

$$|\psi(\vec{r})\rangle = |\tilde{\psi}(\vec{r})\rangle + \sum_{a,i} \left( |\phi_{i,a}(\vec{r})\rangle - |\tilde{\phi}_{i,a}(\vec{r})\rangle \right) \langle \tilde{p}_{i,a} | \tilde{\psi} \rangle. \quad (2.44)$$

Notice that this split the extended-space and the atom-centered contributions. This allows to obtain compact expression for various quantities in PAW. The first term can be evaluated on an extended grid, or on a soft basis set, while the last two terms are evaluated on fine radial grids. In summary, the PAW transformation is expressed in terms of three components:

- The partial waves  $|\phi_{i,a}\rangle$  which are obtained as solutions of the Schrödinger equation for the isolated atom and utilized as an atomic basis for the all-electron wavefunctions within the augmentation sphere.

- The smooth pseudo partial waves  $|\tilde{\phi}_{i,a}\rangle$  which match with the corresponding true partial waves outside the augmentation sphere but are smooth continuations inside the spheres. These are employed as atomic basis-sets for the pseudo-wavefunctions.
- The smooth projector pseudo-functions  $|\tilde{p}_{i,a}\rangle$  one for each partial wave, which satisfy the condition  $\langle \tilde{p}_{i_1,a} | \tilde{\phi}_{i_2,a} \rangle = \delta_{i_1,i_2}$  inside each augmentation sphere.

Up to this point the PAW method may be considered as an exact implementation of DFT. In order to make it a practical scheme, the following three approximations are required.

- i) *Frozen ore approximation*: Since the core orbitals are localized within the augmentation spheres, it is assumed that they are not modified by the formation of chemical bonds. Therefore, the core Kohn-Sham orbitals are taken from the calculations on the isolated atoms. We thus write

$$|\phi_c^n\rangle = |\psi_{a,core}^\alpha\rangle \quad (2.45)$$

where the index  $n$  on the left hand side refers to both a specific atom  $a$  and an orbital  $\alpha$ .

- ii) *Finite basis set*: The extended pseudo contribution  $\tilde{\psi}_n$  in Eq. (2.44) is measured outside the augmentation spheres by using either an appropriate basis set or a real-space grid. In both cases the lack of completeness in the basis or, equivalently the finite grid-spacing necessary. This is however easy controllable error.
- iii) *Finite number of partial waves and projectors*: The number of partial waves and projector functions is also finite. This means that the completeness condition we have assumed is not strictly fulfilled. However, this approximation can be controlled by increasing the number of partial waves and projectors until they form a satisfactory complete space for the expansion of the wave functions within the augmentation spheres.

More detailed information about the PAW method may be found in Ref. [75].

### 2.3.3 The Hellmann-Feynman theorem

As pointed out in the discussion of the BO approximation in section 2.1 the electronic energy  $E = E(\vec{R}_i)$  for a given fixed ion position  $\vec{R}_i$  results an effective potential which is felt by the ions as they move. This leads to forces acting on the ions. We explicit

the the Hellmann-Feynman (HF) theorem presented independently by H. Hellmann in 1937 [76] and R. Feynman in 1939 [77]. It states that *the derivative of the electronic energy  $E$  with respect to the ion positions  $\vec{R}_i$  (which are external parameters) equals to the expectation value of the derivative of the electronic Hamiltonian  $\hat{H}$  with respect to  $\vec{R}_i$ .*

Suppose  $\psi$  is a wavefunction of the Hamiltonian  $\hat{H}$ , than the energy derivative with respect to ion position  $\vec{R}_i$  is given by

$$\frac{\partial E}{\partial \vec{R}_i} = \frac{\partial}{\partial \vec{R}_i} \langle \psi | \hat{H} | \psi \rangle = \left\langle \frac{\partial \psi}{\partial \vec{R}_i} | \hat{H} | \psi \right\rangle + \langle \psi | \hat{H} | \frac{\partial \psi}{\partial \vec{R}_i} \rangle + \langle \psi | \frac{\partial \hat{H}}{\partial \vec{R}_i} | \psi \rangle. \quad (2.46)$$

As the exact ground state wavefunction, the energy is minimum with respect to all possible variations of the wavefunction. It follow that the first and second terms vanish.

Therefore, the forces  $\vec{F}$  acting on the atoms are given by

$$\vec{F} = -\frac{\partial E}{\partial \vec{R}_i} = -\langle \psi | \frac{\partial \hat{H}}{\partial \vec{R}_i} | \psi \rangle. \quad (2.47)$$

The force plays an important role in order to determine the *local energy minimum* for a given ionic system without recalculating the electronic state, or finding their derivatives. The total energy of the system decreases by decreasing the ion position in the direction of the force. In practices, one considers that the minimum-energy configuration has been reached when the residual forces  $\vec{F}$  on all the atoms are smaller than a given small value (typically  $\sim 0.01 - 0.001$  meV).

## 2.4 Calculation Tool

In this thesis, the calculation have been performed in the framework of Hohenberg-Kohn-Sham DFT, as implemented in the Vienna *ab-initio* simulation package (VASP) [78]. This is a periodic supercell approach. The XC energy-functional is treated by using Perdew and Wang's spin-polarized GGA [71]. The spin-polarized KS equations are solved in an augmented plane-wave basis set, taking into account the interaction between valence electrons and atomic cores by means of the PAW method [75]. This is an efficient frozen-core approach, which takes into account the proper nodes of the valence KS orbitals in the core region and the resulting effects on the electronic structure and magnetic properties.

The KS wave functions are expanded in the interstitial region in a plane wave basis set with a cut-off energy of  $E_{max} = 500$  eV. The integrations in the Brillouin zone

(BZ) are performed by using the Monkhorst-Pack scheme [79]. The used numbers of  $k$ -points are defined in the respective chapter for each system. The cut-off energies and  $k$ -points have been checked to yield accurate results for the present systems. For metallic-like systems, one often finds very rapid variations of the states close to the Fermi level  $\varepsilon_F$  that may cause a poor convergence of the relevant physical quantities such as the total energy or the local magnetic moments. Therefore, a smearing of the KS levels is introduced in order to improve the numerical stability. Here, we use a Gaussian smearing with a width  $\sigma = 0.05$  eV, a value that ensures that the smearing contribution to the total energy is less than 1 meV/atom. The criterion for the energy convergence has been set to  $10^{-5}$  eV and the force on each atom less than  $10^{-2}$  eV/Å.

This DFT method is expected to yield an accurate description of the electronic structure results even for large systems, and it requires a relatively small plane-wave basis set for each atom in the calculation. It also contains the opportunities to include spin orbit coupling, noncollinear spiral SDWs [80], and external electric fields in the system [81]. Based on its past success, we utilize DFT-GGA for our studies.



# Theory of magnetism in transition metal nanostructures

## 3.1 Noncollinear magnetic order in density functional theory

In principle, the spin-polarized DFT, as presented in the section 2.2, allows us to determine the ground-state of any magnetic system showing collinear as well as noncollinear orders. In the collinear case, the magnetization  $\vec{m}(\vec{r})$  has the form  $\vec{m}(\vec{r}) = m(\vec{r}) \hat{\mu}$ , where  $\hat{\mu}$  is the unit vector independent of  $\vec{r}$ . In other words,  $\vec{m}(\vec{r})$  is either parallel or antiparallel to a given direction of  $\hat{\mu}$ . The collinear spin-density formalism only allows us to consider single-particle wave function having either spin-up or spin-down character. Therefore, it is always possible to choose the spin coordinate frame such that the *spin-quantization axis* pointing along the  $z$ -direction. In noncollinear configurations, the single-particle KS orbitals having a mixed spin-up and spin-down character. This is indispensable in order that the magnetization density  $\vec{m}(\vec{r})$  varies not only in magnitude but also in direction. In noncollinear spin-polarized DFT the fundamental variable is the Hermitian  $2 \times 2$  density matrix  $n_{\alpha\beta}(\vec{r})$ , where  $\alpha$  and  $\beta$  refer to spin indices ( $\alpha, \beta = \uparrow, \downarrow$ ). Accordingly, the KS orbitals are represented by spin-1/2 spinors. The charge density  $n(\vec{r})$  is given by the trace

$$n(\vec{r}) = \sum_{\alpha} n_{\alpha\alpha}(\vec{r}). \quad (3.1)$$

The magnetization density is obtained from

$$\vec{m}(\vec{r}) = \sum_{\alpha\beta} n_{\alpha\beta}(\vec{r}) \cdot \vec{\sigma}_{\alpha\beta}, \quad (3.2)$$

where  $\vec{\sigma} = (\sigma_x, \sigma_y, \sigma_z)$  is the vector of Pauli matrices. Conversely, one may express  $n_{\alpha\beta}(\vec{r})$  in terms of  $n(\vec{r})$  and  $\vec{m}(\vec{r})$  as

$$n_{\alpha\beta}(\vec{r}) = \frac{1}{2} [\delta_{\alpha\beta} n(\vec{r}) + \vec{\sigma}_{\alpha\beta} \cdot \vec{m}(\vec{r})] \quad (3.3)$$

or where explicitly, as

$$n_{\alpha\beta}(\vec{r}) = \frac{1}{2} \begin{pmatrix} n + m_z & m_x - im_y \\ m_x + im_y & n - m_z \end{pmatrix}. \quad (3.4)$$

The functional derivatives of the exchange and correlation energy  $E_{XC}[n_{\alpha\beta}(\vec{r})] = E_{XC}[n(\vec{r}), \vec{m}(\vec{r})]$  with respect to the charge and spin densities yield, for example in the local spin density approximation, the scalar XC potential

$$v_{XC}[\vec{r}, n(\vec{r}), \vec{m}(\vec{r})] = \frac{\delta E_{XC}}{\delta n(\vec{r})} = \epsilon_{XC} + n(\vec{r}) \frac{\delta \epsilon_{XC}}{\delta n(\vec{r})} \quad (3.5)$$

and the XC magnetic field

$$\vec{b}_{XC}[\vec{r}, n(\vec{r}), \vec{m}(\vec{r})] = \frac{\delta E_{XC}}{\delta \vec{m}(\vec{r})} = \vec{m}(\vec{r}) n(\vec{r}) \frac{\delta \epsilon_{XC}}{\delta m(\vec{r})} \quad (3.6)$$

Notice that in LDA, and in others semi-local approximations to the XC energy, the XC energy density  $\epsilon_{XC}$  depends only on the norm  $m(\vec{r})$  of the magnetization density and not on the relative orientation of  $\vec{m}(\vec{r})$  at different points. Therefore, the XC magnetic field  $\vec{b}_{XC}(\vec{r})$  is parallel to the magnetization density  $\vec{m}(\vec{r})$ . The same holds for the generalized gradient approximation [71, 80]. Further details on the implementation of noncollinear magnetism the PAW formalism may be found in the Ref. [80].

Let us finally mention that in noncollinear calculations the computational effort increases by a factor of 4 in comparison with the collinear calculation. Furthermore, in many cases noncollinearity reduces the symmetry of the problem, which results in an increase of the irreducible wedge of the Brillouin zone. Thus, a larger number of Bloch vectors  $\vec{k}$  have to be incorporated. Since the computational requirement increases with the number of  $\vec{k}$ -points, the noncollinear calculations are in general highly time-consuming.

### 3.1.1 Spin spiral

A spin spiral is a periodic static noncollinear magnetic structure in which the local magnetic moments  $\vec{\mu}_i$  at the different atoms  $i$  are rotated around a given axis  $\hat{n}$  by



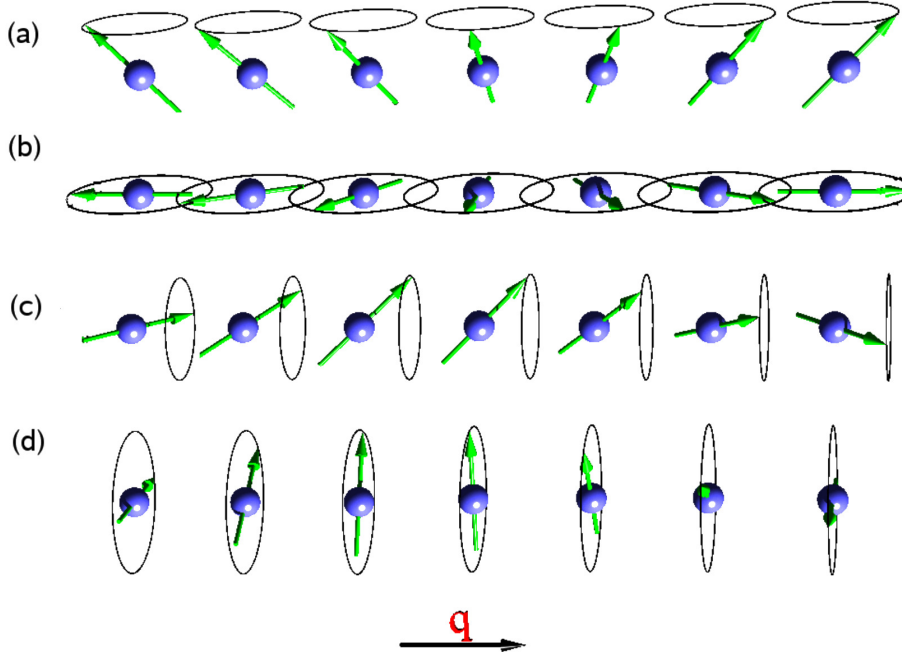


**Figure 3.1:** Illustration of a spin spirals with spin-rotation axis perpendicular and parallel to the wave vector  $\vec{q}$ . The magnetic moment is rotated by wave vector  $\vec{q} = (0, 0, \pi/a)$  between the neighboring atoms. (a-c) shows a tilted view of the spirals with cone angle  $\theta = \pi/4$ , and (b-d) flat spirals with cone angle  $\theta = \pi/2$  (after Ref. [82]).

a constant angle  $\Delta\phi$  along a certain direction  $q$  in a crystal. These magnetic structures are also called spiral SDWs in order to distinguish them from the longitudinal spin-density waves. The magnitude  $q$  of spin density wave vector  $\vec{q} = q\hat{q}$  defines the periodicity of the spin spiral order by the usual relation  $\lambda = 2\pi/q$ , where  $\lambda$  is the wave length. The angle of the local magnetic moment  $\mu_i$  at atomic position  $\vec{R}_i$  is given by  $\phi_i = \vec{q} \cdot \vec{R}_i$ . Thus, all atoms lying on a plane perpendicular to  $\vec{q}$  share the same angle of rotation. Assuming for a simplicity that the rotation axis  $\hat{n}$  is along the  $z$ -axis [ $\hat{n} = (0, 0, 1)$ ]. The local moment  $\vec{\mu}_i$  at atom  $i$  is given by

$$\vec{\mu}_i(\vec{R}_i) = \mu_0 \begin{pmatrix} \cos(\vec{q} \cdot \vec{R}_i) \sin \theta \\ \sin(\vec{q} \cdot \vec{R}_i) \sin \theta \\ \cos \theta \end{pmatrix}, \quad (3.7)$$

where  $\mu_0$  is the magnitude of the magnetic moment, which is assumed to be site-independent. The angle  $\theta$  between the rotation axis and the local moments is known as the cone angle.

Three parameters are important to define a spin spiral wave:

- i) The spin spiral vector  $\vec{q}$ , which defines the propagation direction of the wave and the angle between the local moments at neighboring atoms,
- ii) the rotation axis  $\hat{n}$  around which the local moments are oriented, and
- iii) the cone angle  $\theta$ , which defines the direction of the magnetic moment at the origin of the coordinate system  $\vec{\mu}(R_{i=0}) = (\sin \theta, 0, \cos \theta)$  [see Fig. 3.1].

Fig. 3.1 shows that the four different spin spiral configurations with wave vectors  $\vec{q} = (0, 0, \pi/4a)$ . For  $\theta = \pi/2$ , the spirals rotate in the plane perpendicular and parallel to the rotation axis and are called flat spirals [see Fig. 3.1 (a-c)]. This method is computationally demanding, because it requires a large magnetic unit cell in order to compute the energy of spin spiral particularly for small  $\vec{q}$ -values. However, within this scheme the spin-orbit coupling effects on the stability of spin spiral can be calculated.

### 3.1.2 Constrained magnetic moments

In order to determine the energy of the magnetic system (e.g., TM nanostructures) corresponding to a fixed arbitrary set of orientations  $\{\hat{e}_i\}$  of the local magnetic moments at each atom  $i$ , it is necessary to impose constraints on the magnetization density  $\vec{m}(\vec{r})$ , since arbitrary spin arrangements are not equilibrium states in general. For this purpose we apply constraints to spin-projected DFT by means of the penalty functional method [60,83]. In the scheme proposed by Haynes and Payne [84] a penalty functional

$$E_P[\vec{m}(\vec{r})] = \frac{\lambda}{2} \sum_i [\vec{\mu}_i - (\vec{\mu}_i \cdot \hat{e}_i) \hat{e}_i]^2 \quad (3.8)$$

is added to the Hohenberg-Kohn energy functional  $E_{\text{HK}}[n(\vec{r}), \vec{m}(\vec{r})]$ , where the local magnetic moment

$$\vec{\mu}_i = \langle \vec{m} \rangle_i = \int_{\text{WS}(i)} \vec{m}(\vec{r}) d\vec{r}^3 \quad (3.9)$$

at atom  $i$  is obtained by integrating  $\vec{m}(\vec{r})$  within the corresponding WS sphere. Eq. (3.8) can be written as

$$E_P[\vec{m}(\vec{r})] = \frac{\lambda}{2} \sum_i (\vec{\mu}_i^\perp)^2, \quad (3.10)$$

where  $\vec{\mu}_i^\perp$  is the projection of  $\vec{\mu}_i$  perpendicular to  $\vec{e}_i$ . This penalty functional has an effect that is similar to an applied local magnetic field and can be regarded as such.

The aim of including this term in the Hamiltonian is to force the local moment  $\vec{\mu}_i$  to have the specific direction  $\hat{e}_i$ . The parameter  $\lambda > 0$  entering Eq. (3.8) controls the strength of the local magnetic fields acting inside each WS cell, which impose the constraints. Hence, in the limit of  $\lambda \rightarrow +\infty$ , the local moments are forced to be parallel to the unit vectors  $\hat{e}_i$ . The additional contribution to the total energy produced by the constrained local moments decreases with increasing  $\lambda$  and can in principle be made vanishingly small. Increasing  $\lambda$  stepwise, from one run to another (slowly so the solution remains stable) one thus converges towards the DFT total energy for a given magnetic configuration [78]. However, a value of the order of  $\lambda = 10\text{--}50 \text{ eV}/\mu_B$  is usually large enough, so that  $E_P$  and the deviations from the imposed magnetic arrangement can be simply neglected.

### 3.1.3 Generalized Bloch theorem

The *generalized Bloch theorem* (GBT) is an alternative and a simple approach to describe spin spirals in periodic systems [85]. Within this approach it is possible to improve the computational efficiency as well as numerical accuracy by reducing the number of atoms in the supercell. Using the GBT, for example, in the case of the linear chain, one needs only one atom in unit cell to compute the spin spiral dispersion relation even for very small  $\vec{q}$ -values. A direct comparison between these two methods is illustrated in Fig. 3.2.

According to the classical *Bloch theorem* as discussed in section 2.3.1, the wavefunction  $\psi_{n\vec{k}}(\vec{r})$  is translational invariant with a translation operator  $T_{\vec{R}_i}$ . For a spin-polarized system in which the magnetization is rotating with a constant angle  $\Delta\phi = (\vec{q} \cdot \vec{R}_{i+1}) - (\vec{q} \cdot \vec{R}_i)$  along a certain direction in the crystal. The wavefunction  $\psi_{n\vec{k}}(\vec{r})$  of the system remains invariant under the general translation and satisfies the equation

$$U(\phi) \psi_{n\vec{k}}(\vec{r} + \vec{R}_i) = e^{i\vec{k} \cdot \vec{R}_i} \psi_{n\vec{k}}(\vec{r}) \quad (3.11)$$

where  $U(\phi)$  represents a spin-1/2 rotation matrix by an angle  $\phi$  perpendicular to  $z$ -axis, which can be written as

$$U(\phi) = \begin{bmatrix} e^{-i\phi/2} & 0 \\ 0 & e^{i\phi/2} \end{bmatrix} \quad (3.12)$$

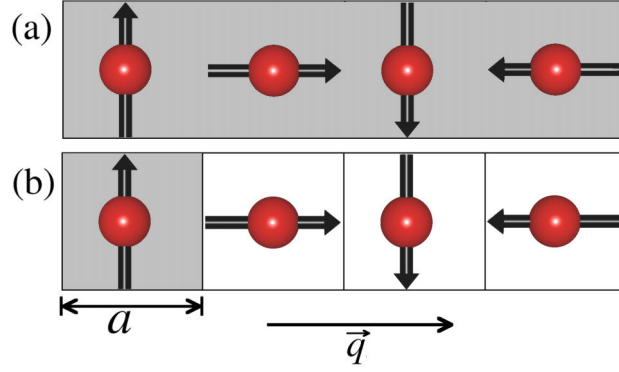


**Figure 3.2:** Illustration of two different possibilities of flat spiral spin-density wave in a linear chain having a wave vector  $\vec{q} = (0, 0, \pi/2a)$ : (a) using a large supercell, (b) generalized Bloch theorem approach. The high-lighted unit cell are used for spin spiral calculations.

On the basis of *generalized Bloch theorem*, the wave function is described as a two components Bloch spinors instead of the usual one-electron wave function. The Bloch spinors are still characterized by a wave vector  $\vec{k}$  in the first Brillouin zone

$$u_{n\vec{k}}^{\sigma}(\vec{r} + \vec{R}_i) = u_{n\vec{k}}^{\sigma}(\vec{r}), \quad (3.13)$$

with  $\sigma \in \{\uparrow, \downarrow\}$

$$\psi_{n\vec{k}}(\vec{r}) = e^{i\vec{q}\cdot\vec{r}} \begin{pmatrix} e^{i\vec{q}\cdot\vec{r}/2} u_{n\vec{k}}^{\uparrow}(\vec{r}) \\ e^{-i\vec{q}\cdot\vec{r}/2} u_{n\vec{k}}^{\downarrow}(\vec{r}) \end{pmatrix}. \quad (3.14)$$

Here, the functions  $u_{n\vec{k}}^{\uparrow}(\vec{r})$  and  $u_{n\vec{k}}^{\downarrow}(\vec{r})$  are related to spin-up and spin-down components and invariant with respect to lattice translations. Therefore, It is possible to calculate the magnon-dispersion relation in periodic systems by applying the generalized Bloch theorem. GBT holds only in the absence of spin-orbit coupling.

## 3.2 The classical Heisenberg model

The NC ground-state magnetic order obtained from the DFT calculations can be analyzed from the local perspective in terms of the phenomenological classical Heisenberg model. The energy of the TM nanostructure is described as a function of relative orientation of the local magnetic moments by the Hamiltonian

$$H = - \sum_{i=1}^N \sum_{\delta=1}^{\nu} J_{0\delta} \hat{\mu}_i \cdot \hat{\mu}_{i+\delta}, \quad (3.15)$$

where  $\hat{\mu}_i$  is the unit vector along the direction of the magnetic moment at atom  $i$ , and  $J_{0\delta}$  is the effective exchange interaction between the moment at atom  $i$  and its  $\delta$ th NN. The spin can be classified into three groups: ferromagnets (FM), antiferromagnets (AF), and noncollinear (NC), which can be well described in terms of classical Heisenberg model. For  $J_{01} > 0$ , the local moments  $\mu$  tend to be all aligned in parallel direction or FM. In the case of  $J_{01} < 0$ , the adjacent local moments prefer antialignment (antiparallel) or AF. In addition, there exist noncollinear or incommensurate spin structures, an example of magnetic frustration, in which the competing exchange interactions arising from different atoms cannot simultaneously be satisfied. Furthermore, NC or flat spin spiral is a general solution of the classical Heisenberg model in which the local magnetic moment are given by Eq. (3.15) with the spin spiral wave vector  $\vec{q}$ .

The total electronic energy  $E(q)$  of a flat spiral SDWs is is derived from the Eq. (3.15) reads as

$$E(q) = \sum_{\delta=1}^n J_{0\delta} [1 - \cos(q\delta a)], \quad (3.16)$$

the interaction parameters  $J_{0\delta}$  corresponding to different geometries and lattice parameters can be calculated by mapping the Eq. (3.16) to calculated *ab initio* results. The effective interactions between the local magnetic moments  $\mu_i$  can also be calculated as the Fourier coefficients of  $E(q)$ , which is an alternative approach and express as

$$J_{0\delta} = -\frac{a}{\pi} \int_0^{2\pi/a} dq E(q) \cos(q\delta a). \quad (3.17)$$

The discrete Fourier transformation yields more accurate results, but one needs to check the convergence by acquiring fine value of  $n$ -points. In present work, we find that the interaction up to six NNs ( $n = 6$ ) provides a very accurate description of all the calculated *ab initio* dispersion relations.

### 3.2.1 Effective interactions between local magnetic moments

As we shell see the Heisenberg model provides a very accurate phenomenological description of the *ab initio* results by obtaining the exchange interactions from the magnon dispersion relations via Eq. (3.16) for all considered nanowire geometries.

### 3.2.2 Magnetic phase diagrams

A more detail analysis of the stability of flat spiral density wave in our considered 1D system is provided by the magnetic phase-diagrams of the classical Heisenberg model.

#### $(J_{01}-J_{02})$ phase diagram

The energy dispersion of 1D systems including the first two NN interaction parameters  $J_{01}$  and  $J_{02}$  is given by

$$E(q) = 2J_{01} \cos(qa) + 2J_{02} \cos(2qa) . \quad (3.18)$$

For a minimum of energy [maximum  $E(q)$ ] we require

$$\frac{\partial E}{\partial q} = 0 \rightarrow J_{01} = -4 \cos(qa) \text{ or } q = 0 \pi/a, \quad (3.19)$$

and

$$\frac{\partial^2 E}{\partial q^2} < 0 \text{ or } J_{01} \cos(qa) > -4J_{02} \cos(qa). \quad (3.20)$$

The three cases are summarized in the following

FM	AF	NC
$q = 0$	$q = \pm\pi/a$	$qa \neq 0, \pm\pi/a$
$J_{01} > -4J_{02}$	$J_{01} < 4J_{02}$	Rotating angle $qa$ defined by $\cos(qa) = -J_{01}/4J_{02}$ and
e.g. $J_{01} > 0, J_{02} = 0$	e.g. $J_{01} < 0, J_{02} = 0$	$J_{01} \cos(qa) > -4J_{02} \cos(qa)$

Restricting the range of the interactions up to the most important couplings e.g.,  $J_{01}$  and  $J_{02}$ . One identifies three distinct regimes: the FM, AF and the NC regions. The  $(J_{01}-J_{02})$ -phase diagram of the classical Heisenberg model as a function of the interactions between the first and second NNs summarizes very clearly the competition between these couplings and the resulting ground-state magnetic orders [see Fig. 3.4 (a)].

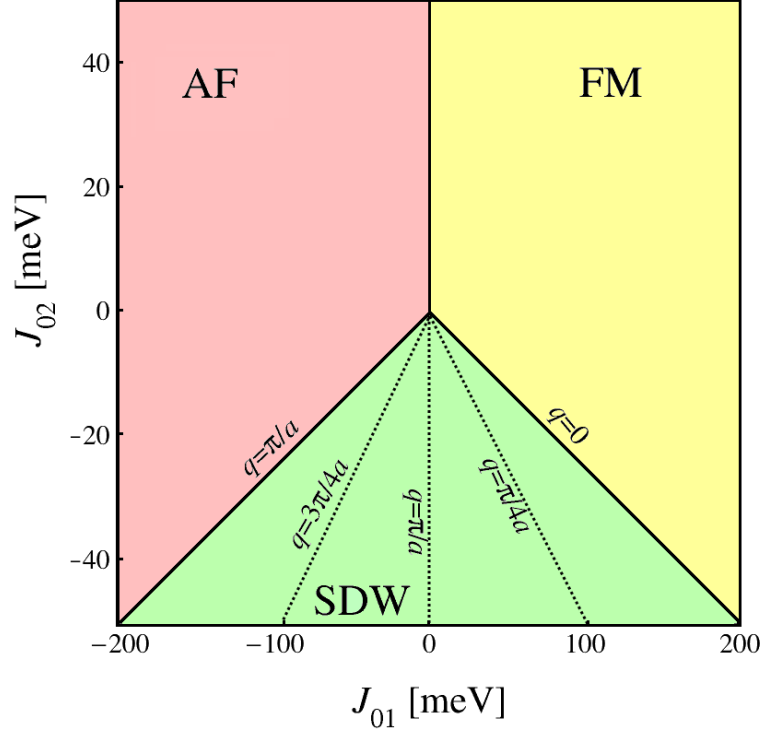


**Figure 3.3:** Magnetic phase diagram of the 1D Heisenberg model having first and second NN interactions  $J_{01}$  and  $J_{02}$ , respectively. The three regions refer to the stable ferromagnetic (FM), antiferromagnetic (AF), and spiral spin-density wave (SDW) configurations. The dotted lines correspond to the spin-spiral arrangements for different values of  $q$ .

### $(J_{01}-J_{02}-J_{03})$ phase diagram

It is more less well know that the decays of the exchange interaction in 1D system is slower than in 2D and 3D ones. Therefore, it is expected that  $J_{02}$  and  $J_{03}$  might take some relevance. Later on, in our present work, we find that only first and second interactions  $J_{02}$  and  $J_{02}$  are not enough to reproduce calculated *ab initio* results, respectively (it can be verified by mapping the dispersion relations to the higher-order interaction coupling  $\sim J_{03}$  or  $J_{04}$ ). Therefore, one can rewrite the Heisenberg energy dispersion equation (3.16) by including the  $J_{03}$  interaction coupling:

$$E(q) = 2J_{01} \cos(qa) + 2J_{02} \cos(2qa) + 2J_{03} \cos(3qa), \quad (3.21)$$

A local minimum for  $q = 0$  is obtained if

$$\frac{1}{a^2} \frac{\partial^2 E(q)}{\partial q^2} = J_{01} + 4J_{02} + 9J_{03} > 0 \quad (3.22)$$

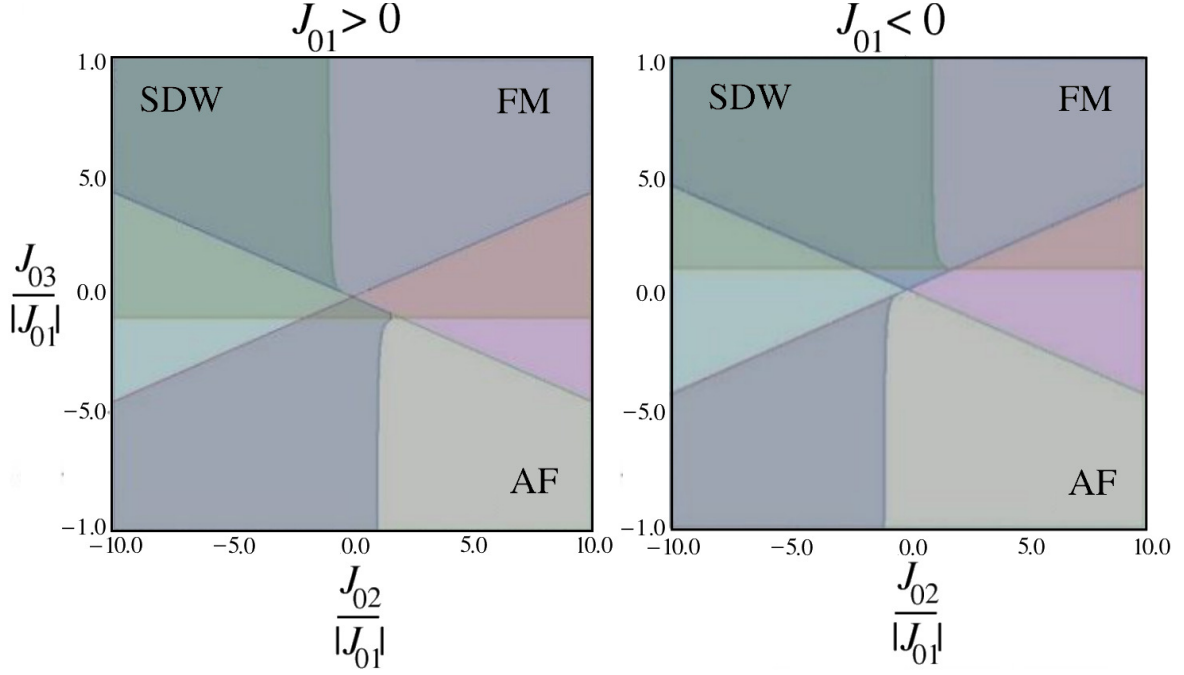


**Figure 3.4:** Magnetic phase diagram of the 1D Heisenberg model having first, second and third NN interactions  $J_{01}$ ,  $J_{02}$  and  $J_{03}$ , respectively. The regions where the magnetic configurations are favored over others are indicated.

and  $q = \pi/a$  has a local minimum if

$$\frac{1}{a^2} \frac{\partial^2 E(q)}{\partial q^2} = -J_{01} + 4J_{02} - 9J_{03} > 0 \quad (3.23)$$

In order to find out the local minimum of spiral SDW arrangements, we obtain the following conditions read in the form

$$\begin{aligned} 1 - 3\frac{J_{03}}{J_{01}} + 4\frac{J_{02}}{J_{01}} \cos(qa) + 12\frac{J_{03}}{J_{01}} \cos^2(qa) &= 0, \\ \cos(qa) + \frac{J_{02}}{J_{01}} \cos(2qa) + \frac{J_{03}}{J_{01}} \cos(3qa) &> 0. \end{aligned} \quad (3.24)$$

for  $J_{01} > 0$  (FM). These equations can only be solved numerically.

By employing the above conditions, it is possible to plot a phase diagram having first, second and third NN interactions  $J_{01}$ ,  $J_{02}$  and  $J_{03}$ , where one can see the stability of magnetic orders including FM, AF and spin spiral. Fig. 3.4 (b) shows a phase diagram which indicates the stability zones of the NC spiral configurations. For instance,



for a spin spiral having  $q = \pi/2$ , we obtain by using Eq (3.27)

$$\frac{J_{03}}{J_{01}} = -\frac{1}{3} \quad (3.25)$$

whereas for  $q = 1/6$

$$\frac{J_{03}}{J_{01}} = \frac{1}{3} - \frac{2}{3} \frac{J_{02}}{J_{01}} \quad (3.26)$$

Similarly, in the case of  $J_{01} < 0$  (AF), the conditions for a spiral minimum take the form

$$\begin{aligned} -1 - 3\frac{J_{03}}{J_{01}} + 4\frac{J_{02}}{J_{01}} \cos(qa) + 12\frac{J_{03}}{J_{01}} \cos(qa)^2 &= 0, \\ \cos(qa) + \frac{J_{02}}{J_{01}} \cos(2qa) + \frac{J_{03}}{J_{01}} \cos(3qa) &> 0. \end{aligned} \quad (3.27)$$

Moverever, we can also explain the nature of magnetic solutions by analyzing the curvatures of Eq. (3.22) and Eq. (3.23). The positive values prefer the FM and AF orders, whereas negative values give rise the possibility of spin spiral configurations.

In this context, we analyze others NC magnetic configurations that they can not be described by a spiral spin-density wave. This study allows us to verify the stability of the spin spiral structures in a more rich variety of magnetic alignments.

### 3.3 Spin-orbit interaction

Relativistic effects play an important role especially in low-dimensional systems (e.g., nanowires, clusters, and ultra-thin films) than in bulk. The MAE is caused by the spin-orbit coupling and the magnetic dipolar interaction. In the presence of SO coupling, the energy for different magnetization orientations give rise to the distinction between minimal (easy axis) and maximal (hard axis) energy orientations. The MAE is, together with saturated magnetization, on of the main characteristics of any magnetic material. It determines the low-temperature orientation of magnetization and the stability of the magnetization direction against thermal fluctuations. For the technology point of view, the magnetic anisotropy and the orbital anisotropy have crucial importance in magnetic recording or memory devices, where one aims to pin the magnetization to a given direction in space. In  $3d$  TM monoatomic chains the calculated MAE is of the order of  $\sim 2\text{--}10$  meV [1, 3, 4, 86], which is very large in magnitude with respect to corresponding bulk values. However, a significant enhancement of MAE is observed in mixed  $3d\text{--}5d$  magnetic alloys [87].

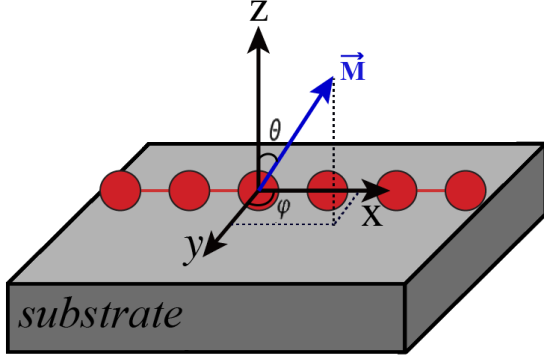


**Figure 3.5:** Magnetization  $\vec{M}$  direction in terms of the polar angle  $\theta$  and azimuthal  $\phi$  angle.

### 3.3.1 Magnetic anisotropy energy

The spin-orbit coupling is the interaction of the spin of a particle with its orbital moment. This is a relativistic effect that can be derived from the Dirac equation [65]. The spin-orbit interaction of a single atom is given by

$$\hat{H}_{SO} = \frac{\hbar}{2m_e^2 c^2} (\nabla V(\vec{r}) \times \vec{p}) \cdot \vec{\sigma}, \quad (3.28)$$

where  $\vec{\sigma}$  are the Pauli matrices,  $V(\vec{r})$  is the electrostatic potential within the muffintins around each atomic nucleus and  $\vec{p}$  is the moment of the electron. Taking into account the spherical symmetry of the potential,  $H_{SO}$  can be rewritten as

$$\hat{H}_{SO} = \xi(\vec{r}) \hat{L} \cdot \hat{S} \quad (3.29)$$

with

$$\xi(\vec{r}) = \frac{1}{2m_e^2 c^2} \frac{1}{r} \frac{\partial V}{\partial r} \quad (3.30)$$

$\hat{L}$  and  $\hat{S}$  are the orbital and spin angular momentum operators (in the unit of  $\hbar$ ), and  $\xi(\vec{r})$  is the spin-orbit coupling constant (that is normally decaying faster with increasing distance). The spin-orbit coupling can be included as a perturbation in the scalar relativistic Hamiltonian Eq. (2.17) with a self-consistent treatment of spin-orbit contribution at each variational step.

Magnetic anisotropy can be defined as the change of the total energy of a magnetic system as a function of the orientation of the magnetization  $\vec{M}$  with respect to the crystalline axes. This means that there are some unique directions in space in which

a magnetic material is easy or hard to magnetized. Fig. 3.5 illustrates the procedure to calculate the MAE for different values of  $\vec{M}$ . For 1D system, we define the MAE in the following form

$$E_{MAE}(\theta, \phi) = E(\theta, \phi) - E(0, 0), \quad (3.31)$$

where  $\theta$  and  $\phi$  are the polar and azimuthal angles, respectively [see Fig. 3.5], and

$$E_{MAE}(\theta, \phi) = \sum_{i=1}^N K \sin^2 \varphi_i \quad (3.32)$$

where  $K$  stand for the anisotropy energy constant and  $\varphi_i$  is the angle between the easy axis and the local moment at lattice position  $i$ . A positive anisotropy constant  $K$  corresponds to an easy axis along the *chain*-direction, while a negative of  $K$  corresponds to an easy plane perpendicular to the *chain*-direction.

According to Bruno's model [88] which based on second-order perturbation theory, the MAE induce due to spin-orbit interactions is proportional to the anisotropy of the orbital moment. Thus, anisotropy energy can be written as

$$E_{MAE} = -\frac{\xi}{4\mu_B} \Delta L \quad (3.33)$$

where  $\Delta L$  are the difference in orbital moments between the easy and hard axis. In other words, this approach lies in the analysis of the variation of orbital moments (also called orbital anisotropy) between two quantization axes.

## 3.4 External electric fields

An external electric field (EF) induces charge distributions corresponding to a screening charge density at the the metallic surface. In the case of magnetic metals (e.g., FM Ni surface), this gives rise to modifications of the spin imbalance at the Fermi level with respect to the equilibrium state [89]. Since the screening charges at the surface are spin-polarized they can influence almost any magnetic properties of the system, for example the spin moments, the anisotropy energy, the orientation of magnetization  $\vec{M}$  with respect to the crystal structure or surface [21], the exchange interactions [90], etc. In the recent paper, Negulyaev *et al.* showed that the Mn dimer on Ni(100) has multi-stable magnetic ground states in the presence of an external EF [90]. In this work, both collinear and noncollinear magnetic orders were taken into account. In collinear case,

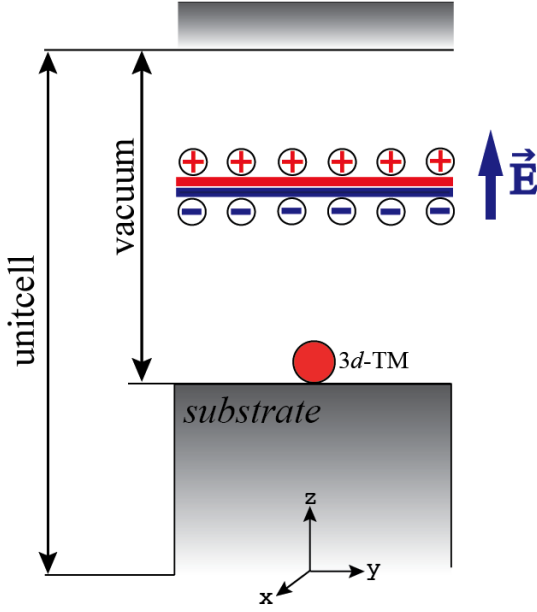


**Figure 3.6:** Illustration of a unit cell under the influence of the external electric field (EF). The dipole layer is placed in the middle of the vacuum space. The EF is applied perpendicular to the substrate along the  $z$  direction, while the  $3d$  TM linear chain is periodic in  $x$  direction.

the FM order is more favorable in the absence of EF. When the dimer is exposed to an external EF, the exchange energy changes dramatically. Negative (positive) values of the EF favor the FM (AF) order. In the case of NC calculations, noncollinearity is destroyed by a negative EF, while a positive EF sustains the noncollinear alignment with an angle of about  $116^\circ$  between NN spins.

In the present work, we are interested in investigating the effect of the external EF on the electronic and magnetic properties of  $3d$  TM chains including collinear and noncollinear magnetic configurations.

In supercell DFT calculations, an external EF can be introduced by adding a dipole layer in the vacuum region in the middle of the unitcell [81]. A schematic diagram of the static uniform external EF applied perpendicular to a slabs is shown in Fig. 3.6. An external EF introduces a potential  $V(z) = E_z z$ , as a result the electronic potential along the  $z$  direction is strongly modified. The charge distribution is therefore modified by keeping the charge neutrality of the whole system. Positive (negative) values of  $E_z$  refer to outwards (inwards) direction of the fields with respect to the surface [see Fig. 3.6]. An alternative approach to include the external EFs is to introduce point charges  $Q$ . Similar to dipole layer method, the charge neutrality of the supercell is preserved by means of compensating background charges. Here, the  $Q > 0$  ( $Q < 0$ ) refers to the added (depleted) electrons per unit cell [21].

The change in KS Hamiltonian introduced by the external EF is given by

$$\Delta H = \phi_{ext}(\vec{r}) - \phi_o, \quad (3.34)$$

where  $\vec{E}(\vec{r}) = -\vec{\nabla}\phi_{ext}(\vec{r})$  and  $\phi_0$  describes the interaction between  $\phi_{ext}$  and ionic pseudopotentials. Therefore, the additional external electrostatic potential term in the Hamiltonian modifies the free-energy functional  $F_{HK}$  [Eq. (2.8)] to

$$\tilde{F}[n(\vec{r})] = F_{HK}[n(\vec{r})] + \Delta E[n(\vec{r})], \quad (3.35)$$

where the change in energy  $\Delta E[n(\vec{r})]$  is written as

$$\Delta E[n(\vec{r})] = -e \int \phi_{ext}(\vec{r}) n(\vec{r}) d\vec{r} + e \sum_i Z_i \phi_{ext}(\vec{R}_i). \quad (3.36)$$

In the above equation  $Z_i$  and  $\vec{R}_i$  stand for the atomic number and position of the  $i$ th ion core. According to this method, the total energy of the system changes due to the external EF.

## 3.5 Technical details

As discussed section 2.4, our investigations are performed in the framework of density functional theory as implemented in the Vienna *ab-initio* simulation package (VASP) [78]. Noncollinear magnetism is treated within a fully unconstrained formalism [80].

To compute the forzen-magnon dispersion relation in TM chains, the spiral SDWs are constructed using the supercell approach by constraining the local moment  $\vec{\mu}_i$  at each atom  $i$  with different values of spin wave vector  $q$ . Consequently, for small  $q$ , one needs a large unit cell of length  $Na$ , being  $N$  is the number of atoms in the supercell and  $a$  is the nearest-neighbor distance [see Fig. 3.1 (a)]. In the present study, the calculations are performed by exploiting the generalized Bloch theorem (GBT) as discussed in section 3.1.3. Additionally, a large unit cell is considered for the analysis of the local  $d$ -electron density of states  $\rho_{i\sigma}^d(\varepsilon)$  and magnetization density.

The MAE has been calculated using the so-called *force theorem*. In this method one computes the total energy difference between the single-particle KS eigenvalues corresponding to the two involved orientation of  $\vec{M}$ . These calculations are less demanding than the self-consistent ones. Since the MAE is a very small quantity (of the order of a few meV), a large plane-wave energy cutoff  $E_{max} = 500$  eV and a dense value of  $\vec{k}$ -mesh, which depends on the system, are required in order to ensure the accuracy of the calculations.

An external EF is applied by introducing a planar dipole layer inside the vacuum region as discussed in Ref. [81]. The calculations of the spiral SDWs in the presence of the external EF are performed self-consistently using a large supercell cell as described in section 3.4. As discussed previously, the GBT does not hold in the presence of the external EF or if SOC is taken into account, since the atoms with different magnetization directions are not equivalent anymore, and therefore the roto-translational symmetry is broken. The calculated results are presented in chapter 6.

# Spiral spin-density waves in $3d$ transition-metal monoatomic chains

In this chapter, we investigate the electronic and magnetic properties of one-dimensional  $3d$  TM (V, Mn and Fe) nanowires from a first-principles prospective within the framework of density functional theory. The stability of various collinear and noncollinear spin arrangements is analyzed in terms of the forzen-magnon dispersion relation. The dependence of the local magnetic moment  $\mu$  as a function of spin wave vector  $q$  is discussed, which reveals the itinerant character of the magnetism of the nanowires. The electronic structures of the wires are analyzed by comparing the density of states  $\rho_{i\sigma}^d(\varepsilon)$  for different representative values of  $q$ . The effect of structural variables such as the interatomic distance  $a$  on the stability of noncollinear solutions has been investigated. The resulting effective exchange parameters  $J_{ij}$  between the local magnetic moments are discussed in the context of a simple classical Heisenberg spin model.  $J_{ij}$ -phase diagrams are calculated to analyze their relative stability from a phenomenological perspective.

## 4.1 Introduction

Despite its long history the magnetism of low-dimensional systems such as nanowires, ultrathin films, and nanostructures has recently gained considerable attention for basic science and applications. Understanding these magnetic systems would allow us to take advantage of their novel properties and to design new materials with the desired characteristic. Indeed, a wide variety of studies have been performed, which range from experimental and theoretical basic studies all over to material-science de-

velopments geared to specific technological purpose. Particular attention design non-volatile magnetic random access memories or recording heads for ultrahigh-density hard-disk drives and spintronic devices [2, 13, 14, 91–95]. In this context, 3d TM ultrathin films and nanowires deposited on non-magnetic substrates are expected to yield non-magnetic structures due to hybridization between the  $d$ -orbitals and the metal substrate (e.g., Cu, Pd, Pt). Novel experimental techniques have been developed such as spin-polarized STM and diffusion-controlled aggregation, which are capable to investigate the magnetic structures at the nanoscale and even atomic level. A variety of nanostructures including small particles, 1D TM nanowires, and 2D islands of various sizes can be created at surfaces by STM manipulation. Making used of these techniques, experimental investigations performed on atom-by-atom engineered structures have revealed a number of interesting effects, such as the enhancement of orbital magnetism and magnetic anisotropy [2, 4], long-range atomic ordering of adatoms [5, 44], non-collinear spin arrangements, quantum confinement, and self-alignment of local moments in nanowires [8]. Consequently, 1D magnetic nanostructures define a fascinating research field, where a number of current fundamental experimental and theoretical interests converge.

Most recently, experimental and theoretical investigations have revealed that the significant reduction in dimensionality of 1D 3d TM nanowires, can lead to a wide spectrum of interesting properties, in particular, large magnetic anisotropy, short-range and long-range exchange interactions and NC magnetic structures. Moreover, low-dimensional magnetic systems offer new possibilities to control the magnetic order, which sensitively depends on the geometrical structure. Besides the well-know collinear magnetic spin-arrangements, a large variety of complex NC structures exist (e.g., spin spiral density waves or skyrmion) [36]. For instance, Zelený *et al.* [40] have explored the NC magnetic order of manganese nanostructures, from nanowires to nanorods consisting of 6-Mn atoms, in which the magnetic moments are rotated by  $120^\circ$  between nearly neighbor atoms. They found that Mn nanowires have a NC magnetic ground state instead of spin-spiral configurations. Saubanère *et al.* [41] investigated the stability of spiral SDWs in V wires for different values of the NN distance  $a$ . They revealed that V wires develop stable NC spiral magnetic state at  $a < 2.55 \text{ \AA}$ . In this case, noncollinearity is mainly the consequence of competing FM and AF couplings between first and second NNs. Furthermore, Tung *et al.* [42] and Schubert *et al.* [43] extended these investigations in various directions. However, in all these studies the effects of spin-orbit coupling have been neglected. Very recently, spin-polarized STM experiments on finite biatomic Fe chains on the  $(5 \times 1)$ -Ir(001) surface have revealed that the Fe chains show a noncollinear magnetic ground state. These results are in excellent agreements with DFT calculations [36]. Both studies conclude that the antisymmetric DMI is the driving force for the formation of the spin-spiral.



Noncollinear arrangements are often the result of magnetic frustrations such as AF NN interactions in non-bipartite lattices or competing FM and AF interactions between atoms at different distances. Previous theoretical studies using DFT have succeeded in describing SDW states in itinerant-electron magnetic materials such as bulk Cr,  $\gamma$ -Fe, and U compounds [22–25]. Even in systems that are usually ferromagnetic, for example Fe, Co, and Ni, spin-spiral orders have been predicted to become stable under certain conditions (e.g., particular structures at high pressure) [26].

The spiral SDWs in low-dimension magnetic systems are of special interest from a fundamental prospective, which can provide important information for characterizing the magnetic materials and their structures. Many parameters such as the exchange and dipolar interactions, magnetic anisotropies and applied electric and magnetic fields can affect the behavior of the spin-waves. Moreover, the spin-spiral structures can also be useful to simulate some effects of temperature-induced spin fluctuations in the adiabatic approximation by analyzing the excitation energy spectrum, particularly at very low temperatures where long-wavelength magnons dominate. In this context, a number of theoretical and experimental studies have been performed which provide information related to the temperature variation at a particular energy level. Another examples of spin-spiral structures are the magnetic domain walls (DWs) in FM and AF materials, which have always attracted considerable experimental and theoretical attention, ever since the pioneering works of Bloch and Néel [31, 74]. Therefore, understanding the physics of noncollinear structures is crucial to numerous applications.

The aim of this chapter is to investigate the stability of noncollinear spiral magnetic order in 1D  $3d$  TM nanowires. Here, we focus on V, Mn and Fe nanowires as important representative examples of  $3d$  metals, because we expect that these elements might have a tendency to stabilize the noncollinear spin arrangements in the low dimensional regime. In section 4.2, the considered model of spiral SDWs in the  $3d$  monoatomic chains is presented together with the theoretical background. The structural, electronic and magnetic properties are analyzed in section 4.3 from the local prospective. Finally, in section 4.5 the conclusions are given

## 4.2 Simulation model and Computational details

A flat spiral SDW in infinite free-standing  $3d$  TM chains, defined by their wave vector  $\vec{q} = [0, 0, 2\pi/(Na)]$ , is simulated within a supercell approach by constraining the direction of the local magnetic moment  $\mu_i$  at each chain atom  $i$  as discussed in section 3.1.1, being  $N$  number of atoms in the supercell and  $a$  is the nearest-neighbor distance. For each integer  $N \leq 16$  all the spiral SDW vectors  $\vec{q}$  compatible with the supercell period-

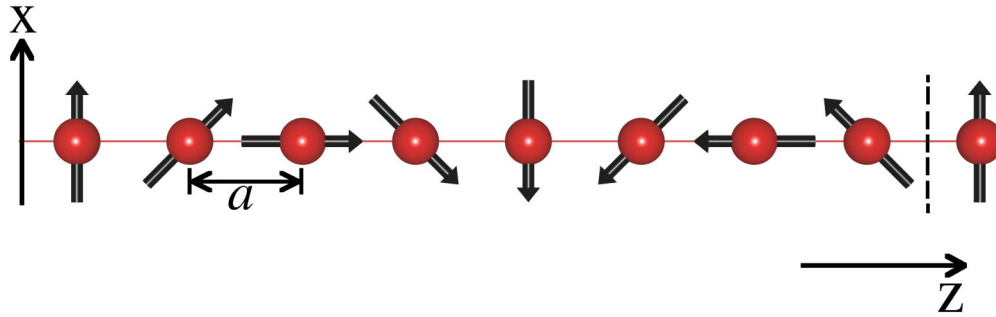


**Figure 4.1:** Illustration of a spiral spin-density wave having a wave vector  $\vec{q} = (0, 0, \pi/4a)$  with periodic length  $|\lambda| = 8a$  in a chain of atoms and spin polarization within the  $xz$  plane.

icity are considered, i.e.,  $q = 2\pi n/(Na)$  with  $0 \leq n < N$  and [see Fig. 4.1]. The others  $q$ -values laying between  $q = 0$  (FM) and  $q = \pi/a$  (AF) are the NC spiral magnetic arrangements. The supercell dimensions perpendicular to the wire are large enough to avoid any interaction with periodic replicas. In practice, 16 Å is found to fulfil this condition.

The present calculations have been performed in the framework of Hohenberg-Kohn-Sham DFT, as implemented in Vienna *ab-initio* simulation package (VASP) [78]. The exchange and correlation (XC) energy-functional is treated by using Perdew and Wang's spin-polarized generalized-gradient approximation (GGA) [71]. The spin-polarized Kohn-Sham (KS) equations are solved in an augmented plane-wave basis set, taking into account the interaction between valence electrons and ionic cores by means of the projector-augmented wave (PAW) method [75]. This is an efficient frozen-core all-electron approach, which takes into account the proper nodes of the valence KS orbitals in the core region and the resulting effects on the electronic structure and magnetic properties. For the present work the 4s, 4p and 3d orbitals are treated as valence electrons. The KS wave functions are expanded in the interstitial region in a plane wave basis set with a cut-off energy  $E_{max} = 500$  eV. The integrations in the Brillouin zone (BZ) are performed by using the Monkhorst-Pack scheme with a  $k$ -mesh of  $1 \times 1 \times 120/N$  points [79], which has been checked to yield accurate results for the present systems. Test calculations with higher cut-off energies and additional  $k$  points have shown that these values are a good compromise between accuracy and computational effort. The accuracy of our calculations, for example in the total energy, is estimated to be 1 meV/atom or better. For metallic-like systems, one often finds very rapid variations of the states close to the Fermi level  $\varepsilon_F$  that may cause a poor convergence of the relevant physical quantities such as the total energy or the local magnetic moments. Therefore, a smearing of the KS levels is introduced in order to improve the numerical stability. Here, we use a Gaussian smearing with a width  $\sigma = 0.02$  eV, a value that ensures that the smearing contribution to the total energy is less than

$10^{-4}$  eV/atom. The criterion for the energy convergence has been set to  $10^{-5}$  eV and the force on each atom less than  $10^{-2}$  eV/Å.

## 4.3 Interplay between magnetic and electronic properties

### 4.3.1 V monoatomic chains

In order to investigate the stability of noncollinear magnetism in V nanowires we determine the frozen-magnon dispersion relation  $\Delta E(q) = E(q) - E(0)$  for spiral spin arrangements as a function of the SDW vector  $q$ . Results for the magnetic excitation energy  $\Delta E(q)$  referred to the corresponding FM state ( $q = 0$ ) are reported in Fig. 4.2 (a). Several representative values of the lattice parameter  $a$  are considered in order to simulate some of the effects of interaction between the wire and a substrate or ligand environment.

For large  $a$  ( $a \geq 2.6$  Å) the simplest FM state is the most stable magnetic order. However, as the NN distance decreases below  $a \simeq 2.55$  Å there is a finite range of SDW vector  $0 < q < \pi/a$  for which the noncollinear spiral spin arrangements are more stable than both collinear FM or AF states. This is a quite remarkable effect which can not be inferred from the available collinear FM and AF calculations [86]. Notice that despite the spiral instability, the FM order remains more stable than the AF order over a wide range of lattice parameters. Only for very short NN distances  $a < 2.4$  Å the AF order becomes more stable than the FM order, actually as long as the local magnetic moments are not strongly reduced ( $\mu_i = 0 \forall i$  if  $a \leq 1.9$  Å). Quantitatively, the energy gained upon the formation of the spiral state with the optimal  $q = q_{min}$  is relatively small:  $\Delta E(q_{min}) = 2$  meV/atom with  $q_{min} \simeq \pi/4a$  for  $a = 2.55$  Å and  $\Delta E(q_{min}) = 25$  meV/atom with  $q_{min} \simeq \pi/2a$  for  $a = 2.05$  Å. For comparison, notice that the excitation energy to the AF state, which measures basically the strength effective exchange coupling between first NNs, is in general much larger (e.g.,  $\Delta E(\pi/a) = 121$  meV/atom for  $a = 2.55$  Å). The stability of the spiral state is therefore the result of the interplay between competing interactions between local moments at different distances. The subtlety of the underlying itinerant-electron origin of these effective magnetic interactions suggests that they should be quite sensitive to external parameters and interactions. It is therefore important to investigate how the stability of spiral states are affected by other contributions such as wire-substrate interactions or magnetic anisotropy.

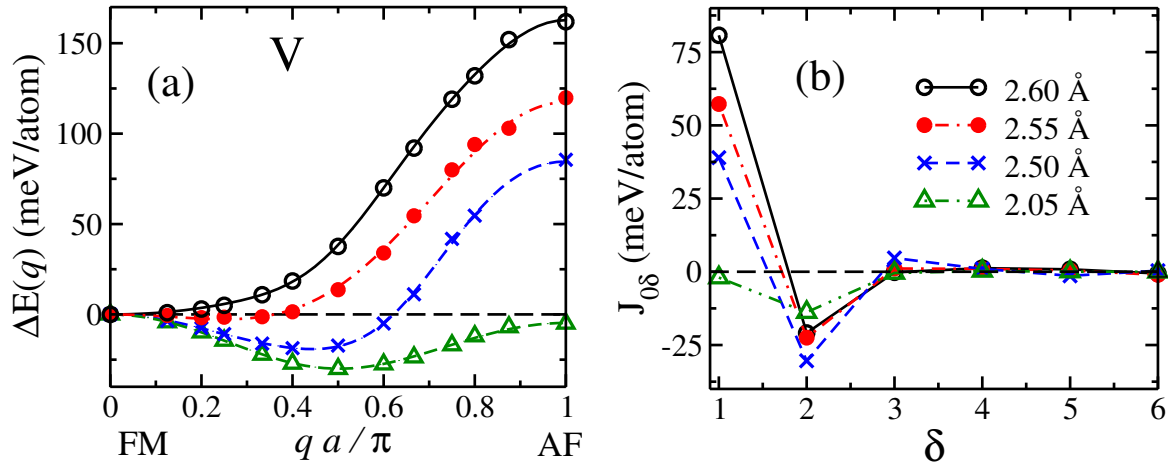


**Figure 4.2:** (a) Frozen-magnon dispersion relation  $\Delta E(q) = E(q) - E(0)$  of infinite V chains. The symbols refer to the *ab initio* results and the curves to the fit obtained by a classical Heisenberg model with exchange coupling  $J_{0\delta}$  (3.16). (b) Effective exchange interactions  $J_{0\delta}$  between a local moment  $\hat{\mu}_0$  and its  $\delta$ th nearest neighbor  $\hat{\mu}_\delta$  as a function of  $\delta$ . Results are given for representative values of the lattice parameter  $a$  as indicated.

Figure 4.2 (b) presents the calculated effective interactions parameters  $J_{0\delta}$  in the V monoatomic wires as a function of  $\delta$ th nearest neighbors. At relaxed FM NN distance ( $a = 2.6 \text{ \AA}$ ),  $J_{01}$  has a large positive value of 81 meV/atom, which suggests that the interaction tends to align the local magnetic moments  $\mu$  in the same direction (FM coupling). In contrast,  $J_{02}$  shows a relatively small negative value of  $-20$  meV/atom, indicating that the interaction with the second NNs tends to reverse the moment direction (AF coupling).  $J_{03}$  is also negative, but its value is one order of magnitude smaller than those of  $J_{01}$  and  $J_{02}$ , which indicates that the 3rd NN interaction has a negligible influence. Finally, we conclude that the FM coupling is the result of the competing interactions  $J_{01}$  and  $J_{02}$ . Moreover, we notice that under certain compression ( $a \leq 2.55 \text{ \AA}$ ), the positive  $J_{01}$  tends to decrease, whereas the negative  $J_{02}$  tends to increase in absolute value (i.e., compression weakens the FM interaction and strengthens the AF interaction). The resulting interplay between  $J_{01}$  and  $J_{02}$  stabilizes the noncollinear spin-spiral configurations. At even shorter NN distance  $a = 2.05 \text{ \AA}$ , the system is also magnetically frustrated due to the large negative value of  $J_{02}$  coupling which further stabilizes the spiral configurations. In all cases, we find that  $J_{01}$  and  $J_{02}$  are the dominant interactions, while  $J_{0\delta}$  for  $\delta \geq 3$  play a negligible role.

In Fig. 4.3, the modulus of the local magnetic moments  $\mu(q) = |\langle \vec{m} \rangle_{\text{ws}}|$  within the WS spheres is given as a function of  $q$ . For not too short NN distances one obtains large  $\mu$ , which are nearly saturated for the FM state state [ $\mu(0) = 3.2 \mu_B$  for  $a = 2.6 \text{ \AA}$ ] and decrease moderately and monotonously as  $q$  increases towards

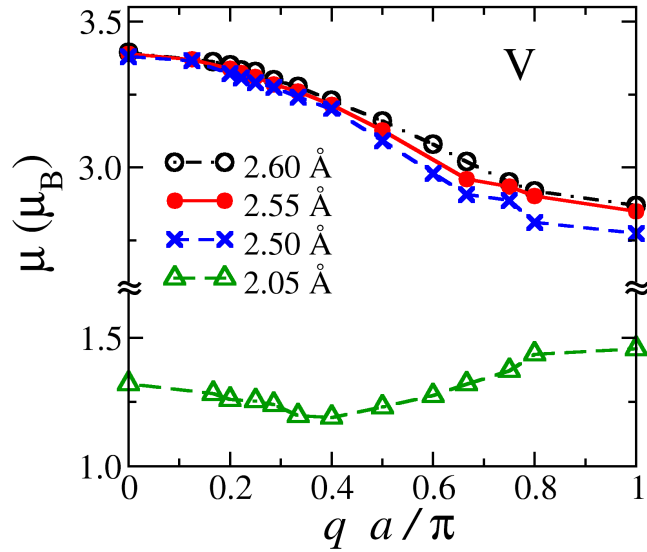


**Figure 4.3:** The variation of the magnitude of the local magnetic moments  $\mu$  within the Winger-Seitz (WS) cells as a function of the SDW vector  $q$ . Results are given for representative values of the lattice parameter  $a$  as indicated.

the AF state [ $\mu(\pi/a) \simeq 2.9 \mu_B$ ]. As the NN distance decreases we observe a sharp drop in the local moments due to the increasing  $d$ -orbitals hybridization and bandwidth [ $\mu(0) = 1.3 \mu_B$  for  $a = 2.05 \text{ \AA}$ ]. It is in this non-saturated regime that the stability of the spiral order becomes most important. Here the  $q$  dependence of  $\mu_i$  is weaker and non-monotonous [see Fig. 4.3]. Notice that for the energetically optimal  $q_{min} \simeq \pi/2a$  the local moments are minimal. This suggests that the stability of the spiral states is driven by kinetic or hybridization effects rather than by local exchange contributions, since the latter should favor an enhancement of the local polarizations. In fact, an analysis of the spin polarization vector  $\vec{m}(\vec{r})$  shows that in the present GGA approximation the spin density is essentially collinear within each WS sphere, even for  $q = \pi/2a$  [41].

### Local electronic structure

To gain further insight on the properties of spiral states, it is interesting to investigate how the electronic structure depends on the noncollinearity of the magnetic arrangement, to this aim we have calculated spin-polarized local  $d$ -electron DOS  $\rho_{i\sigma}^d(\varepsilon)$  of V chains at NN distance  $a = 2.55 \text{ \AA}$ . The results are given for representative wave numbers  $q$  in Fig. 4.4. The DOS of the collinear FM and AF states are also shown for the sake of comparison. In order to obtain  $\rho_{i\sigma}^d(\varepsilon)$  we first calculate the  $3d$ -electron DOS  $\rho^d(\vec{r}, \sigma, \varepsilon)$ , which is projected on the position  $\vec{r}$  and on the spin components up and down ( $\sigma = \uparrow, \downarrow$ ) taking the direction of the local magnetic moment  $\vec{\mu}_i$  at atom  $i$  as the spin-quantization axis. The up and down spin components should actually be understood as majority- and minority-spin projections at any atom  $i$ . Subsequently, the DOS  $\rho^d(\vec{r}, \sigma, \varepsilon)$  is integrated within the WS sphere of atom  $i$  in order to obtain

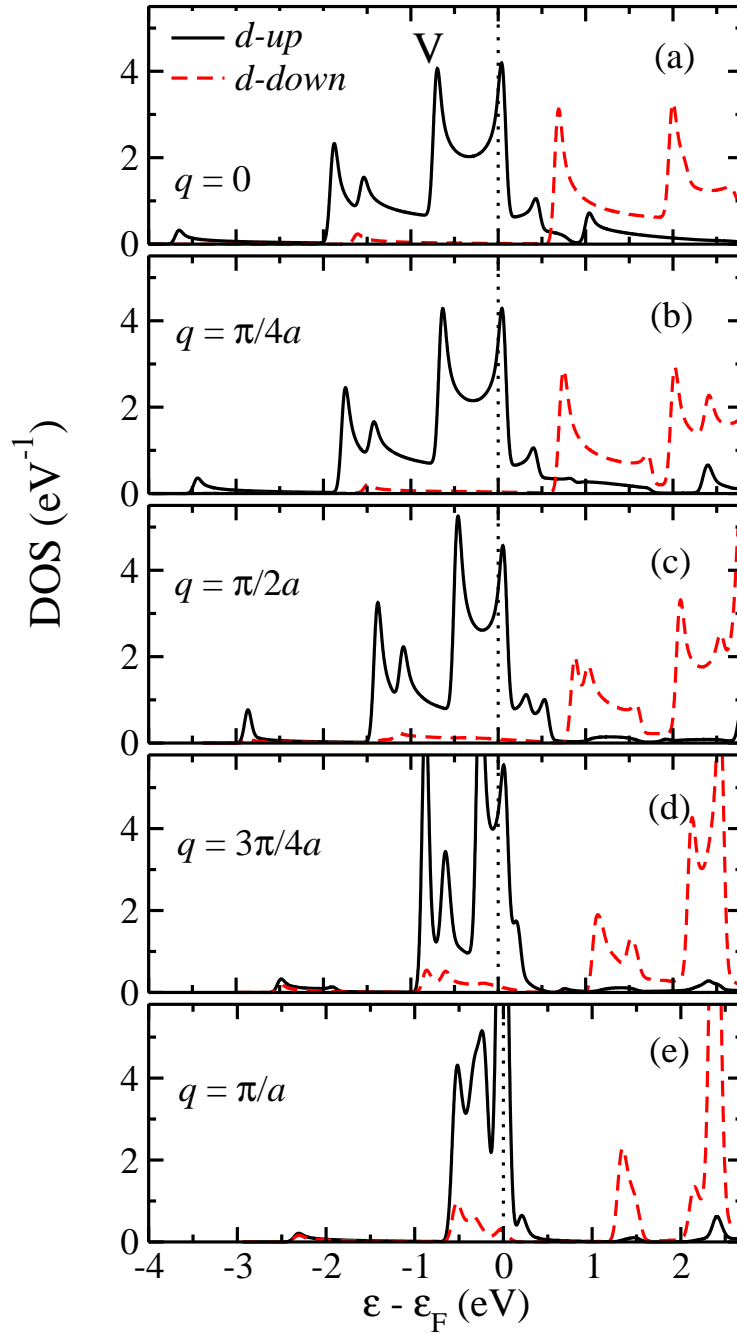


**Figure 4.4:** Local  $d$ -electron density of states (DOS)  $\rho_{i\sigma}^d(\varepsilon)$  of free-standing V chains having NN distance  $a = 2.55 \text{ \AA}$ , for representative SDW vectors  $q$ . Results are given for the majority-spin (full lines) and minority-spin (dashed) components along the direction of the local magnetic moment  $\vec{\mu}_i$ . The Fermi energy  $\varepsilon_F$  is indicated by the vertical dotted lines.

the spin-polarized local DOS  $\rho_{i\sigma}^d(\varepsilon)$ . Since the magnetic order of the assumed spiral SDWs is roto-translational invariant for all  $q$ , the thus obtained local DOS are strictly the same at all atoms. A translation of the orbital coordinates by  $a$  along the wire, followed by a rotation of the spin coordinates by an angle  $\theta = qa$  around the axis of the wire, leaves the electronic states unchanged. Therefore, the result for  $\rho_{i\sigma}^d(\varepsilon)$  can be compared for different  $q$  and lattice structures. The qualitative similarities between the  $q = 0$  (FM) and  $q$ -dependent DOS are quite remarkable, particularly for the occupied states. It seems that in first approximation these DOSs can be related by a simple band-width scaling. As we move to larger values of  $q$  the changes in DOS become more significant [see Fig. 4.4 (c)-(e)]. Notice in particular the depletion of KS states in the  $q = \pi/a$  (AF) DOS just above the Fermi energy,  $\varepsilon - \varepsilon_F = 0.3\text{--}1.3$  eV, and for  $\varepsilon - \varepsilon_F = 1.8\text{--}2.0$  eV, forerunners of which can be recognized already in the  $90^\circ$ -spiral DOS. Concerning the width  $W = \varepsilon_F - \varepsilon_b$  of the occupied band we observe a monotonic decrease with decreasing spiral wave length:  $W = 3.61$  eV,  $3.48$  eV,  $2.94$  eV,  $2.56$  eV, and  $2.47$  eV for  $q = 0, \pi/4a, \pi/2a, 3\pi/2a, \text{ and } \pi/a$ , respectively. This explains qualitatively the monotonic increase of the magnon energy  $\Delta E(q)$  with increasing  $q$  [see Fig. 4.2]. Finally, a common feature of the DOS for all  $q$  is the high degeneracy at the Fermi level. This is likely to be the source of structural instabilities and symmetry breaking, for example, as a result of spin-orbit interactions or hybridizations with a metallic substrate.

### Magnetization density

Another interesting aspect which has been less explored that enables to further understand the spin-spiral waves stability is the local magnetisation distribution. The magnetisation density  $\vec{m}(\vec{r})$  inside the PAW spheres of each atom where the local moment  $\mu$  deviates from the parallel (collinear) alignment to NC magnetic configuration is obtained. In Fig. 4.5 (a), we display the graphical representation of  $\vec{m}(\vec{r})$  combined with charge density (background contour plot) in the vicinity of the spin-spiral arrangement having  $q = \pi/2a$  in V wires. Here, blue spheres represent the position of V chain atoms and small black arrows indicate the direction of the local magnetization around each atom. For collinear FM order,  $\vec{m}(\vec{r})$  is pointing in the same direction everywhere in space, whereas for NC configuration, the direction of  $\vec{m}(\vec{r})$  is allowed to vary freely in space. In fact, most applications of NC SDFT to date are based on this idea [22, 24, 96]. We find that the local magnetization vectors remain almost parallel within the WS spheres around each atom in which the magnitude of  $\vec{m}(\vec{r})$  is relatively high and supporting the usual picture of assigning a net direction for the magnetization or magnetic domain to each atom. The noncollinearity of  $\vec{m}(\vec{r})$  of a spin-spiral is observed in the interatomic regions between two domains where the magnitude of

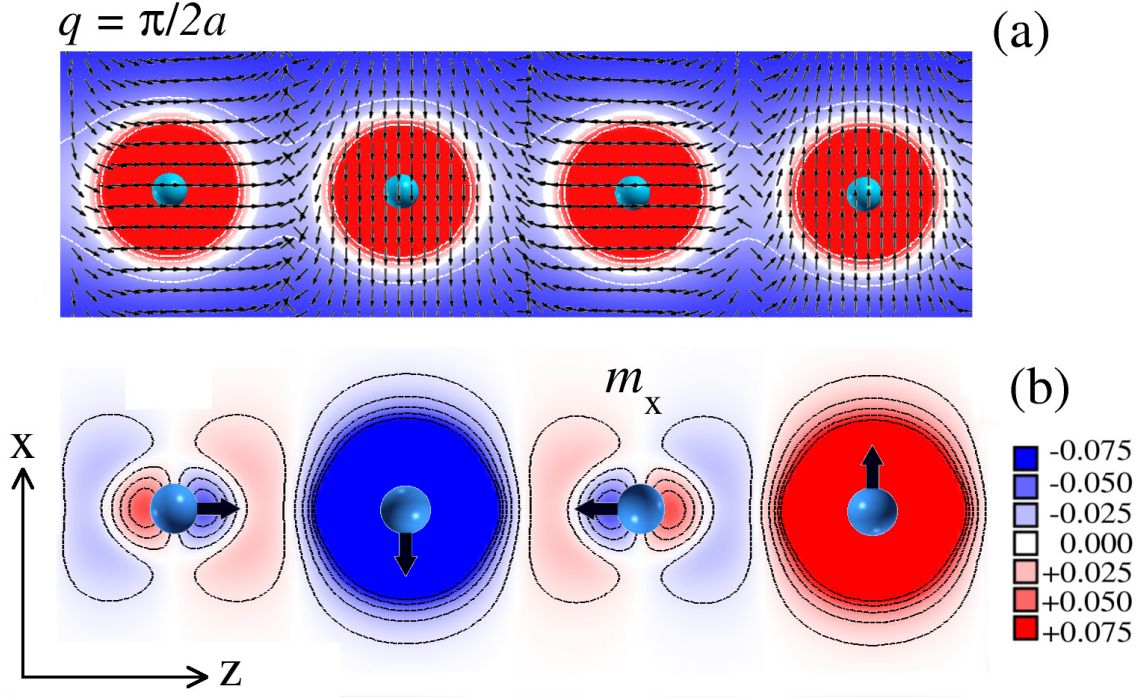


**Figure 4.5:** The magnetization density  $\vec{m}$  profile of spin spiral structure with wave vector  $q = \pi/2a$  in V linear chain.

$\vec{m}(\vec{r})$  is very weak. Similarly, in Fig. 4.5 (b), the magnetization density components  $m_x$  is shown. The results demonstrate that the magnetization  $m_x$  are highly localized around those atoms which are along the  $x$ -direction, whereas equally divided into  $m_x$ - and  $m_z$ -component when the local moment directed in the  $z$ -direction.

### 4.3.2 Mn monoatomic chains

In order to explore the formation of spiral SDWs in Mn chains, we have calculated the frozen-magnon dispersion relation  $\Delta E(q) = E(q) - E(0)$  for some representative values of  $a$  as shown in Fig. 4.9 (a). As a first step, we compute the optimal bond length of freestanding Mn nanowires by minimizing the energy as a function of NN distance  $a$  for fixed values of  $q$ . The calculated stress free lattice parameters for FM and AF order are  $a = 2.6 \text{ \AA}$  and  $a = 2.4 \text{ \AA}$ , respectively. These values are in good agreement with the earlier studies [40, 86, 97]. Moreover, it is analyzed that the FM governs for  $a \geq 2.6 \text{ \AA}$  while the AF arrangements are stabilized at shorter NN distances. The frozen-magnon dispersion relation  $\Delta E(q)$  corresponding to the FM equilibrium lattice parameter  $a = 2.6 \text{ \AA}$  is displayed in Fig. 4.9 (a). One observes that the spin-spiral structure is most stable having  $q_{min} \simeq 0.65\pi/a$  and the ground-state energy is



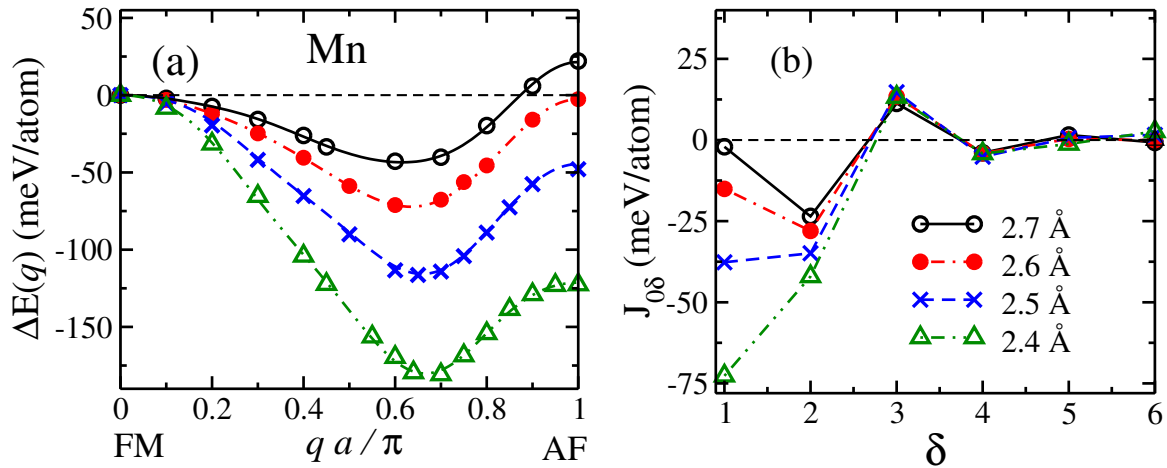


**Figure 4.6:** (a) Frozen-magnon dispersion relation  $\Delta E(q) = E(q) - E(0)$  of infinite Mn chains. The symbols refer to the *ab initio* results and the curves to the fit obtained by a classical Heisenberg model with exchange coupling  $J_{0\delta}$  (3.16). (b) Effective exchange interactions  $J_{0\delta}$  between a local moment  $\hat{\mu}_0$  and its  $\delta$  the nearest neighbor  $\hat{\mu}_\delta$  as a function of  $\delta$ . Results are given for representative values of the lattice parameter  $a$  as indicated.

72 and 68 meV/atom lower than the corresponding FM and AF orders, respectively. Similarly, for  $a = 2.4 \text{ \AA}$ , the lowest energy minimum is found close to  $q_{min} \simeq 0.6\pi/a$ . In this case the corresponding energy is 176 meV/atom lower than the FM one. The magnon-dispersion relations over a wide range of  $a$  ( $2.4 \leq a \leq 2.7 \text{ \AA}$ ) are shown in Fig. 4.9 (a). One concludes that the stability of NC spin spiral orders increases by decreasing interatomic distance  $a$ . However, the energy difference  $|\Delta E(q)|$  between the FM and AF orders decreases with increasing  $a$  whereas the NC magnetic arrangements remain always more stable within the considered values of  $a$ .

The *ab initio* results can be interpreted in terms of exchange interactions  $J_{ij}$ . The obtained exchange interactions  $J_{0\delta}$  as a function of  $\delta$ th NNs by fitting  $\Delta E(q)$  are given in Fig. 4.9 (b). Positive (negative) values of  $J_{01}$  stand for ferromagnetic (antiferromagnetic) coupling. We find that first three NNs interactions terms play a leading role in order to figure out the magnetic ground states. The interaction  $J_{0\delta}$  beyond the third NNs is less important and can be neglected. Interestingly, the  $J_{01}$  depends strongly on the lattice parameter  $a$ . Its strength decreases by increasing the NN distance  $a$  between the consecutive Mn atoms. The value of  $J_{02}$  is much less affected by changing the value of  $a$ , whilst  $J_{03}$  remains merely constant in the considered range  $2.4 \leq a \leq 2.7 \text{ \AA}$ . This trend can be qualitatively understood in terms of a reduction in the orbital overlapping when the distance between the Mn atoms is increased. Noncollinear magnetism in Mn monolayers and nanowires have been intensively discussed in the previous theoretical and experiment studies [40, 42, 43]. The aim of this work has been to provide a more

detailed analysis and, and to allow a direct comparison of the stability of spiral SDWs in 3d TM nanowires by increasing the 3d-band filling.

### Local electronic structure

The purpose of this section is to investigate the electronic structure of Mn wires as a function of wave vector  $q$ . Fig. 4.7 shows the calculated the spin-polarized  $d$ -electron local DOS  $\rho_\sigma^d(\varepsilon)$  for few representative values of  $q$  at a NN distance  $a = 2.5 \text{ \AA}$ . In our analysis, we only present the spin-resolved local  $d$ -DOS of Mn atom because in NC magnetic configurations the electronic states are generally spin-hybridized. In the case of collinear spin i.e., when the relative angle between the spins is  $\theta = 0$  (FM) or  $\theta = \pi/a$  (AF), there is no mixing between the up and down spins states. In the case of  $\theta = 0$  (FM) [see Fig. 4.7 (a)], one observes substantial wide peaks in the majority-spin DOS at about  $\sim 2.63 \text{ eV}$  below the Fermi energy  $\varepsilon_F$  as well as peaks in the minority-spin DOS at above  $\sim 1.2 \text{ eV}$  above  $\varepsilon_F$ . This is corresponding to strong ferromagnetic, in contrast to Mn bulk which is weak. The calculated exchange splitting between these states and the local magnetic moments are  $\sim 3.8 \text{ eV}$  and  $\mu \simeq 3.94 \mu_B$ , respectively. For NC spin arrangements when  $\theta$  lies in between the limit  $0 < \theta < \pi/a$ , two kinds of major changes can be expected in the electronic structures of a magnetic system. First, the noncollinearity destroys the spin projection as a good quantum number and tends to mix the opposite spin states. The mixing between the majority- and minority-spin bands increases and reaches its maximum when  $\theta = 0$  (FM) while reduces and approaches to zero as  $\theta$  goes to  $\pi/a$ . In result, mixing of these states in NC arrangements changes significantly the electronic structure (subbands). In order words, this mixing leads to the hybridizational repulsion of the bands which results to move the majority bands to the lower energy states and the minority bands to the higher energy states. The direct consequence of this interplay may decrease (lower) the energy of the system. Secondly, some features of the double-exchange mechanism and band narrowing can be presented as well. In spiral SDW configuration, indeed we observe a substantial reduction in the bandwidth  $W$  together with a shift in position of the majority and minority bands as  $q$  increases:  $W = 3.5, 3.2, 2.5, 2.0$  and  $1.8 \text{ eV}$  for  $q = 0, \pi/4a, \pi/2a, 3\pi/4a$  and  $\pi/a$  due to shifting of the majority- and minority-spin bands in opposite direction, respectively. Our calculated results demonstrate that the most pronounced changes of the calculated magnetic spin local DOS occur mainly in the energy range of  $\sim -4 \text{ eV}$  and  $-1 \text{ eV}$  below the Fermi energy  $\varepsilon_F$  between the spin-up and spin-down states by introducing the NC spin configurations. The sum of the one-electron energies is lower for the spiral SDW than the the FM and AF orders [40].

To further illustrate our discussion of 3d-DOS with the local electronic structure, we obtain the integrated DOS as a function of energy at the same NN distance  $a = 2.5 \text{ \AA}$

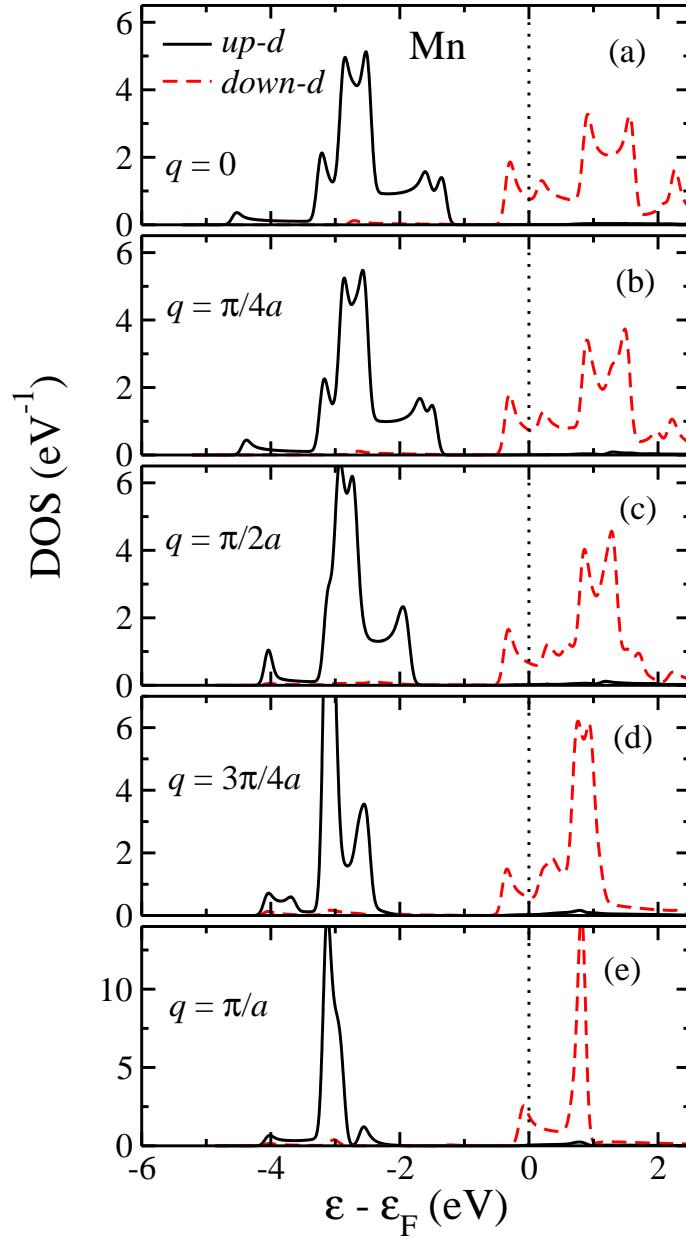


**Figure 4.7:** Local  $d$ -electron density of states  $\rho_{i\sigma}^d(\varepsilon)$  of free-standing Mn chains at a NN distance  $a = 2.5 \text{ \AA}$ , for representative SDW vectors  $q$ . Results are given for the majority-spin (full lines) and minority-spin (dashed) components along the direction of the local magnetic moment  $\vec{\mu}_i$ . The Fermi energy  $\varepsilon_F$  is indicated by the vertical dotted lines.

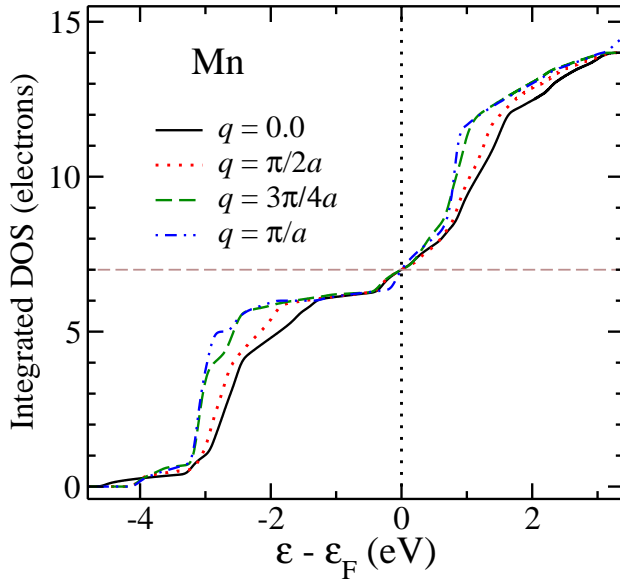


**Figure 4.8:** Integrated density of states (DOS) of free-standing Mn monoatomic chains at NN distance  $a = 2.5 \text{ \AA}$  for various wave vectors  $q$ . The Fermi energy  $\varepsilon_F$  is indicated by the vertical dotted lines.

for various wave vectors  $q$  [Fig. 4.8]. This can provide us a direct comparison of the electron distribution. The change in number of electrons is evaluated by integrating the local density of states by projecting the wavefunctions onto the spherical harmonics within the WS sphere around each atom. In other words, the integral area of  $d$ -DOS can be used to calculate the change in number of electrons for different values of  $q$ . As  $q$  increases, an enhancement in the number of electrons around 2.5 eV below the Fermi energy is determined. Since the total number of electrons are constant, such localization in the electronic distribution explains the bands narrowing and the onset of one single peak in the DOS when  $q$  increases. Thus, the DOS wave-vector dependence can be explained by an electron redistribution or re-arrangement of electrons in the majority- and minority-spin states.

### 4.3.3 Fe monoatomic chains

Similarly to our previous investigations, we calculate the frozen-magnon dispersion relation  $\Delta E(q) = E(q) - E(0)$  of Fe chains which provides a complete picture of stability the ground-state configuration with respect to spin-wave excitation spectrum. Our results reveal that a spiral SDW having  $q \simeq \pi/5a$  is the most stable magnetic order at the equilibrium NN distance  $a = 2.25 \text{ \AA}$ . The energy of the optimal spin-spiral arrangement is around 10 meV/atom lower than the FM order. In order to explore the effect of bond length changes on the stability of NC configurations, we present the magnon dispersion relation  $\Delta E(q)$  over a wide range of NN distances ( $2.0 \leq a \leq 2.5 \text{ \AA}$ ) [see Fig. 4.9 (a)]. Here, the symbols refer to the *ab initio* DFT results, whereas the curves are obtained by mapping the dispersion  $\Delta E(q)$  to the classical Heisenberg

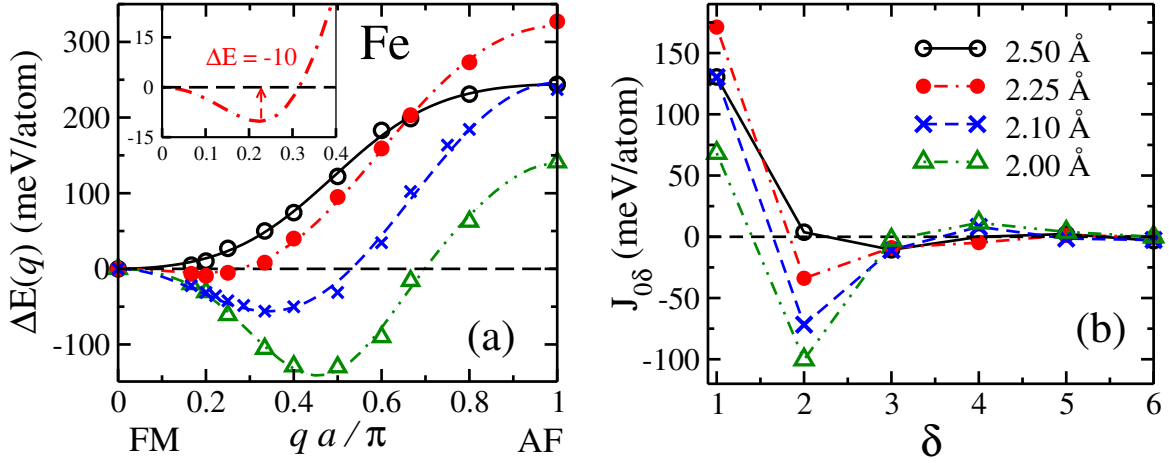


**Figure 4.9:** (a) Frozen-magnon dispersion relation  $\Delta E(q) = E(q) - E(0)$  of infinite Fe chains. The symbols refer to the *ab initio* results and the curves to the fit obtained by a classical Heisenberg model with exchange coupling  $J_{0\delta}$  [see Eq.]. (b) Effective exchange interactions  $J_{0\delta}$  between a local moment  $\hat{\mu}_0$  and its  $\delta$ th nearest neighbor  $\hat{\mu}_\delta$  as a function of  $\delta$ . Results are given for representative values of the lattice parameter  $a$  as indicated.

energy relation (3.16). A very good fit is obtained by considering sixth NN interactions into account. One concludes that the spiral SDWs are stabilize for  $a \leq 2.25$  Å, whilst the FM state is more favorable for larger NN distances.

The exchange couplings  $J_{ij}$  provide us local interpretation of the stability of the NC magnetic order, which can be derived from the *an initio* results by means of relation (3.16). First, at equilibrium bond length  $a = 2.25$  Å, we find that  $J_{01}$  is positive which favor FM alignment whilst  $J_{02}$  is negative and small in magnitude which tends to favor antiparallel alignment. The exchange interactions are thus magnetically frustrated. The competition between the nearest-neighbor  $J_{01} > 0$  and  $J_{02} < 0$  interactions leads to the stabilization of the NC spin arrangement. For large values of  $a$  (i.e.,  $a = 2.5$  Å,  $J_{01}$  dominates over all other terms and is preferred FM order. However, for short NN distance (i.e.,  $a = 2.1$  Å) the magnitude of  $J_{01}$  and  $J_{02}$  are comparable. This situation is more complex in order to figure out the stable magnetic ground-state of frustrated system when the NN and next NN are comparable. In fact, one needs to taken into account also the  $J_{03}$  coupling for the determination of the ground state. In order to gain further insight into the nature of these magnetic structures, we display in Fig. 4.10 (b) the average local magnetic moment  $\mu(q) = |\langle \vec{m} \rangle_{\text{WS}}|$  inside the WS spheres as a function of the  $q$  for different NN distances  $a$ . One observes that for all the relevant  $a$ , the magnitude of the local magnetic moments decreases monotonically as we go from the FM ( $q = 0$ ) to AF ( $q = \pi/a$ ) alignment.  $\mu(q)$  is equal to  $3.1 \mu_B$  and  $2.74 \mu_B$  for  $q = 0$  and  $q = \pi/a$  at NN  $a = 2.25$  Å, respectively. The decrease of

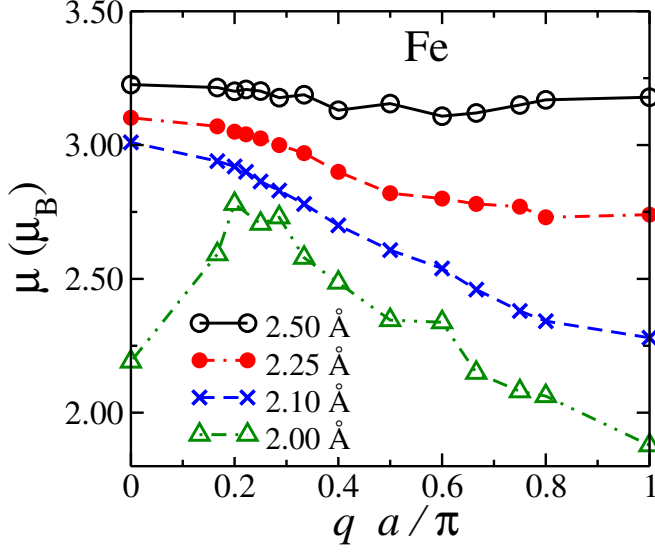


**Figure 4.10:** The variation of the magnitude of the local magnetic moments  $\mu$  within the Winger-Seitz (WS) cells as a function of the SDW vector  $q$ . Results are given for representative values of the lattice parameter  $a$  as indicated.

$\mu(q)$  is more pronounced for the shorter bond length due to the stronger hybridizations between the  $d$ -orbitals.

### Local densities of states

In order to insight the microscopic origin of the relative stability of NC spiral magnetic orders, we have calculated the spin-polarized  $d$ -electron local DOS  $\rho_\sigma^d(\varepsilon)$  of Fe chains at a NN distance  $a = 2.25 \text{ \AA}$ . The results are shown for some representative wave numbers  $q$ . In the case of FM ( $q = 0$ ) order, owing to the large number of electrons in the  $d$ -bands, one can see that the majority and minority states are slightly overlapped around  $\sim -1 \text{ eV}$  below the Fermi energy [see Fig. 4.11 (a)]. As the  $q$  increases, the majority and minority states tends to separate due to hybridization repulsion. Moreover, the width of the dominated bands decreases appreciably as we go from FM ( $q = 0$ ) to AF ( $q = \pi/2$ ) order. Concerning to the width  $W = \varepsilon_F - \varepsilon_b$  of the occupied band, we observe a monotonic decreases with decreasing spiral wave length:  $W = 3.61, 3.48, 2.94, 2.56,$  and  $2.47 \text{ eV}$  for  $q = 0, \pi/4a, \pi/2a, 3\pi/2a,$  and  $\pi/a$ , respectively.

A more detailed analysis of electronic states is possible by decomposing the  $d$ -resolved DOS in the different  $d$ -orbitals. Due to the symmetry of the chains (placed along  $z$ -direction) and in the absence of SO coupling the  $d$ -orbitals can be grouped in three sets of bands. The band  $dd\sigma$  formed by the  $d_{z^2}$  orbitals, the doubly degenerated  $dd\pi$  and  $dd\delta$  bands are formed by the  $(d_{xz}, d_{yz})$  and the  $(d_{x^2-y^2}, d_{xy})$  orbitals, respectively. For  $q = 0$  [see Fig. 4.11 (a')], one observes the characteristic of FM exchange splitting between up and down DOS. Each state has an important band widths. The  $dd\delta$  bands have narrowest width (around  $\sim 0.6 \text{ eV}$ ) because the corresponding orbitals

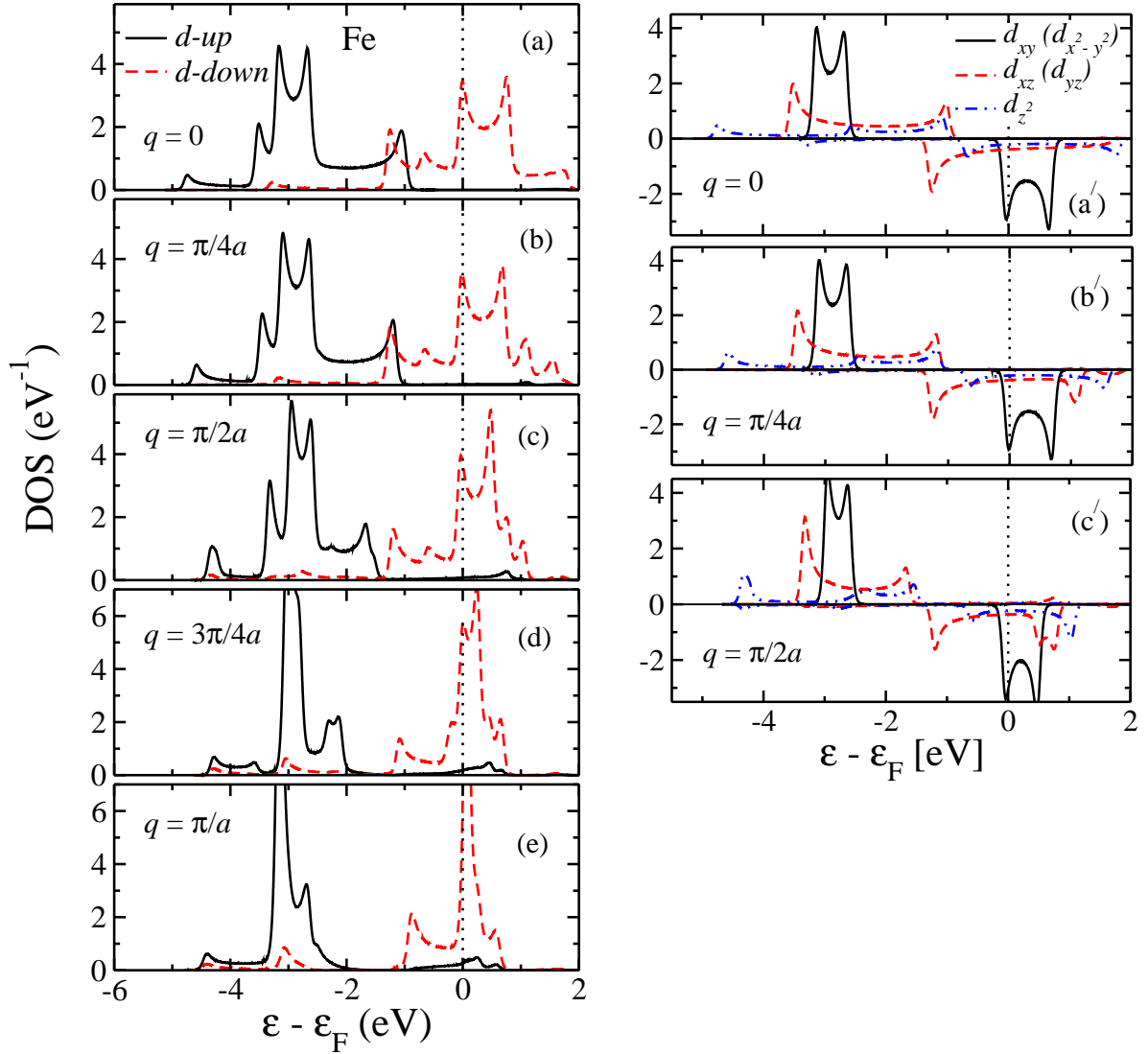


**Figure 4.11:** Local  $d$ -electron density of states (DOS)  $\rho_{i\sigma}^d(\varepsilon)$  of free-standing Fe chains having NN distance  $a = 2.25 \text{ \AA}$ , for representative SDW vectors  $q$ . Results are given for the majority-spin (full lines) and minority-spin (dashed) components along the direction of the local magnetic moment  $\vec{\mu}_i$ . The Fermi energy  $\varepsilon_F$  is indicated by the vertical dotted lines.

are perpendicular to the chain, whereas the  $dd\sigma$  bandwidth is large since the orbitals point along the chain direction. In the SDW configurations ( $q > 0$ ) the change in band widths as well as shifting of the majority and minority states in opposite direction around  $\sim -1$  eV below Fermi level  $\varepsilon_F$  have been observed. It is interesting to notice that the distance between these states increases because the majority-spin states are shifted to lower energies and the minority-spin states are moved towards the higher energies. Furthermore, the band-width of the  $dd\pi$  bands monotonically decreased with increasing  $q$  [see Fig. 4.11( $a'-c'$ )]. Therefore, the interband repulsion between opposite spin-projections states due to spiral wave vector  $q$  could be lower the total energy of the magnetic system and thus stabilized the NC spin configuration in Fe chains.

Figs. 4.12 (a-c) display the magnetization density  $\vec{m}(\vec{r})$  around each chain atom for the spin-spiral arrangements in which the local moments  $\mu_i = \mu [\cos(qa), 0, \sin(qa)]$  are rotated in the  $(x-z)$ -plane with  $\vec{q} = (0, 0, \pi/4a)$ . The angle between magnetic moments on neighboring atoms is  $45^\circ$ . We present the  $m_x$ - and  $m_z$ -components of magnetization because the local moment  $\mu_i$  rotates or propagates only in the  $xy$ -plane [see Fig. 4.12 (b)], whereas the  $m_y = 0$ . In other words there is no distribution of magnetization in the  $xy$ - or  $yz$ -planes. One analyzes that the magnetization are fairly well localized around each atom in the chains. For instance,  $m_x$ -component of the magnetization density of 1-atom only lies (localizes) in  $x$ -direction [see Fig. 4.12 (a)], whereas the  $m_z = 0$ . The magnetization components are equally divided for 2-atom and vice versa.



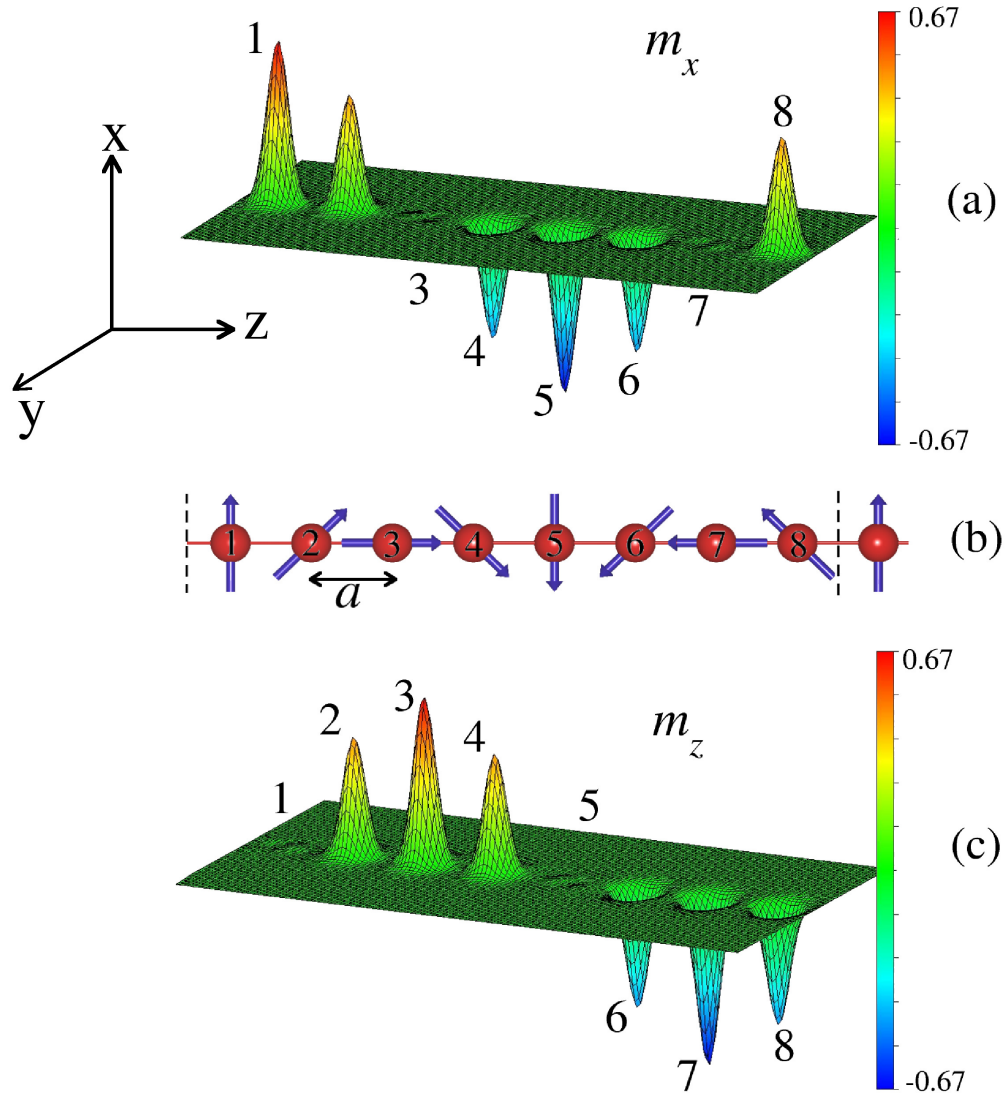


**Figure 4.12:** The first and third panels display the  $x$ - and  $z$ -components of magnetization density ( $m_x$  and  $m_z$ ), respectively. In the middle panel the arrows represent orientation of magnetic moments  $\mu_i$  of spiral SDW with wave vector  $\vec{q} = (0, 0, \pi/4a)$  at the equilibrium NN distance ( $a = 2.25 \text{ \AA}$ ). [Dotted line shows the size of supercell with 8-atoms periodicity of spin-spiral structures in  $z$ -direction with lateral dimensions along  $x$ - and  $y$ -direction about  $14 \text{ \AA}$ ].

## 4.4 Magnetic phase diagrams

Figures 4.14 and 4.13 display the magnetic phase diagrams of the classical Heisenberg model by taking the first-two and the first-three NN interactions  $J_{0\delta}$  into account as discussed in the Sec: 3.2.2. The phase diagrams provide us with a complete picture concerning to the stability of complex magnetic solutions. The corresponding results for  $J_{0\delta}$  in V, Mn and Fe monoatomic wires are also shown for few representative values of NN distances  $a$ . Each point in the phase diagrams corresponds to one dispersion relation for a given value of  $a$ . The calculated values of  $J_{01}$  and  $J_{02}$  at the equilibrium NN distances for V, Mn and Fe nanowires (underlined value of  $a$ ) lie in the SDW part of the phase diagram. For large value of  $a$ , one observes a transition from SDW to FM order in V and Fe chains. On the contrary, the NC magnetic configurations become more favorable under certain compression.

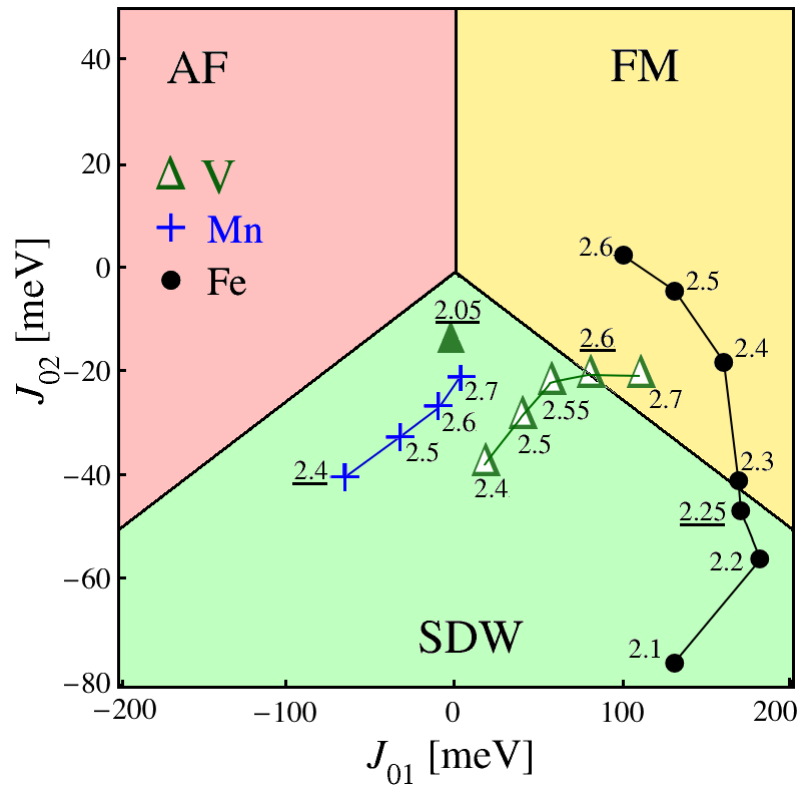


**Figure 4.13:** Magnetic phase diagram of the classical one-dimensional Heisenberg model with first and second NN interactions  $J_{01}$  and  $J_{02}$ . The regions of stable antiferromagnetic (AF), ferromagnetic (FM) and spiral spin-density wave (SDW) orders are shown. The symbols corresponding to the effective exchange couplings  $J_{0\delta}$ , which are derived from the *ab initio* calculations for V, Mn and Fe monoatomic chains. Different NN distance  $a$  are indicated in Å by the numbers. The equilibrium value of  $a$  is underlined

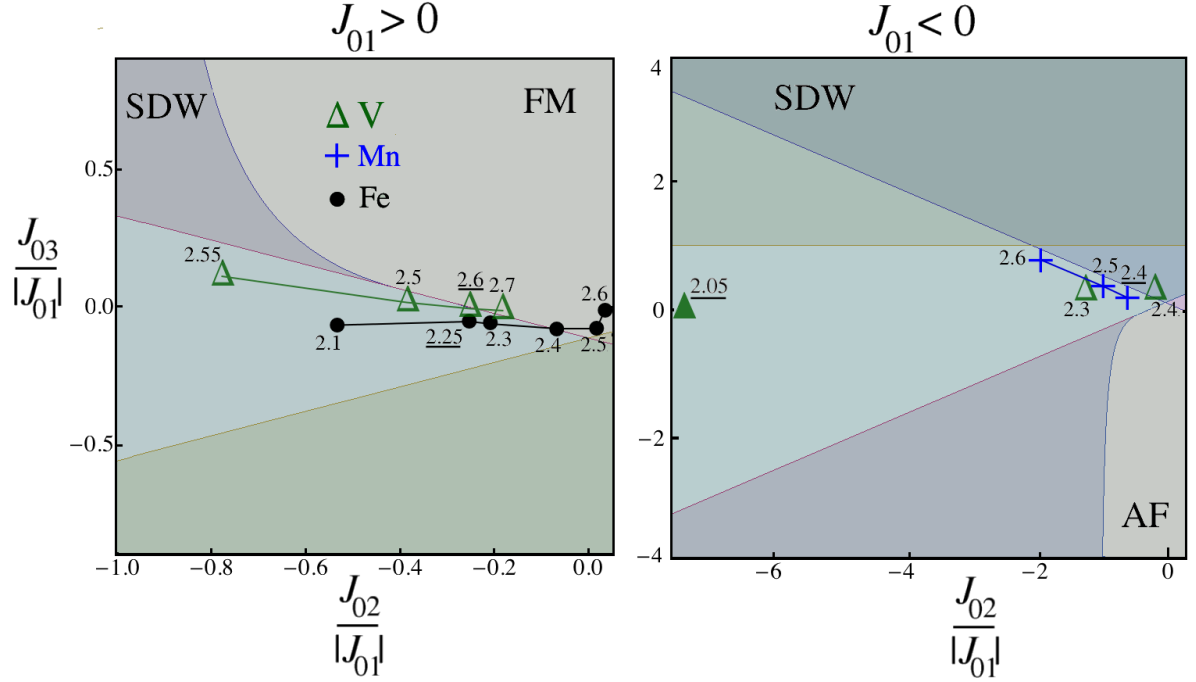


**Figure 4.14:** Magnetic phase diagram of the classical Heisenberg model having first, second, and third NN interactions  $J_{01}$ ,  $J_{02}$  and  $J_{03}$ . The left figure corresponding to  $J_{01} > 0$  (FM NN coupling) while the right figure corresponding to  $J_{01} < 0$  (AF NN coupling). The symbols correspond to the effective exchange parameter  $J_{0\delta}$ , which are derived from the *ab initio* magnon dispersion relations of V, Mn and Fe chains. The corresponding lattice parameter  $a$  is given in Å. The equilibrium value is underlined.

It is interesting to notice that the SDW states remain the most stable arrangements in Mn chain over a wide range of interatomic distances ( $2.4 \leq a \leq 2.7$  Å). The phase diagram of the classical Heisenberg model based on the first and second NN interactions summarizes the competition between these couplings and the resulting ground-state magnetic orders.

A more detailed description of the classical Heisenberg model is obtained by including the 3rd NN interaction. In this case the different magnetic behavior can also be summarized in a 2D plot. However, one needs to consider the case  $J_{01} > 0$  and  $J_{01} < 0$  separately. The corresponding phase diagram is shown in Fig. 4.14. It consists two parts:  $J_{01} > 0$  (FM NN coupling) and  $J_{01} < 0$  (AF NN coupling). It is particularly interesting to include the  $J_{03}$  interaction coupling in the phase diagram, when  $J_{01}$  decreases and becomes small as compared to  $J_{02}$  as a function of the interatomic distance  $a$ . For example,  $J_{01}$  becomes very small approaching to zero at  $a = 2.05$  and  $a = 2.7$  Å in the case of V and Mn nanowires, respectively. Therefore, one needs to include higher-order interactions terms beyond  $J_{02}$ . For Mn chains, the obtained values of  $J_{01}$ ,  $J_{02}$  and  $J_{03}$

are  $-2.1$ ,  $-23.5$  and  $11.3$ ) meV at  $a = 2.7$  Å, respectively. Thus,  $J_{03}$  has a sizable value and plays an important part for the stability of magnetic state. The *ab initio* calculations yield in most case  $J_{01} < 0$  except in the case of Mn wires, where the first NN interaction favor AF order. In V wires, we have  $J_{01} > 0$  for  $a > 2.4$  Å and  $J_{01} < 0$  for  $a < 2.4$  Å. The stability of spiral SDW structures is not changed by including  $J_{03}$  for all considered V, Mn and Fe nanowires. The classical Heisenberg model provides a better understanding of ground-state structures and of the changes in the magnetic stability with different values of the interatomic distances.

## 4.5 Conclusions

The magnetic order in one-dimensional 3d transition-metal (V, Mn and Fe) nanowires has been investigated in the framework of a generalized-gradient approximation to density-functional theory. The stability of spiral SDWs structures has been analyzed in terms of the frozen-magnon dispersion relation. Our results indicate that V, Mn and Fe nanowires the NC spiral arrangements are stable than the collinear FM and AF orders at the equilibrium lattice parameter. In addition one observes that the stability of spin-spiral structures is further enhanced under compression. A local analysis of the effective exchange interaction  $J_{0\delta}$  between the local moments shows that the stability of the NC SDWs is mainly the result of competing first and second NN interactions. The electronic structures of collinear and noncollinear magnetic states have been analyzed in some detail by comparing the local density of states for various representative values of the SDW vector  $q$ . The depletion of the DOS around the Fermi energy and the additional hybridization between orbitals having opposite spins suggested the main cause for the stability of NC magnetic configurations.

The effective exchange interaction parameters  $J_{0\delta}$ , which are derived from the *ab initio* results by using the classical Heisenberg model, provide a local interpretation of the magnetic order and its stability. A broader perspective to the problem of the stability of collinear and NC magnetic orders in 1D systems is provided by the magnetic phase diagrams of the classical Heisenberg model in the framework of the calculated *ab initio* magnon dispersion relations become simple specific examples.

An important extension extensions of this work is the study of wires deposited in experimentally relevant insulating and metallic surfaces. Comparison with the results reported in chapter should allow to assess the effects of wire-substrate hybridizations on the wire geometry and electronic structure. Calculations of local electronic and magnetic properties such as spin-density profiles relevant for spin-polarized STM experiments would provide additional possibilities of contrasting theory and experiment.

In addition, materials which are non-magnetic as 3D bulk solids (e.g., Rh, Pd or Pt) are likely to be magnetic in a low coordinated 1D geometry. These heavier elements offer new possibilities of showing remarkable magnetic behaviors due to the importance of spin-orbit interactions. Furthermore, the effective exchange interaction parameters derived from the present constrained DFT combined with electronic calculations of the MAE could be used to explore the static and dynamic properties of domain walls in TM nanowires, a subject of crucial importance for future technological applications.

In the present work, spin-orbit (SO) interactions are not taken into account, since their influence on the  $q$ -dependence of the total energy  $E$  is not expected to be important for  $3d$  elements [40–43]. As we see in Fig. 4.10 (a), the typical energy differences between FM and AF orders in Fe chain at the equilibrium distance  $a = 2.25 \text{ \AA}$  is of the order of  $\Delta E^{\text{SR}} = E(\pi/a) - E(0) = 321.6 \text{ meV/atom}$ , while including SO interactions and applying the force theorem we obtain  $\Delta E^{\text{SO}} = 322.7 \text{ meV/atom}$ . The SO contribution to the total energy  $E$  is actually small, of the order of  $1 \text{ meV/atom}$  [e.g.,  $E(0)^{\text{SR}} - E(0)^{\text{SO}} = 1.1 \text{ meV/atom}$ ] but the resulting  $q$ -dependence remains very weak, at least in this case. Similar results are obtained for spirals with intermediate values of  $q$ . Moreover, the wires to be consider in the following have all inversion symmetry. This implies that the Dzyaloshinskii-Moriya interaction, [37] which could stabilize noncollinear order as shown for some ultrathin films, [39, 98] strictly vanishes in our case.



# Noncollinear magnetic orders and spin-wave spectra of Fe chains

The following chapter is dedicated to investigate the ground-state magnetic properties of free-standing Fe wires having zig-zag and rectangular geometries in the framework of density-functional theory. The stability of various wires geometries and types of magnetic orders is analyzed as a function of the spin-density-wave (SDW) number  $q$ . In particular we consider all possible magnetic configurations such as ferromagnetic (FM), antiferromagnetic (AF) and noncollinear (NC). The frozen-magnon dispersion relations  $\Delta E(q)$ , local magnetic moments  $\mu_i$ , spin-polarized electronic densities of states  $\rho_{i\sigma}^d(\varepsilon)$  and effective exchange couplings  $J_{ij}$  are calculated at equilibrium interatomic bond lengths  $d$ . The electronic structures of collinear and NC states are analyzed by comparing the density of states  $\rho_{i\sigma}^d(\varepsilon)$  for different representative values of  $q$ . Effective exchange-interaction parameters  $J_{ij}$  between the local moments  $\mu_i$  and  $\mu_j$  are derived by fitting the *ab initio* magnon dispersion relation  $\Delta E(q)$  to a classical Heisenberg model. Comparing the *ab initio* results within a model phase diagram provides new insights on the magnetic order of Fe wires from a local perspective.

## 5.1 Introduction

The understanding of the fundamental properties of Fe bulk and its nanostructures have not been completely understood upto now. Numerous experimental and theoretical investigations have been carried out in order to understand the magnetic properties of Fe and its alloys. For example,  $\gamma$  phase of Fe is one of the most complicated example with highly frustrated structures [22–24,96]. The complex interplay between the struc-

tural and the magnetic degrees of freedom leads to many interesting properties such as noncollinear configurations and spiral SDWs. Furthermore, the magnetic ground-states of  $\gamma$ -Fe crucially depends on the values of lattice parameters. This sensitivity to volume dependence has been discussed in detail by many groups in the context of a so-called moment-volume instability [26,99].

Similarly, in low-dimensional Fe nanostructures e.g., 1D monoatomic chains the magnetic properties are particularly interesting. Much effort has been spent in order to understand the effect of the reduced dimensionality on the magnetic ground-state properties [41–43,100]. Magnetic monoatomic chains especially in TM systems are a subject of a very intensive theoretical and experimental research activity that is driven by equally important fundamental and technological interests [1,2,13,91,101]. Experimentally, the controlled formation of 1D or quasi-1D magnetic materials sets the first challenge. Significant progress has been made in the variety of preparation techniques, for example, techniques have been developed to this aim, for example, diffusion controlled aggregation along the on anisotropic surfaces [2], self-assembly [1], spin-polarized STM manipulation [102], or controlled mechanical breaking of junctions [95]. Alongside these experimental developments, a significant number of theoretical studies have been performed on the magnetic properties of 1D systems [4,36,40,41,43,44,86,97,100,103]. For instance, Tung *et al.* explored the electronic structures and magnetic properties of one-dimensional  $3d$  TM chains [42]. They found that the ground-state magnetic order of Fe chains is noncollinear as a result of competing interactions.

The remainder of the chapter is organized as follows. In section 5.2 the simulation model of SDWs in zigzag chains and ladders are presented along with the details of the theoretical background and computational procedure. The results of our calculation for the stability of NC magnetism in various geometries of Fe chains are reported in sections 5.2.1 and 5.2.2. Here, we focus on the structural, electronic and magnetic properties of considered Fe wires. The magnon dispersion relations are discussed for representative interatomic distances including the equilibrium configuration. In section 5.2.4, the effective exchange interactions between local magnetic moments are derived, which allow a detailed interpretation of the spin-spiral instabilities from a local perspective. we also analyze the stability of SDWs in terms of a simple classical Heisenberg model, which takes into account the effective exchange interactions  $J_{ij}$  between various NNs. Finally, we conclude in section 5.3 with a summary of our main results and an outlook on challenging future developments.



## 5.2 Models of SDWs in chains and ladders

In order to investigate the formation of SDWs in 1D zigzag chains and ladders, we consider a supercell approach and determine the magnetic properties of free-standing Fe wires having different geometrical structures as a function of the wave number  $q$ . The spiral spin arrangements are modeled by fixing the direction of the local magnetic moment  $\vec{\mu}_i$  at each atom  $i$  in the wire. In monoatomic linear chains [Fig. 6.1(a)] the SDW consists of  $N$  atoms in the supercell (typically  $N \leq 12$ ) separated by the lattice parameter  $a$ , which in this case coincides with the NN distance  $d$ . For more complex structures, such ZZ chains or RLs,  $a$  and  $d$  are different, as illustrated in Fig. 6.1. The dimensions of the supercell in the directions perpendicular to the wire must be chosen large enough to ensure that there is no significant interaction between the periodic replicas. In practice, 16 Å is found to fulfill this condition. In order to calculate the frozen-magnon dispersion relation we determine the total energy  $E(\vec{q})$  by considering SDW vectors  $\vec{q}$  along the chain direction. The corresponding wave numbers  $q = |\vec{q}|$  are compatible with the supercell periodicity:  $q = 2\pi n/(Na)$  with  $0 \leq n < N$  and  $n$  integer. Thus, the collinear FM and AF states ( $q = 0$  and for  $N$  even  $q = \pi/a$ ) are included as particular cases when  $q$  is varied [see Fig. 6.1]. Four different types of wires are considered: linear chains (LCs), ZZ chains with periodic noncollinear (PNC) order, ZZ chains with alternating collinear and noncollinear alignment of neighboring local moments, and RLs. Fig. 6.1 illustrates these wire geometries taking spiral SDWs with wave vector  $\vec{q} = (0, 0, \pi/4a)$  as representative examples.

The first principles calculations reported in the present work have been performed in the framework of Hohenberg-Kohn-Sham's DFT [55], as implemented in the Vienna *ab-initio* simulation package (VASP) [78]. The XC energy-functional is treated by using Perdew and Wang's spin-polarized GGA [71]. The spin-polarized KS equations are solved in an augmented plane-wave basis set, taking into account the interaction between valence electrons and ionic cores by means of the PAW method [71]. This is an efficient frozen-core all-electron approach, which takes into account the proper nodes of the valence KS orbitals in the core region and the resulting effects on the electronic structure and magnetic properties. For the present calculations the 4s, 4p and 3d orbitals are treated as valence electrons. The KS wave functions are expanded in the interstitial region in a plane wave basis set with a cut-off energy  $E_{max} = 500$  eV. The integrations in the Brillouin zone are performed by using the Monkhorst-Pack scheme [79] with a  $k$  mesh of  $1 \times 1 \times 40$  points. Test calculations with higher cut-off energies and additional  $k$  points have shown that these values are a good compromise between accuracy and computational effort. The accuracy of our calculations, for example in the total energy, is estimated to be 1 meV/atom or better. For metallic-like systems, one often finds very rapid variations of the states close to the Fermi

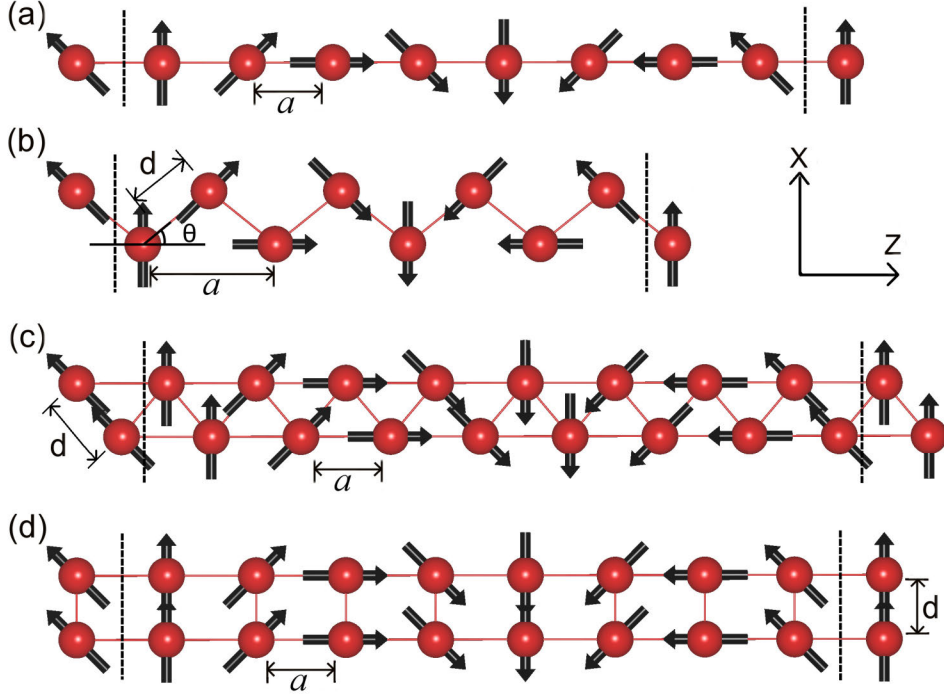


**Figure 5.1:** Illustration of the wire structures and magnetic orders corresponding to a spin-wave vector  $\vec{q} = (0, 0, \pi/4a)$ : (a) linear chain (LC), (b) zig-zag chain with periodic noncollinear (PNC) order, (c) zig-zag chain with alternating noncollinear (ANC) order, and (d) rectangular-ladder (RL) with parallel moments in the direction perpendicular to the chain. In (a) and (b) the simplest PNC spin-density wave having  $\hat{\mu}_i \cdot \hat{\mu}_{i+1} = \cos(qa)$  is shown, while (c) and (d) correspond to the so called ANC order having  $\hat{\mu}_i \cdot \hat{\mu}_{i+1} = \cos(qa)$  for  $i$  even and  $\hat{\mu}_i \cdot \hat{\mu}_{i+1} = 1$  for  $i$  odd. The lattice parameter  $a$ , nearest-neighbor distance  $d$ , and bond angle  $\theta$  are indicated.

level  $\varepsilon_F$  that may cause a poor convergence of the relevant physical quantities such as the total energy or the local magnetic moments. Therefore, a smearing of the KS levels is introduced in order to improve the numerical stability. Here we use a Gaussian smearing with a width  $\sigma = 0.01$  eV, a value that ensures that the smearing contribution to the total energy is less than  $10^{-4}$  eV/atom. The local magnetic moment  $\vec{\mu}_i$  at atom  $i$  is calculated by integrating the magnetization density  $\vec{m}(\vec{r})$  inside the corresponding atomic WS sphere. In the case of Fe the radius of WS sphere is  $R_{WS} = 1.302$  Å.

### 5.2.1 Structural properties

In order to investigate the interplay between the magnetic behavior and geometrical structure of Fe wires, we determine the binding energy  $E_B = E - E_{at}$  by referring the

total electronic energy  $E$  of the wires to the sum  $E_{at}$  of the energies of the constituting isolated atoms. The different geometries and magnetic orders are illustrated in Fig. 6.1. This includes LCs, ZZ chains and RLs having collinear FM and AF orders, as well as PNC and ANC spin arrangements. In each case a bond-length relaxation is performed in order to determine the equilibrium interatomic distance within the 1D constraint. For the sake of comparison, the equilibrium NN distance  $d$  of a monoatomic linear chain has been calculated by assuming a FM state. In agreement with previous studies [86, 100], we obtain  $d = 2.25 \text{ \AA}$ . The corresponding local magnetic moment  $\mu = 3.1\mu_B$  calculated within the Fe WS spheres is largely enhanced with respect to the bulk value  $\mu_b \simeq 2.18\mu_B$ . This is a consequence of the extremely low local coordination number of the linear geometry and the resulting important  $d$ -band narrowing. The ZZ chains are obtained from the relaxation of the linear chain at short lattice parameters, when the atoms are allowed to move in a direction perpendicular to the chain, keeping them within a given transversal plane, in our case the  $xz$ -plane [see Fig. 6.1 (b)]. According to our calculations, the optimal ferromagnetic ZZ structure of Fe wires has a NN bond length  $d = 2.23 \text{ \AA}$ , a lattice parameter or second NN distance  $a = 2.52 \text{ \AA}$ , and a bond angle is  $\theta = 69^\circ$ . These results are similar to those reported in previous works [86, 97, 100]. The local magnetic moments of the ZZ geometry are about 6% smaller than in the LC, which is consistent with the increasing local coordination number. For RLs the relaxed lattice parameters obtained assuming a FM state are  $d = 2.15 \text{ \AA}$  and  $a = 2.4 \text{ \AA}$ . The corresponding local magnetic moment is  $\mu = 2.9\mu_B$ . It should be, however, noted that the FM order is not stable in Fe RLs close to equilibrium.

In Fig. 5.2  $E_B$  is shown as a function of the lattice parameter  $a$ , for various wire geometries and magnetic orders with representative values of the wave number  $q$ . The results provide a first insight on the interplay between structural stability and magnetic order. In the case of ZZ chains we observe that the FM order is always the most stable configuration. Only for very short lattice parameters  $a < 2.15 \text{ \AA}$  we find that some NC arrangements start to be slightly more stable [see Fig. 5.2 (a)]. Moreover, the ANC order, in which one every two pairs of NN spins are parallel, is always found to be more stable than the standard PNC state, in which the angle between all NN spins is finite. This shows that the FM coupling is favored both at short and long length scales. Notice that the relaxed lattice parameters corresponding to the NC states ( $q \neq 0$ ) are similar, though slightly smaller than in the FM state.

In contrast to the ZZ geometry, ferromagnetism is unstable in Fe RLs, since  $E_B$  decreases for non-vanishing values of  $q$ . This holds not only for  $a$  close to the relaxed lattice parameter of the FM state, but even more strongly for shorter bond lengths [see Fig. 5.2 (b)]. As a result, much shorter equilibrium lattice parameters and stronger binding are obtained in the NC state. For instance, the relaxed lattice parameter for  $q = \pi/2a$  is  $a = 2.3 \text{ \AA}$ , which is close to the optimal structural and magnetic

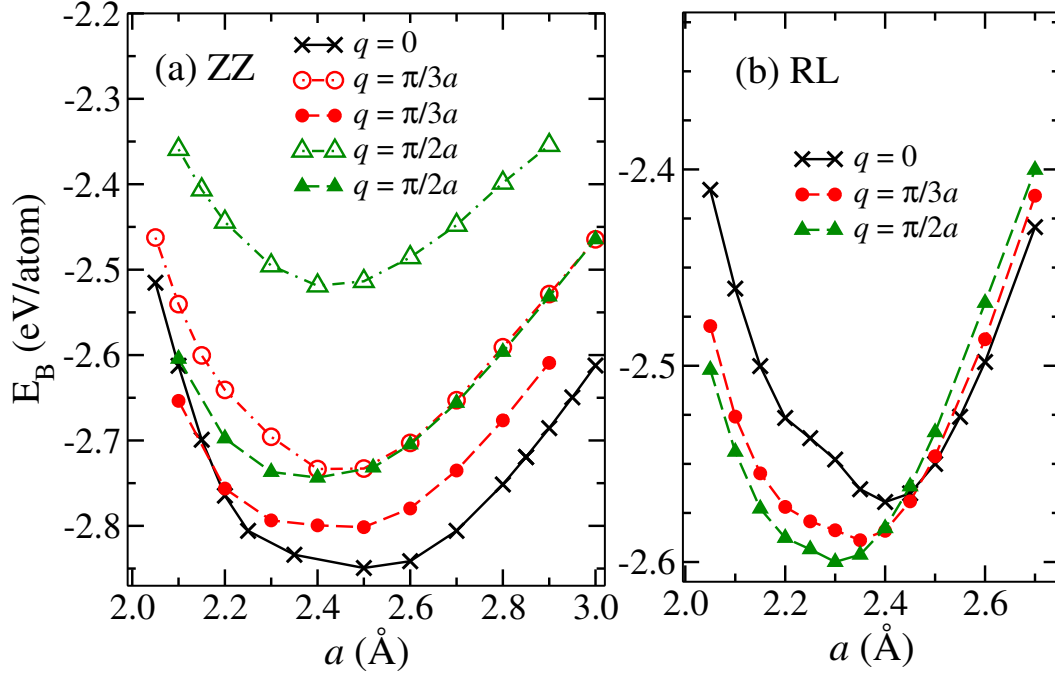


**Figure 5.2:** (a) Binding energy of zig-zag (ZZ) Fe chains as a function of the lattice parameter  $a$  [see Fig. 6.1 (b)]. Different SDW vectors  $q$  are considered as indicated in the inset. Filled symbols correspond to the periodic noncollinear order (PNC) order [Fig. 6.1 (b)], while open symbols correspond to the alternating noncollinear (ANC) order [Fig. 6.1 (c)]. (b) Binding energy of Fe rectangular-ladders (RLs) as a function of the lattice parameter  $a$  [see Fig. 6.1 (d)].

arrangement. This is approximately 56 meV/atom more stable than the lowest FM configuration. The same behavior holds for other SDW lengths. For example, the binding-energy gain for  $q = \pi/3a$  is about 47 meV/atom. Only for long stretched RLs having  $a > 2.5$  Å the trend is reversed and the FM order becomes the most stable configuration [see Fig. 5.2 (b)]. A more detailed discussion of the magnetic properties and underlying electronic structure of Fe wires is found in the following.

### 5.2.2 Spin-density wave spectra

The total electronic energy  $E(q)$  as a function of the wave number  $q$  allows one to identify the ground-state magnetic order as a function of wire geometry and lattice parameter, within the consider spin-spiral configurations. The resulting frozen-magnon dispersion relation  $\Delta E(q) = E(q) - E(0)$  provides detailed information on the stability of the ground-state magnetic configuration with respect to spin-wave excitations. Moreover, quantifying the changes in the local magnetic moments  $\mu(q)$  for different

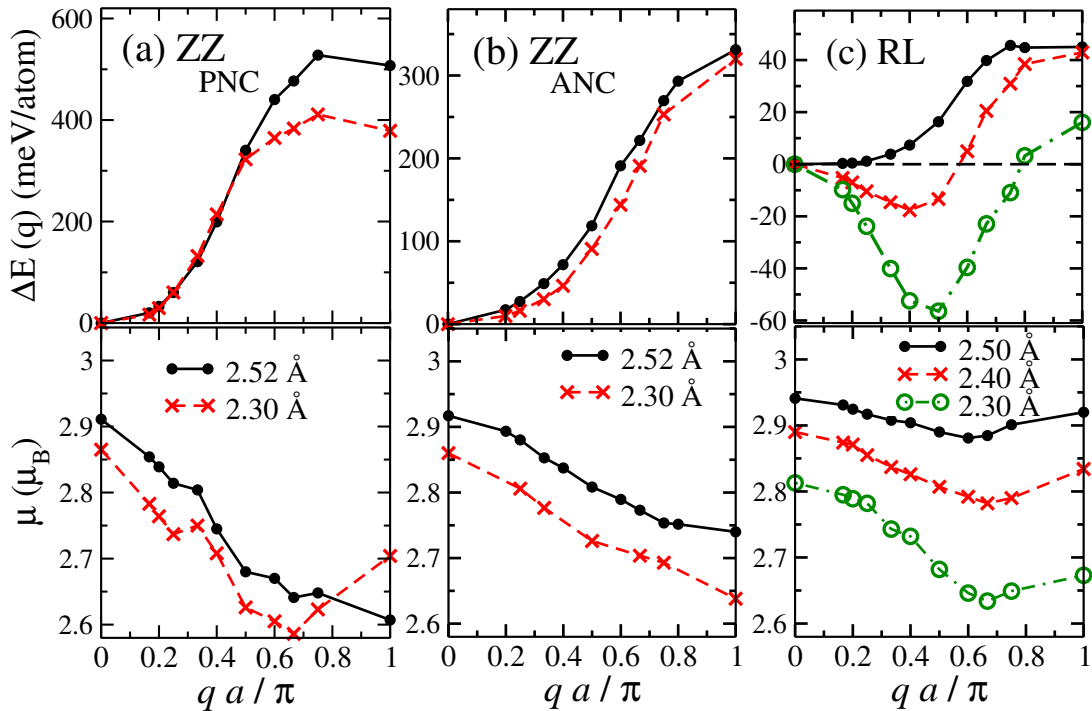


**Figure 5.3:** Frozen-magnon dispersion relation  $\Delta E(q) = E(q) - E(0)$  (upper panels) and local magnetic moments  $\mu$  within the Wigner-Seitz (WS) cells (lower panels) of Fe wires as a function of the SDW vector  $q$ : (a) zig-zag (ZZ) chain with periodic noncollinear order (PNC), (b) ZZ chain with alternating noncollinear magnetic (ANC) order, and (c) rectangular-ladders (RLs) with parallel moments in the direction perpendicular to the wire [see Fig. 6.1]. Results are given for representative values of the lattice parameter  $a$  as indicated.

$q$ , i.e., for different magnetic orders, gives a measure of the robustness the local magnetic degrees of freedom, a requisite for the analysis and interpretation of the magnetic interactions from a local perspective.

In Fig. 6.6 results are given for  $\Delta E(q)$  and  $\mu(q)$  of Fe stripes having ZZ and RL geometries at representative lattice parameters  $a$ . In ZZ wires, not only the FM order yields the lowest-energy configuration but, in addition, the spectrum of spin-wave excitations is particularly stiff.  $\Delta E(q)$  increases monotonously with  $q$ , except close to the zone boundary of PNC waves ( $qa/\pi \geq 0.8$ ) where it goes over a maximum and slightly decreases [see Fig. 6.6 (a)]. The ANC waves involve significantly lower excitation energies than the PNC ones, typically  $\Delta E(q)|_{\text{ANC}} \simeq \Delta E(q)|_{\text{PNC}}/2$ . This indicates that ferromagnetic order is also very stable at short distances, since one every two FM couplings between NNs is preserved in the ANC case [see Fig. 6.1]. These trends hold for all considered lattice parameters  $a$ , including the equilibrium value  $a = 2.52 \text{ \AA}$ , except for strongly compressed ZZ wires ( $a \leq 2.2 \text{ \AA}$ ).

The contrast between triangular and rectangular stripes is most remarkable. As shown in Fig. 6.6 (c), the magnon dispersion relation of Fe RLs having the equilibrium distance  $a = 2.4 \text{ \AA}$  shows a local minimum at  $q_{min} \simeq 0.4\pi/a$ , which energy lies 18 meV/atom below the FM state and 62 meV/atom below the AF state. Moreover, these spin-spiral states are further stabilized in compressed RLs. For example, for  $a = 2.3 \text{ \AA}$ , the SDWs having a periodicity of about four lattice parameters ( $q \simeq \pi/2a$ ) are 57 meV/atom, respectively 73 meV/atom, more stable than the collinear FM and AF arrangements. Only for large large interatomic distances along the wire ( $a \geq 2.5 \text{ \AA}$ ) we find a FM ground state. This behavior is qualitatively similar to the one observed in 3d TM monoatomic linear chains [41, 86]. From this perspective our results confirm that spiral-SDW ground states are neither a specificity of 1D systems [27] nor a simple consequence of reduced coordination number. The geometry of the wire in the transversal direction plays a central non-trivial role. In the following sections we aim to clarify the microscopic origin of this remarkable effect by analyzing the underlying electronic structure for different values of  $q$  and by deriving effective exchange interactions between the local magnetic moments at different lattice positions.

In Fig. 6.6 the modulus of the local magnetic moments  $\mu(q) = |\langle \vec{m} \rangle_{WS}|$  inside the atomic WS spheres is also shown as a function of  $q$ . For all considered lattice parameters one observes that the local moments are remarkably robust, irrespectively of the magnetic order and geometry of the wires. The quantitative changes amount to less than 10%. This implies that the local magnetic degrees of freedom always preserve their identity. An interpretation of the magnon dispersion curves in terms of effective interactions between the local moments in real space is therefore justified. In the FM ZZ wires,  $\mu$  decreases as the spiral order develops with increasing  $q$ , reaching its minimum value for the AF state or short before it [see the lower panels of Figs. 6.6 (a) and (b)]. The largest changes in  $\mu$  are found for the ZZ geometry at the equilibrium  $a$ , where it drops from  $\mu(0) = 2.93 \mu_B$  to  $\mu(\pi/a) = 2.60 \mu_B$  or  $\mu(\pi/a) = 2.75 \mu_B$  for the PNC and ANC waves respectively. This is probably a consequence of the larger local coordination number and stronger  $d$ -electron hybridizations in the ZZ geometry. In RLs a weak non-monotonous dependence of  $\mu$  on  $q$  is found, even for large lattice parameters having a FM ground state. The typical changes are about 2–6%. For example,  $\mu$  drops from  $\mu_i(0) = 2.89 \mu_B$  to  $\mu_i(\pi/a) = 2.83 \mu_B$  for the equilibrium  $a = 2.4 \text{ \AA}$ . Notice that the positions of the minima in  $E(q)$  and  $\mu(q)$  do not coincide in general [see Fig. 6.6 (c)].

### 5.2.3 Local electronic structure

In Figs. 5.6 the calculated spin-polarized local  $d$ -electron DOS of Fe stripes are given for representative wave numbers  $q$ . In each case the 3d-electron DOS  $\rho^d(\vec{r}, \sigma, \varepsilon)$  is projected on the position  $\vec{r}$  and on the spin components up and down ( $\sigma = \uparrow, \downarrow$ ) taking

the direction of the local magnetic moment  $\vec{\mu}_i$  at some atom  $i$  as the spin-quantization axis. The up and down spin components should actually be understood as majority- and minority-spin projections. Subsequently, the DOS is integrated within the WS sphere of atom  $i$  in order to obtain the spin-polarized local DOS  $\rho_{i\sigma}^d(\varepsilon)$ . Since the magnetic order of these wires is roto-translational invariant for all  $q$ , the thus obtained local DOS are strictly the same at all atoms. A translation of the orbital coordinates by a distance  $a$  along the wire, followed by a rotation of the spin coordinates by an angle  $\theta = qa$  around the axis of the wire, leaves the electronic states unchanged. Therefore, the result for  $\rho_{i\sigma}^d(\varepsilon)$  can be compared for different  $q$  and lattice structures.

The changes in the DOS as  $q$  increases reveal a most interesting crossover between the quite distinct FM and AF electronic structures. For  $q = 0$  we observe the characteristic FM exchange splitting between up and down DOS, each of which has an important band width, which is larger than the exchange splitting. Minority and majority DOS overlap, but there is no hybridization between them. The up DOS vanishes at high energies, where the down DOS has the largest unoccupied contributions, and the down DOS vanishes at the bottom of the band, where the important peaks in the up DOS are present. As  $q$  increases a true hybridization between majority and minority states takes place. This is clearly reflected by the increased participation of down states at low energies, where the up states are dominant, and of the up states at high energies, where the down states have their most remarkable features. In addition, with increasing  $q$ , the electronic states are depleted from the middle of the band, near half  $d$ -band filling. Two distinct lower and higher energy sub-bands start to develop. At the same time, the width of the dominant parts of the majority and minority DOS decrease appreciably as we go from the FM to the AF configuration. This band narrowing is compensated by the above mentioned increased hybridization between up and down states, so that the variance (or second moment) of the majority and minority DOS depend very weakly on  $q$ . These features are common to both ZZ and rectangular stripes [see Figs. 5.4, 5.5, and 5.6].

Contrasting the different wire geometries provides a qualitative insight on the microscopic origin of the relative stability of collinear and noncollinear magnetic orders. The DOS around the Fermi energy  $\varepsilon_F$  is particularly low in the FM configuration of ZZ chains [see Fig. 5.4 (a)]. Occupied majority states are well separated from the unoccupied minority ones, which anticipates a strong stability of the  $q = 0$  state. As  $q$  increases spectral weight is transferred to Fermi energy from lower and higher energies. For the PNC order a strong peak is located precisely at  $\varepsilon_F$  for  $q = \pi/2a$  and  $q = 3\pi/4a$ . In the AF state a new though less important reduction of the DOS at the Fermi energy is found. The strong peak becomes essentially unoccupied and further spectral weight is shifted to stronger binding [compare Figs. 5.4 (d) and (e)]. This explains, from an electronic perspective, the strong increase of the magnon dispersion relation  $\Delta E(q)$

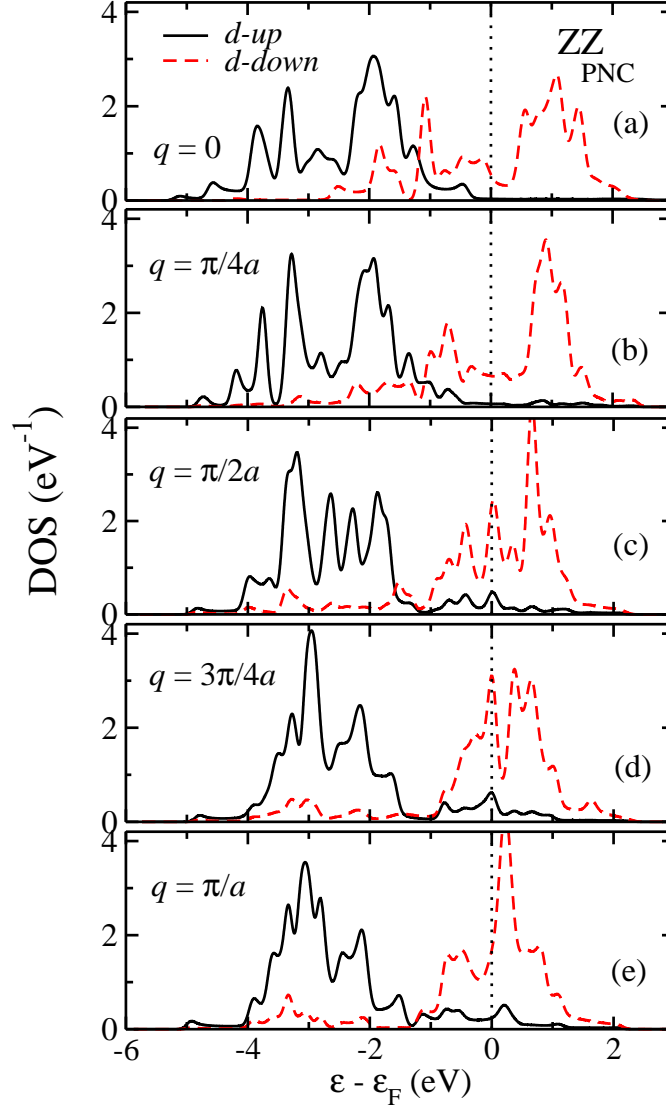


**Figure 5.4:** Local  $d$ -electron density of states (DOS)  $\rho_{i\sigma}^d(\varepsilon)$  of free-standing zig-zag (ZZ) Fe chains with periodic noncollinear (PNC) order at the equilibrium lattice parameter  $a = 2.52 \text{ \AA}$  for representative SDW numbers  $q$ . Results are given for the majority-spin (full lines) and minority-spin (dashed) components along the direction of a local magnetic moment  $\vec{\mu}_i$ . The Fermi energy  $\varepsilon_F$  is indicated by the vertical dashed lines.

for small values of  $q$ , as well as the flattening or slight decrease of  $\Delta E(q)$  at the zone boundary [see Fig. 6.6 (a)]. In the ANC case an increase of the DOS close to  $\varepsilon_F$  is also observed with increasing  $q$ . This explains qualitatively the increase of  $\Delta E(q)$  with increasing  $q$ , which implies that FM order is favored. However, the spectral-weight transfer is more progressive and, above all, much less important than in PNC waves



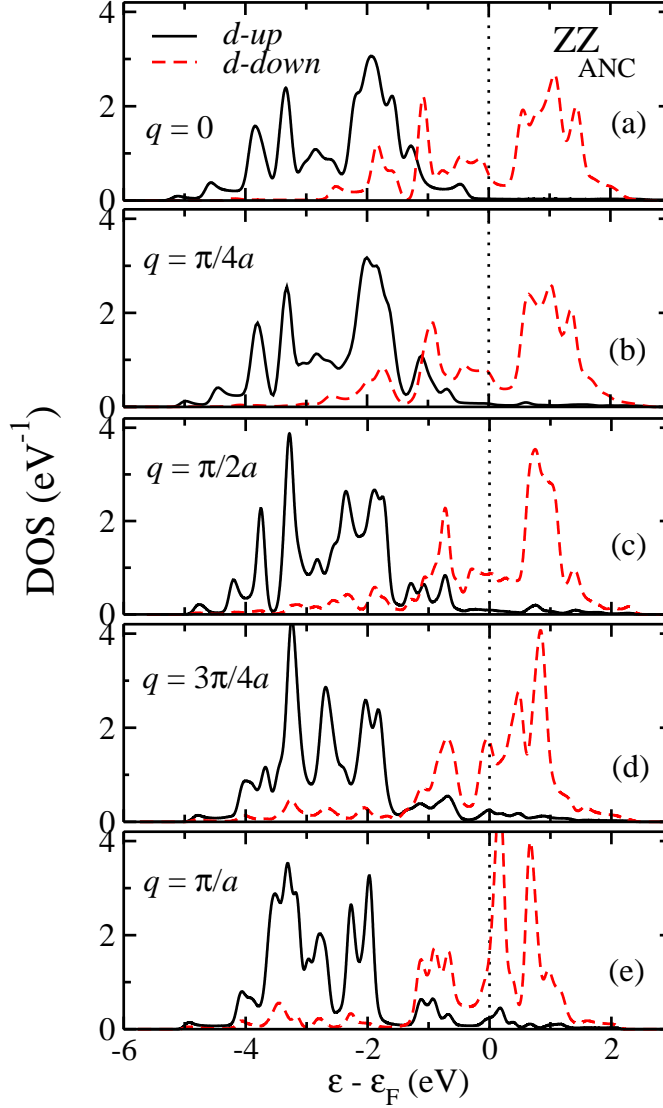


**Figure 5.5:** Local  $d$ -electron density of states (DOS)  $\rho_{i\sigma}^d(\varepsilon)$  of free-standing zig-zag (ZZ) Fe chains with alternative noncollinear (ANC) order at the equilibrium lattice parameter  $a = 2.52 \text{ \AA}$  for representative SDW numbers  $q$ . Results are given for the majority-spin (full lines) and minority-spin (dashed) components along the direction of a local magnetic moment  $\vec{\mu}_i$ . The Fermi energy  $\varepsilon_F$  is indicated by the vertical dashed lines.

[see Fig. 5.5]. This is consistent with the weaker and monotonous increase of  $\Delta E(q)$  shown in Fig. 6.6 (b).

In RLs the electronic structure is quite different. Here we find a high DOS at  $\varepsilon_F$  in the FM state, which tends to be reduced and broadened for  $q = \pi/2a$  [compare Figs 5.6 (a)–(c)]. Consequently, one expects that NC configurations with finite values of  $q$  should be more favorable. Finally, in the AF state of RLs the width of the minority

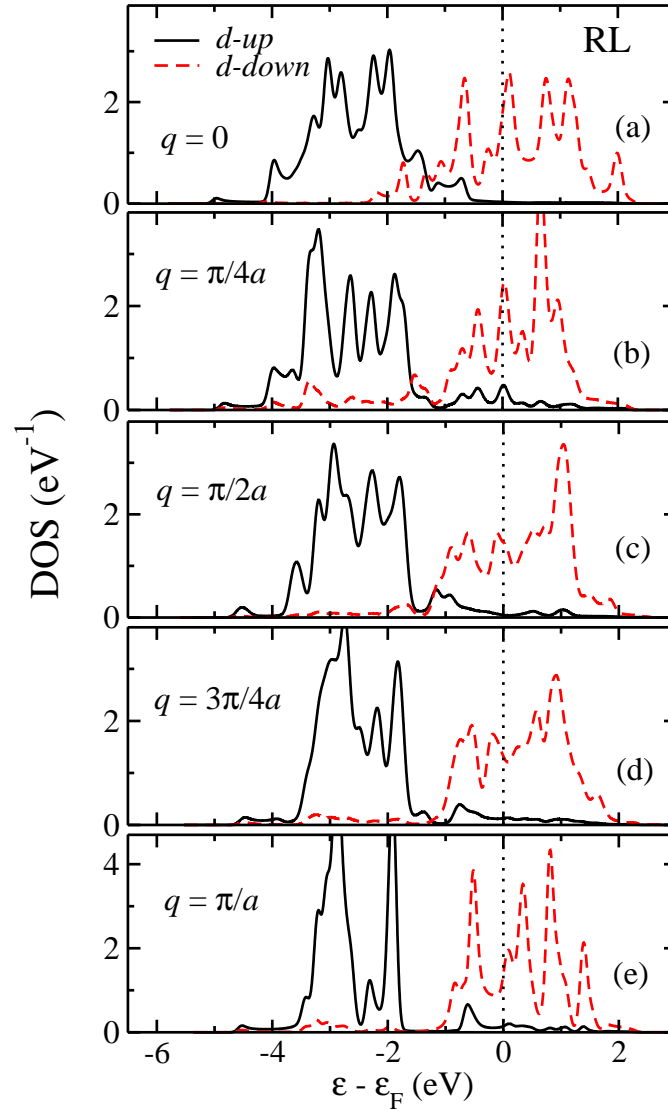


**Figure 5.6:** Local  $d$ -electron density of states (DOS)  $\rho_{i\sigma}^d(\varepsilon)$  of free-standing Fe rectangular ladders (RLs) at the equilibrium lattice parameter  $a = 2.4 \text{ \AA}$  for representative SDW numbers  $q$ . Results are given for the majority-spin (full lines) and minority-spin (dashed) components along the direction of a local magnetic moment  $\vec{\mu}_i$ . The Fermi energy  $\varepsilon_F$  is indicated by the vertical dashed lines.

band becomes clearly narrower [see Fig. 5.6 (e)]. Consequently, occupied minority states are shifted to higher energies, closer to  $\varepsilon_F$ . This implies an increase of the KS electronic energy, in agreement with the increase in  $\Delta E(q)$  shown in Fig. 6.6 (c) for large  $q$ . In conclusion, the analysis of the DOS as a function of wire geometry and wave number allows us to establish correlations between the local electronic structure and the magnon dispersion relations, thus providing a complementary physical understanding of the latter.

Before closing this discussion it is useful to comment on the interpretation of the reported spin-polarized local DOS from the point of view of real space, in relation to the hopping or hybridization of electrons between NN atoms. We adopt here for simplicity the tight-binding or linear-combination-of-atomic-orbitals perspective, although an analogous argumentation holds in terms of the KS potential  $v_s = v_{ext} + v_H + v_{xc}$ . In a FM state the majority-spin atomic energy levels  $\varepsilon_{\alpha\uparrow}$  on the one side, and the minority-spin energy levels  $\varepsilon_{\alpha\downarrow}$  on the other side, are the same at all atoms. The broadening of the up and down  $d$  bands can be regarded as the result of interatomic hoppings or hybridizations of electrons between orbitals that have nearly the same energy and the same spin projection. We put aside here for simplicity the dependence of the energy levels on  $\alpha$ . Since the magnetic order is collinear and the spin quantization directions at all atoms coincide, the electrons preserve their spin direction upon interatomic hopping. In an AF state the situation is different but still quite transparent. Majority and minority spin directions are inverted between NNs (or between different sub-lattices in general). Therefore, the lower lying majority orbitals hybridize with higher-lying minority orbitals at the NNs. This explains the band narrowing, as compared to FM states, the shift of the majority states to lower energies, and the shift of the minority states to higher energies. In the AF solution ( $q = \pi/a$ ) the electronic hoppings between NNs occur with certainty from the majority up to the minority levels, and vice versa. This follows from the convention for spin quantization adopted above, since the electrons preserve their spin direction upon hopping. For  $0 < q < \pi/a$  the situation is less intuitive. In this case, even the spin conserving potentials  $v_{ext}$  and  $v_H$  yield electronic hoppings between both spin directions. For instance for  $q = \pi/2a$ , a spin up electron hops with equal amplitude to the majority and minority levels of its NNs. The densities of states shown in Figs. 5.4–5.6 are indeed the same on all atoms, but they refer to different directions in spinor space. One should be therefore careful when constructing a real space picture of the electronic structure of spiral states on the basis of the reported local DOS.

### 5.2.4 Effective magnetic interactions

The ground-state magnetic order and magnon dispersion relation of Fe wires can be analyzed from a local perspective in terms of the phenomenological classical Heisenberg model. The NN interactions *alone* can only yield FM or AF dispersion relations depending on their sign. Therefore, it is necessary to take into account magnetic interactions beyond the immediate local environment in order to describe the observed complex  $q$  dependencies leading to NC magnetic arrangements. In the following we consider up to 6th NN interactions in the Hamiltonian. As we shall see, this ensures an accurate description of all relevant spin excitations. The interaction parameters  $J_{0\delta}$  corresponding to different geometries and lattice parameters are obtained by fitting (3.16) to the *ab initio* results for  $\Delta E(q)$ . This Fourier transformation allows us to quantify the effective interactions between the local magnetic moments  $\vec{\mu}_i$ .

In Fig. 5.7, the fitted and *ab initio* results for  $\Delta E(q)$  are compared for representative interatomic distances  $a$ . The right column illustrates the quality of the fits: the curves refer to the Heisenberg model and the symbols to the *ab initio* calculations. The corresponding effective interaction parameters  $J_{0\delta}$  between the local moments are given in the left column as a function of  $\delta$ . One observes that the Heisenberg model provides a very accurate phenomenological description of the *ab initio* magnon dispersion relations for all considered wire geometries. Interactions beyond 4th NNs are found to be negligible.

In the case of ZZ wires with PNC order, the first NN coupling  $J_{01}$  is the dominant interaction both at equilibrium ( $a = 2.52 \text{ \AA}$ ) and at shorter distances ( $a = 2.3 \text{ \AA}$ ). The values of  $J_{01}$  are about 250 meV/atom larger than all other exchange interactions. Consequently,  $\Delta E(q)$  increases with increasing  $q$  and the FM order dominates over all the other NC states, as shown in Fig. 5.7 (d). For the ANC order,  $J_{01}$  is also the most important magnetic coupling in the Hamiltonian. However, in this case  $J_{02} < 0$ , which implies that AF interactions start to become important. Still,  $|J_{02}|$  is small in comparison to  $J_{01}$ . Thus, the FM state remains the most stable magnetic arrangement.

In contrast, in RLs the AF second NN coupling  $J_{02}$  gains a considerable importance. For distances close to equilibrium they are comparable to the first NN ferromagnetic coupling  $J_{01}$ , and for  $a = 2.3 \text{ \AA}$  we find even  $|J_{02}| > J_{01}$ . The competition between FM  $J_{01}$  and AF  $J_{02}$ , and the resulting magnetic frustrations are solved by stabilizing noncollinear magnetic configurations. These strong qualitative differences in the distance dependences of  $J_{0\delta}$  for ZZ chains and RLs explain the contrasting dispersion relations and magnetic orders in these systems. Reduced coordination alone is not a valid argument. The details of the transversal structure of the wires and the local atomic environment matter.

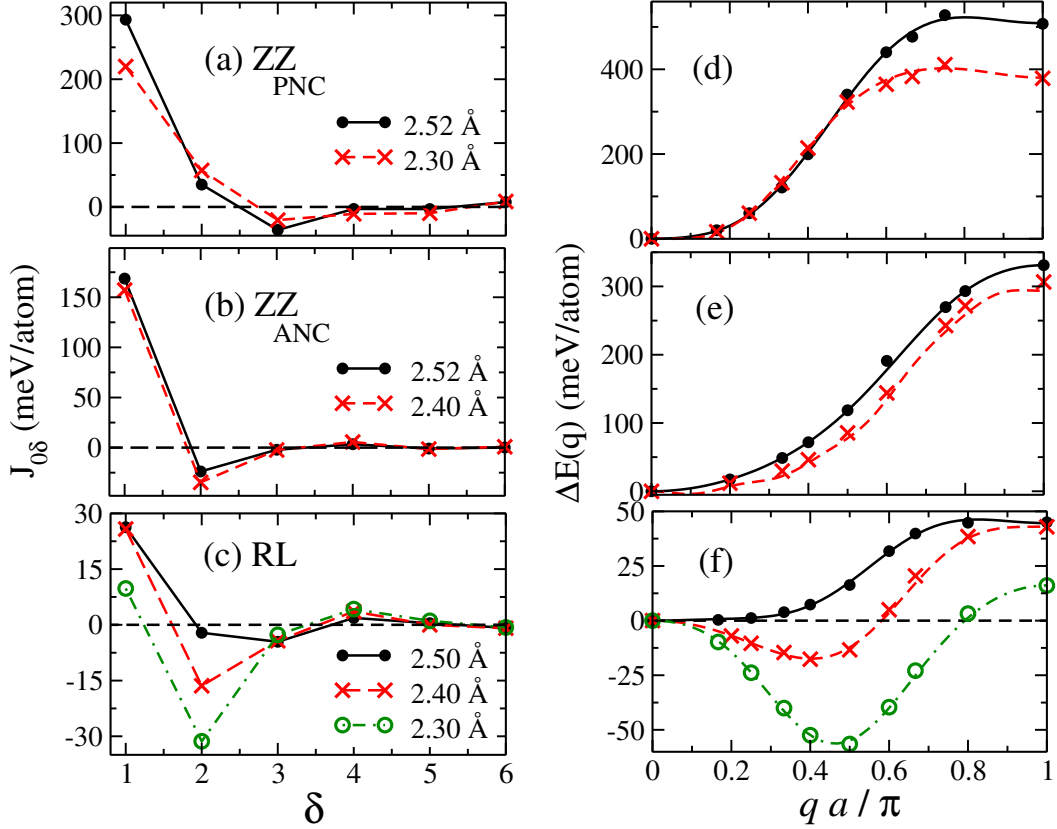


**Figure 5.7:** Effective exchange interactions  $J_{0\delta}$  in Fe wires between a local moment  $\hat{\mu}_0$  and its  $\delta$ th nearest neighbors  $\hat{\mu}_\delta$  as a function of  $\delta$  (left column). The corresponding magnon dispersion relations  $\Delta E(q)$  are shown in the right column, where the curves refer to the classical Heisenberg model fitted to the *ab initio* calculations (symbols). Results are shown for (a) zig-zag (ZZ) chains with periodic noncollinear (PNC) order, (b) ZZ chains with alternating noncollinear (ANC) order, and (c) rectangular ladders (RL) at the indicated lattice parameters  $a$  [see Fig. 6.1].

### Magnetic phase diagram

A more universal analysis of the stability of spiral SDWs in chains and ladders is provided by the ground state phase-diagram of the 2D classical Heisenberg model as a function of the exchange interaction parameters [Eq. (3.16)]. Restricting the range of the interactions to the most important couplings  $J_{01}$  and  $J_{02}$ , one identifies three distinct regimes: the ferromagnetic region for  $J_{01} > 0$  and  $4J_{02} > -J_{01}$ , the antiferromagnetic region for  $J_{01} < 0$  and  $4J_{02} > J_{01}$ , and the noncollinear region for  $4J_{02} < -|J_{01}|$ . In the latter case, SDW solutions having  $0 < q < \pi/a$  are the most stable. In Fig. 5.8, the  $J_{01}$ - $J_{02}$  phase diagram of the classical Heisenberg model is shown. The symbols indicate the interaction parameters derived from the *ab initio* magnon dispersion relations of the different Fe wires at representative lattice parameters  $a$ .

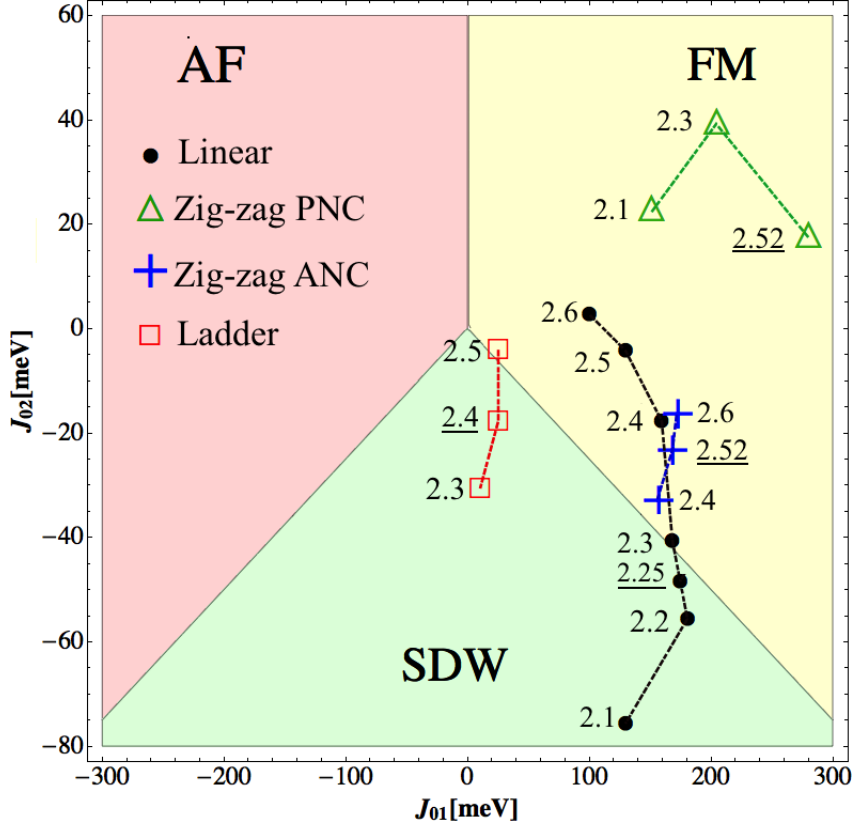


**Figure 5.8:** Magnetic phase diagram of the classical one-dimensional Heisenberg model with first and second NN interactions  $J_{01}$  and  $J_{02}$ . The regions of stable antiferromagnetic (AF), ferromagnetic (FM) and spiral spin-density wave (SDW) orders are shown. The symbols indicate the effective exchange couplings in Fe wires as derived from *ab initio* calculations for linear monoatomic chains (dots), zig-zag chains with PNC (triangles), zig-zag chains with ANC order (cross) and rectangular ladders (squares). The corresponding lattice parameters  $a$  are given in Å, where the equilibrium value is underlined.

For the monoatomic chain, one observes a transition from NC order to FM order as the bond length  $a$  is increased. For  $a \leq 2.3$  Å, and in particular at the equilibrium distance, the linear chain adopts a spiral ground state, whereas for large lattice parameters the FM state is the most stable order. In the ZZ biatomic stripes the PNC and ANC configurations always lie in the FM region for the considered interatomic distances. The ANC states are close to the boundary with the spiral phase, and would certainly finish by changing to a NC configuration if stronger compressions were assumed. In contrast, for PNC waves the points lie well inside the FM phase, confirming the strong stability of the FM order in this case. Finally, RLs at the equilibrium distances lie in the spiral region, not far from the boundaries to the FM and AF phases. Expansion stabilizes the FM order, while compression brings RLs further into the SDW phase.

The phase diagram of the classical Heisenberg model as a function of the interactions between the first and second NNs summarizes very clearly the competition between these couplings and the resulting ground-state magnetic orders. The contrasting behaviors of the various Fe wires, including linear chains, ZZ chains and RLs at different interatomic distances, can thus be visualized from a local perspective. This approach is therefore complementary to the electronic structure viewpoint adopted in the previous section.

### 5.3 Summary

The magnetic properties of free-standing Fe wires having zig-zag and ladder geometries have been investigated from first principles in the framework of density-functional theory. The frozen-magnon dispersion relations have been determined and the stability of various magnetic configurations has been analyzed. The results show that Fe rectangular ladders develop spontaneously a noncollinear spiral ground state at the equilibrium interatomic distance. This behavior is qualitatively similar to the one observed in monoatomic linear wires. In the case of zig-zag stripes neither the periodic noncollinear orders nor the alternating parallel and noncollinear spin arrangements were found to be stable close to the equilibrium distances. In this case ferromagnetism clearly dominates.

The electronic structures underlying the collinear and noncollinear magnetic states have been analyzed by calculating the corresponding local densities of states for various representative wave numbers  $q$ . In this way, a bridge between the electronic structures of the collinear FM and AF states has been established. The stability of NC magnetic order has been correlated to the depletion of the DOS at the Fermi energy  $\varepsilon_F$  (pseudogap formation) and to the changes in the band width as a function of  $q$ . Effective exchange interactions  $J_{0\delta}$  between the local magnetic moments have been derived from the *ab initio* calculations in the framework of a classical Heisenberg model. The stability of the different magnetic phases has been thus explained from a local prospective, as the result of competing first and second NN interactions.





# Tuning spin-density waves in chains by means of external electric fields

In the present work we discuss the effect of an applied external electric field (EF) on the spiral SDWs spectra of 1D 3d TM nanowires (NWs) in the framework of first principles density-functional theory. The magnetic ground-states are analyzed in terms of frozen-magnon dispersion relations  $\Delta E(q)$  in the presence of external EF. Remarkably, an external EF stabilize the spiral SDWs in V chains, in contrast to Fe where the FM order remains most favorable. Moreover, it is interesting to noticed that external EF affects the magnetic and electronic properties such as local magnetic moment  $\mu$  and spin-polarized density of states  $\rho_{i\sigma}^d(\varepsilon)$ . We examine the relative magnitude and sign of the effective exchange interactions  $J_{ij}$ , which are derived by mapping a classical Heisenberg model energy relation to the calculated *ab initio*  $\Delta E(q)$  results, in order to get insight the nature of magnetic orders. We observe that applied EF mainly influences the nearest-neighbor coupling  $J_{01}$  whereas the interaction beyond  $J_{01}$  remains unchanged. Furthermore, the magnetic orders of V chains deposited on the Cu(110) substrate are investigated for few representative values of spin wave vector  $q$  in the presence of the external EF.

## 6.1 Introduction

The control of the magnetic nanostructures through external electric fields (EFs) opens new prospectives for the next generation of low-energy consumption memory, high density energy-efficient storage and spintronic devices [104–107]. Manipulating the properties of the materials by non-magnetic means is therefore highly appealing form both

fundamental and technological stand-points. Indeed, in the past years the effects of applied EFs on a number of magnetic properties have been demonstrated. This in particular effects the magnetic order [90] and its transition temperature, MAE [108,109] and exchange bias [110,111]. Electrically-induced bistable magnetization reversal was measured in MgO-based magnetic tunnel junctions at room temperature, demonstrating the capabilities of the EFs for magnetic data storage applications [105,112]. Furthermore, experimental and theoretical investigations have shown that the exchange interactions can be tuned in the presence of the external EF. For example, Ohno *et al.* showed that the ferromagnetism can be tailored by means of EFs in thin film semiconductor alloys, where ferromagnetic exchange coupling between the localized magnetic spins are mediated by the valence-band holes [113]. This control is also found in small clusters deposited on nonmagnetic transition-metal substrates [90,114]. Moreover, it has been shown that the MAE is highly sensitive to the EFs. In ultrathin films [109] and deposited linear chains [115] the MAE follows a linear like dependence with the electric field strength showing a considerable enhancement in its magnitude.

One-dimensional TM wires are of particular interest due to their unique electronic and magnetic properties, which may have direct technological implications [2,4,14,93,95]. Very recently, DFT calculations predicted that various free-standing 3d TM monoatomic chains such as V, Mn and Fe exhibit stable spin-spiral ground-state magnetic order [40–43,116,117]. These finding suggests that the stability of the wires may be altered if not only the geometrical but the electronic environment is modified. In this context, EFs seem to be the most promising route for tuning the electronic neighborhood of the linear chains due to their well-known ability for controlling locally the electronic and magnetic properties of the nanosized systems [105]. Thus, the aim of the present work is to explore the further conditions in which the spiral SDWs in the TM nanowires are preserved, enriching in this way, the previous research done [41,42].

In the present work, we investigate the effect of the external EF on the stability of the NC magnetic orders especially in V and Fe nanowires. In section 6.2, illustration of spiral SDWs in free-standing chains in the presence of the external EF along with the theoretical background and a brief summary of the electronic calculations are presented. The influence of the external EF on the structural, electronic and magnetic properties of V and Fe chains are discussed in section 6.3. The stability of spiral SDWs is analyzed in terms of the frozen-magnon dispersion relations under the influence of applied EF. Various studies have been reported that the substrates have a crucial influence on the magnetic coupling. Therefore, we analyze V chains on the Cu(110) substrate with a special regard to the possibility of NC configurations. Furthermore, the wire-substrate interaction is also by exploiting the external EF. We demonstrate that magnetic ground-state switches from AF to FM order due to electrostatically induced screening charges. Finally, in section 6.5 we conclude our main results.

## 6.2 Theoretical background

The spiral SDWs in infinite free-standing and deposited TM chains, characterized by their spin wave vector  $\vec{q} = [0, 0, 2\pi/(Na)]$ , are simulated within a supercell approach by constraining the direction of the local magnetic moment  $\mu_i$  at each atom  $i$  in the chain, being  $N$  number of atoms in the supercell and  $a$  is the NN distance. The direction of propagation is chosen along the wire axis ( $x$ -direction). The corresponding wave numbers  $q = |\vec{q}|$  are compatible with the assumed supercell periodicity condition:  $q = 2\pi n/(Na)$  with  $0 \leq n < N$  and  $n \in \mathbb{Z}$ . Thus,  $q = 0$  and  $q = \pi/a$  are refer to the FM and AF states. The effect of an external EF is introduced by adding a planar dipole layer in the middle of vacuum region [81]. In section 3.4 the theory of the external EF and its implementation for the present calculations has been described. The direction of the positive EF is set to be perpendicular to the plane ([001]-direction) of the nanowires. Due to the freestanding wire symmetry, the positive and negative values of EF do not alter the results. An illustration of applied external EF to a infinite free-standing wire having a spin wave  $\vec{q} = (\pi/4a, 0, 0)$  is shown in Fig. 6.1. The stability of spiral SDWs are investigated by varying the strength of EF.

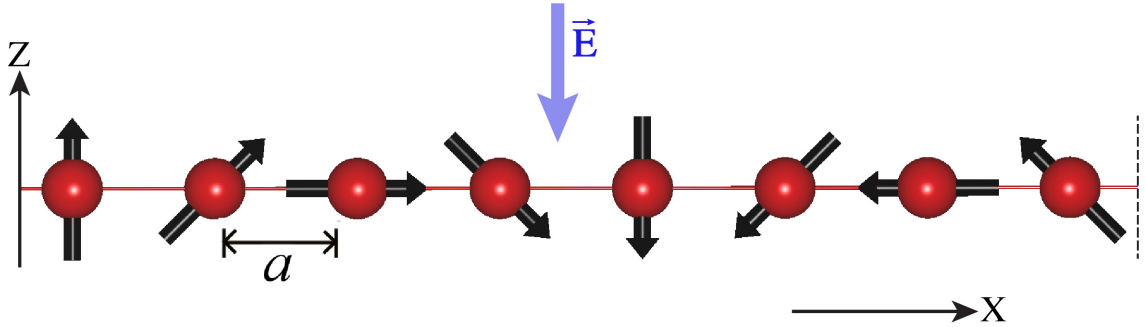


**Figure 6.1:** Illustration of the geometry and coordinate system for a spin spiral having  $\vec{q} = (\pi/4a, 0, 0)$ . The uniform electric field [ $\vec{E} = \hat{z}E_z$ ] is applied perpendicular to the chain.

### 6.2.1 Electronic calculations

We have performed fully NC calculations within the the PAW [75], as implemented in the VASP [78, 80]. The XC energy-functional is treated by using Perdew and Wang's spin-polarized GGA PW91 [71]. The spin-polarized KS equations are solved in an augmented plane-wave basis set taking into account the interaction between valence electrons and ionic cores. The wave functions are expanded in the interstitial region in

plane wave basis set having a cut-off energy of  $E_{max} = 500$  eV. The integrations in the BZ are performed by using Monkhorst-Pack scheme [79], with  $k$ -mesh of  $1 \times 1 \times 120/N$  which has been checked to yield suitable results for the present systems. We have used Gaussian smearing with a width  $\sigma = 0.05$  eV and performed series of calculations by systemically reducing the  $\sigma$  value until the entropy contribution to the total energies is less  $10^{-2}$  meV per atom. The local magnetic moments  $\vec{\mu}_i$  at atom  $i$  are calculated by integrating the magnetization density  $\vec{m}(\vec{r})$  inside the corresponding atomic WS sphere. For V(Fe) wires, the radius of WS spheres is  $R_{WS} = 1.323$  (1.302) Å, respectively. The criterion for the energy convergence has been set to  $10^{-5}$  eV and the force on each atom less than  $10^{-2}$  eV/Å.

The role of the substrate on the magnetic properties of the  $3d$  TM chains is probed by taking a Cu(110) substrate consisting of six layers<sup>1</sup>. The vacuum space between the periodic images is at least 16 Å in the direction normal to the surface. The experimental lattice constant  $a = 3.60$  Å is chosen. The wires are placed in the hollow sites of the Cu(110) surface along the  $x$ -direction. The in-plane separation between chains is approximately 11 Å, which is large enough to avoid possible interactions between neighboring chains. Geometrical relaxation is only allowed for the two outermost layers together with the chain atoms. The three bottom layers keep the bulk distance. For the collinear FM ( $q = 0$ ) and AF ( $q = \pi/a$ ), a two dimensional unit cell  $p(4 \times 2)$  was employed, whereas for the spin spiral configurations, ( $q = \pi/2a$ ), a larger supercell  $p(4 \times 4)$  was considered. Consequently, a  $k$ -mesh of  $10 \times 5 \times 1$  and  $5 \times 5 \times 1$   $k$  was used for the first and second case respectively. For the deposited wires, a cut-off energy of  $E_{max} = 400$  eV was set. It was checked that dense  $k$ -meshes and cut-off energies lead energy variations less than 1 meV per atom.

## 6.3 Spin-density wave spectra

### 6.3.1 Vanadium chains

First, we present the structural properties of V chains in the presence of an external EF, which is applied perpendicular to the chain direction. The calculated binding energy  $E_B = E_{tot} - E_{at}$  curves as a function of the lattice parameter  $a$  for different strength of the external EF are shown in Fig. 6.2. Here,  $E_{tot}$  are  $E_{at}$  are the total energy of V chain and isolated V atom in the presence of EF, respectively. The circles represent the DFT results, whereas the dotted lines are the nonlinear fits. The obtained results demonstrate that the external EF affects the NN distance  $a$  between the chain

<sup>1</sup>We find that upon increasing the number of atomic layers upto seven or more, the difference in the binding energy is less a 10 meV per unit cell.

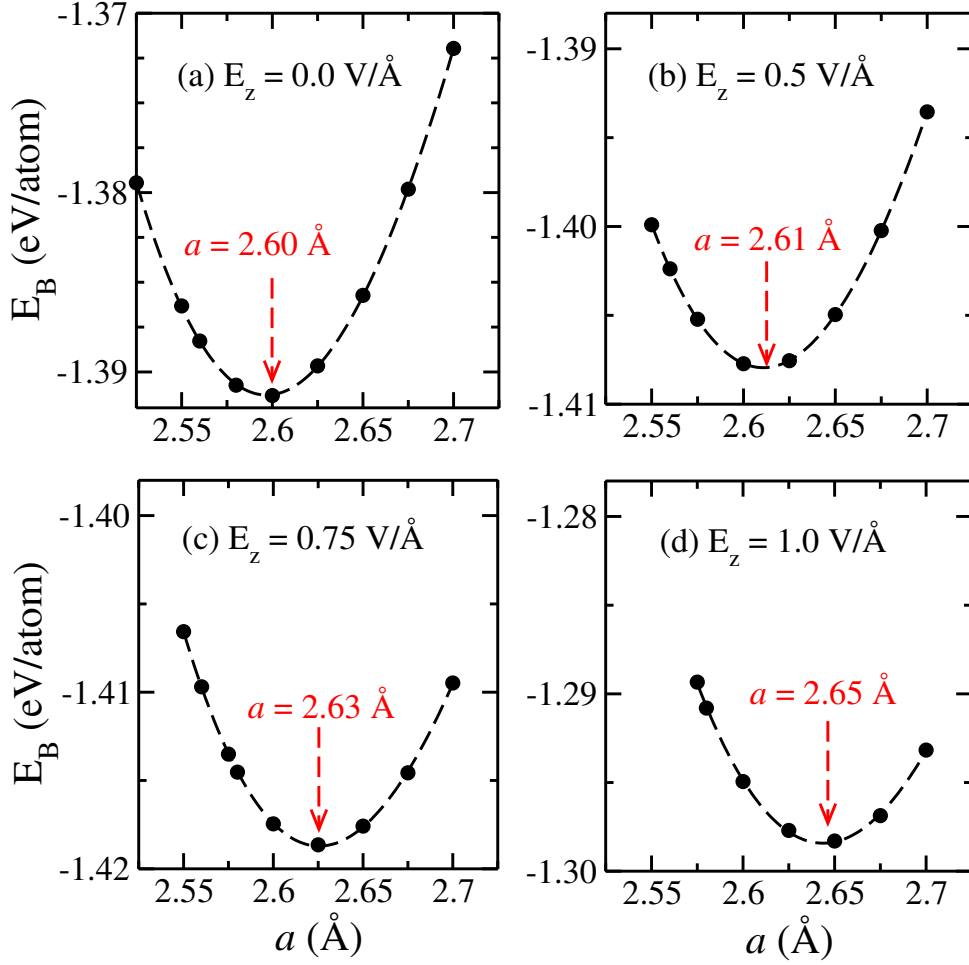


**Figure 6.2:** Binding energy  $E_B$  of one-dimensional V nanowires as a function of the lattice parameter  $a$  [see Fig. 6.1]. The considered values of the electric field applied perpendicular to the chain are given in the insets. The corresponding equilibrium lattice parameters are indicated.

atoms. As can be clearly seen in Fig. 6.2 (b-c), the external field elongates the lattice parameter around 0.4% (2.61 Å), 0.96% (2.63 Å), and 2% (2.65 Å) with respect to FM NN distance (2.6 Å) for  $E_z = 0.5, 0.75,$  and  $1 \text{ V/Å}$ , respectively. It is interesting to notice that the binding energy of V chains also increases with increasing the strength of the field ( $E_z \leq 0.75 \text{ V/Å}$ ), and then decreases for larger value of  $E_z$ . This increase in the lattice parameters  $a$  and the binding energies  $E_B$  occurs because the external EF enhances the electron coupling within the chain atoms. According to previous theoretical investigations, we noticed that a very small compression in NN distance  $a$  can change the electronic and magnetic properties of the 3d TM chains. For example, the spiral SDWs stabilized in V and Fe chains under certain pressure ( $a \leq 2\%$ ) [41, 42, 117].

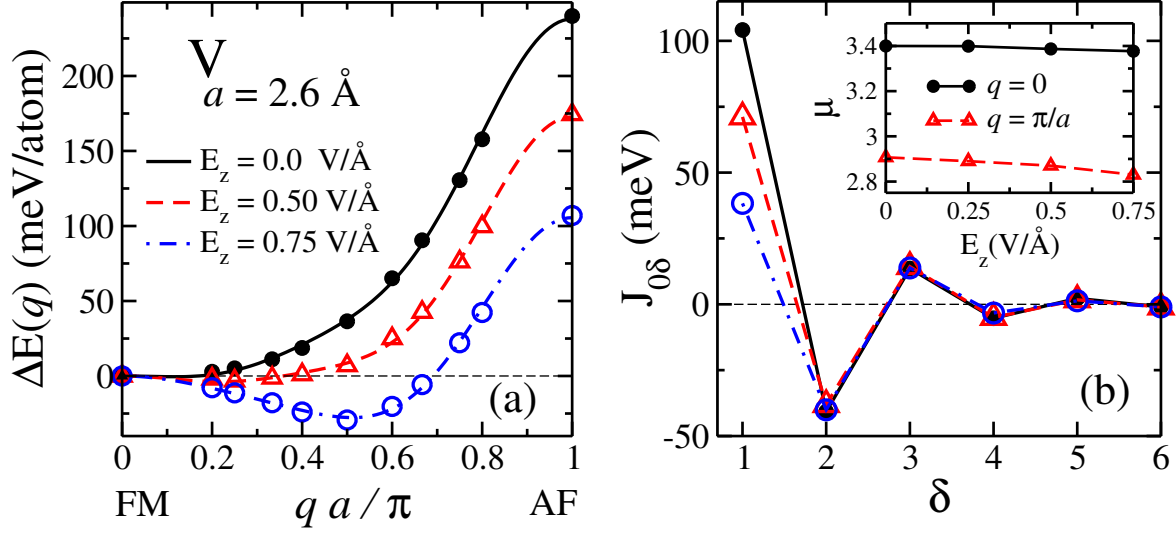


**Figure 6.3:** (a) Magnon dispersion relation  $\Delta E(q) = E(q) - E(0)$  in  $V$  chains for different values of the applied electric field  $E_z$ . The lattice parameter  $a = 2.6 \text{ \AA}$  is the equilibrium bond length corresponding to the FM order in the absence of  $E_z$ . The symbols refer to the *ab initio* calculations and the curves to the fit using a the classical Heisenberg with exchange couplings  $J_{0\delta}$  (3.16). (b) Effective exchange interactions  $J_{0\delta}$ , between a local moment  $\hat{\mu}_0$  and its  $\delta$ th nearest neighbor  $\hat{\mu}_\delta$  as a function of  $\delta$ . The inset shows the local magnetic moments  $\mu$  within the atomic Wigner-Seitz sphere for FM ( $q = 0$ ) and AF ( $q = \pi/a$ ) order as a function of  $E_z$ .

In the present work, we are interested to investigate the effect of the applied external EF on the stability of spiral SDWs in TM chains, which are strongly dependent on the NN distance  $a$ . As we discussed, the EF yields an external constrained (compression) on the chain atoms due to the screening charges, which responsible to elongate the interatomic distance between the chain atoms. In the other side, the bond length of the wires is fixed with the dimension of the supercell. The constrained produce due to the external EF is responsible for stability of spiral SDWs in  $V$  chains at the FM equilibrium lattice parameter  $a = 2.6 \text{ \AA}$ . In order to see this effect, we compute the magnon dispersion relation  $\Delta E(q) = E(q) - E(0)$  of  $V$  chains for two fixed values of  $a$  (i.e., FM bond length  $a = 2.6 \text{ \AA}$  and AF  $a = 2.05 \text{ \AA}$ ) in the presence of the external EF.

First, at relaxed FM NN distance  $a = 2.6 \text{ \AA}$ , Fig. 6.3 (a) shows the dispersion curves  $E(q)$  as a function of spin wave vector  $q$  for some representative values of  $E_z = 0.25, 0.50$  and  $0.75 \text{ V/\AA}$ . In the absence of the external EF ( $E_z = 0$ ), one notice that the FM state is energetically favorable over all the NC magnetic arrangements [41,42]. The AF state lies about 235 meV higher in energy than the FM one. When the EF switches on, the FM ground-state is not anymore remain favorable. For instance, the external

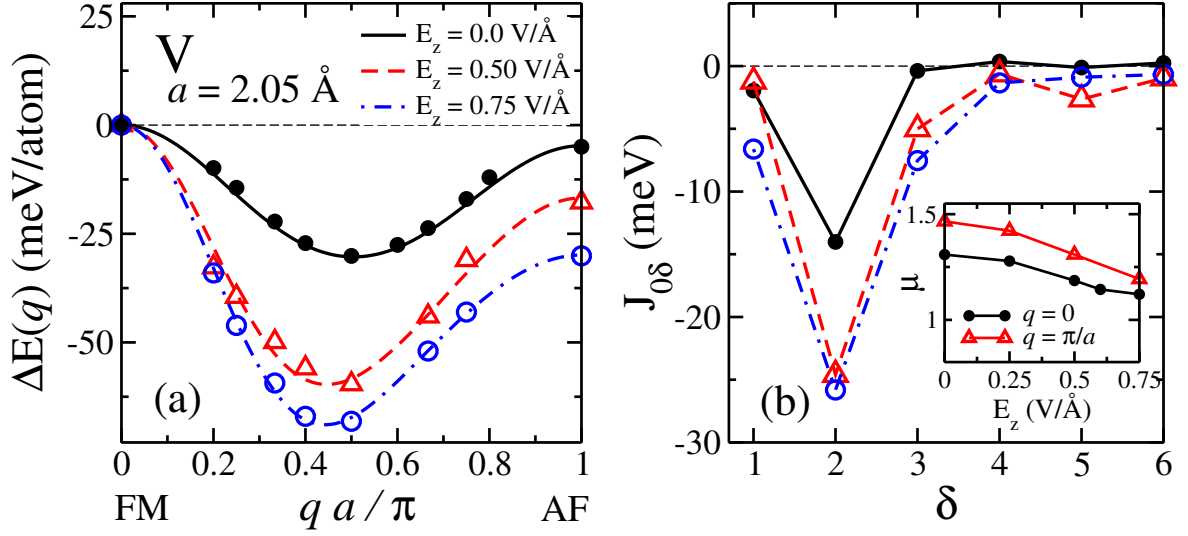


**Figure 6.4:** a) Magnon dispersion relation  $\Delta E(q) = E(q) - E(0)$  in V chains for different values of the applied electric field  $E_z$ . The lattice parameter  $a = 2.05$  Å is the equilibrium bond length corresponding to the AF order in the absence of  $E_z$ . The symbols refer to the *ab initio* calculations and the curves to the fit using a the classical Heisenberg with exchange couplings  $J_{0\delta}$  (3.16). (b) Effective exchange interactions  $J_{0\delta}$ , between a local moment  $\hat{\mu}_0$  and its  $\delta$ th nearest neighbor  $\hat{\mu}_\delta$  ad a function of  $\delta$ . The inset shows the local magnetic moments  $\mu$  within the atomic Winger-Seitz sphere for FM ( $q = 0$ ) and AF ( $q = \pi/a$ ) order as a function of  $E_z$ .

EF at  $E_z = 0.5$  V/Å yields a very weak (shallow) energy minimum of spiral SDW in between the FM and AF orders at  $q \simeq 0.2\pi/a$ , which is is around 1.5 meV/atom lower than the FM order. As the external EF strengthen, it is interesting to notice that the spin-spiral configurations become more stable. For  $E = 0.75$  V/Å, the spiral SDW energy minimum is around  $\Delta E(q) \simeq 28$  meV/atom lower than the FM order at  $q_{min} \simeq 0.5\pi/a$ . Our results show that the external EF has a significant effect on the stability of the ground-state magnetic order of V chains due to screening charges. Here, in Fig. 6.3 (a), the symbols represent the *ab initio* results, whereas the curves (lines) are fitted to the classical Heisenberg model energy relation (3.16).

The effective exchange interactions  $J_{0\delta}$  provide a more detailed analysis of the magnetic orders from a local prospective in TM chains. Fig. 6.3 (b) presents the exchange interactions  $J_{0\delta}$  in V wires between a local moment  $\hat{\mu}_0$  its  $\delta$ th nearest neighbors  $\hat{\mu}_\delta$  as a function of  $\delta$  for different values of the external EF. For  $E_z = 0$  V/Å, one observes that the first NN coupling  $J_{01}$  has a large positive value which dominates over all the other interaction terms and prefers the FM coupling. In contrast, the  $J_{02}$  exhibits a small negative value, resulting AF exchange coupling. As the strength of the external EF increases the magnitude of  $J_{01}$  tends to decrease, whereas the the values of  $J_{02}$

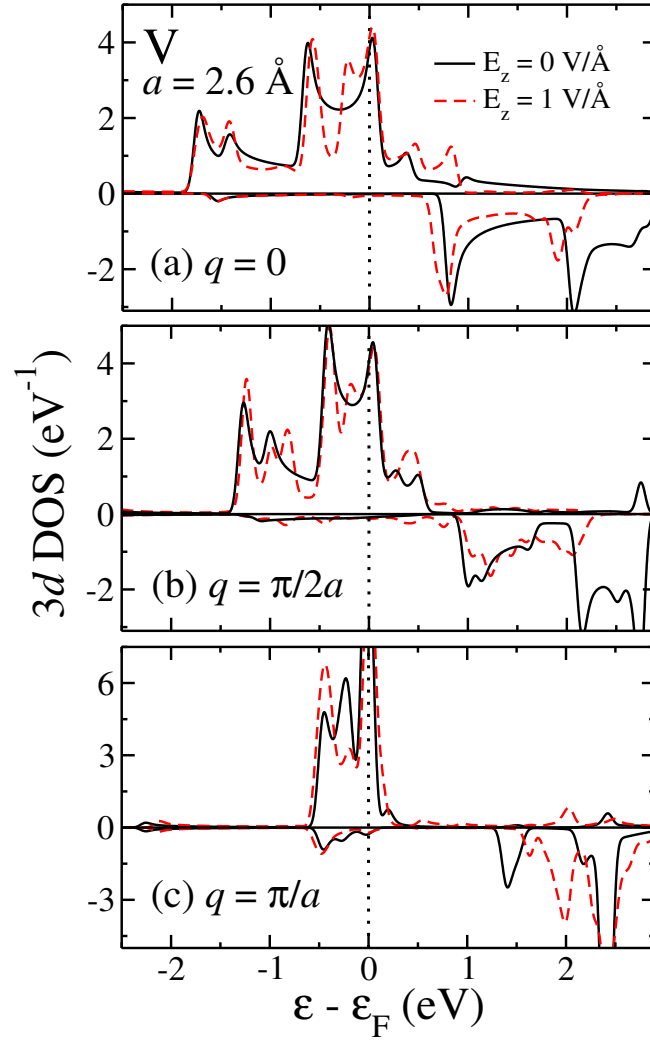


**Figure 6.5:** Spin-polarized 3d-electron local density of states (DOS) of V chains at the FM equilibrium NN distance 2.6 Å. Results are given for (a) FM order, (b)  $\pi/2a$  spiral and (c) AF order. The spin quantization axis is taken along the direction of the local magnetic moment  $\vec{\mu}_i$ . Positive (negative) values refer to major (minority) spin, while full (dashed) correspond to  $E_z = 0$  ( $E_z = 1$  V/Å).



and  $J_{03}$  are almost remains constant. However, for large value of  $E_z = 0.75 \text{ V/\AA}$ , the magnitudes of  $J_{01}$  and  $J_{02}$  become comparable. This competition between the first ( $J_{01} > 0$ ) and second NN ( $J_{01} < 0$ ) couplings leads to the magnetic frustration and stabilize the spin-spiral solution. The inset of Fig. 6.3 (b) shows the local moments  $\mu$  for  $q = 0$  (FM) and  $q = \pi/a$  (AF) orders as a function of  $E_z$ . In the absence of the external EF, the calculated local moments are  $\mu = 3.4 \mu_B$  and  $\mu = 2.9 \mu_B$  for FM and AF states, respectively. In both cases, the  $\mu$  decreases monotonously with the strength of  $E_z$ . This is due to the redistribution of the charge densities in the V atoms.

Moreover, we consider another case of V chain with AF NN distance  $a = 2.05 \text{ \AA}$  and compute the dispersion relations in the presence of the external EF as presented in Fig. 6.4 (a). First, we start the discussion when  $E = 0$ , we find that the magnetic ground-state is spiral SDW at  $q_{min} \simeq \pi/2a$ . The energy minimum of  $E(q)$  is around 30 and 25 meV lower than the FM and AF orders, respectively [41,42]. For large value of  $E_z = 0.75 \text{ V/\AA}$ , the external EF lowers the total energy of spin-spiral arrangements at  $q_{min} \simeq 0.47\pi/a$  with respect to others possible magnetic orders. This energy minimum is around 69 meV and 41 meV lower than the FM and AF orders, respectively. In Fig. 6.4 (b), we represent the exchange coupling  $J_{0\delta}$  parameters as a function of  $\delta$  for different strength of  $E_z$ . At  $E = 0$ ,  $J_{01}$  is negative but small in magnitude prefer AF solution. In this situation, when  $J_{01}$  is small, than  $J_{02}$  and  $J_{03}$  get more importance –  $J_{02}$  is even more large in magnitude than  $J_{01}$ . This corresponds to a deep spin-spiral energy minimum in the dispersion relation [see Fig. 6.4 (a)]. Remarkably, the magnitude of  $J_{01}$  and  $J_{02}$  become more negative in the presence of EF. The average of local moments  $\mu$  for  $q = 0$  and  $q = \pi/a$  are also plotted as a function of  $E_z$  in the inset of Fig. 6.4 (b). For  $q = 0$ ,  $\mu$  decrease monotonously with the strength of  $E_z$ , whilst the  $\mu$  totally quenched for larger value of  $E_z \geq 0.8 \text{ V/\AA}$ .

In order to qualitative insight into the microscopic origin of the relative stability of spin-spiral magnetic orders, we calculate the spin-polarized  $3d$ -electron local DOS  $\rho_{i\sigma}^d(\varepsilon)$  of V chains at the FM NN distance  $a = 2.6 \text{ \AA}$ . Results are given in Fig. 6.5 for  $q = 0$ ,  $q = \pi/2a$  and  $q = \pi/a$  in the presence of the external EF. In order to see significant effect on the local  $3d$ -DOS, we consider large value of the external EF such as  $E_z = 1 \text{ V/\AA}$ , and for the sake of comparison, DOS at  $E_z = 0 \text{ V/\AA}$  are also shown. At  $E = 0 \text{ V/\AA}$ , all the features of DOS are understand able as discussed in the earlier theoretical studied [41, 86, 97]. For  $E = 1 \text{ V/\AA}$ , the majority-spin  $3d$ -states ( $d_{x^2-y^2}$ -states not shown) just below the Fermi level are pushed towards the higher energy. At the same time, the minority-spin  $d$ -states moving towards the lower energies. As a result, the exchange splitting between the the majority and minority states are reduced. Thus, the decrease in the exchange splitting between the majority and minority states are responsible for reduction of local moments. The squeezing of  $d_{x^2-y^2}$  states suggests that the numbers of electrons decreases due to the external EF,

which can be calculated by integrating the local DOS within the sphere around each atoms with the radius equal to that of the WS sphere. A quit similar behavior have been observed in the DOS for  $q = \pi/2a$  in the presence of EF.

### 6.3.2 Iron chains

Similarly, we calculate the magnon dispersion relation  $\Delta E(q)$  of Fe nanowires at equilibrium NN distance  $a = 2.25 \text{ \AA}$  in the presence of applied external EF as shown in Fig. 6.6 (a). In the absence of external EF ( $E_z = 0$ ), the spiral SDW solution is the most stable one at  $q_{min} \simeq 0.2\pi/a$  and the energy is around  $\sim 10 \text{ meV/atom}$  lower than the corresponding FM order [41, 42]. When an external EF is introduced, we observe that the spin-spiral energy minimum becomes shallow and switches to FM order at  $E_z \geq 0.5 \text{ V/\AA}$ . Fig. 6.6 (a) shows the dispersion relations for two representative values of  $E_z$ . One notices that the effect of EF on spin-spiral arrangements for small values of  $q$  is very small, which is few meV/atom as compared to large value i.e.,  $q = \pi/a$ . For this reason, in a close window, we display the total energy difference  $\Delta E(q_{min}) = E(q_{min}) - E(0)$  at the most stable magnetic configuration having  $q_{min} = \pi/5a$  as a function of the external as shown in Fig. 6.6 (b). The plot is divided

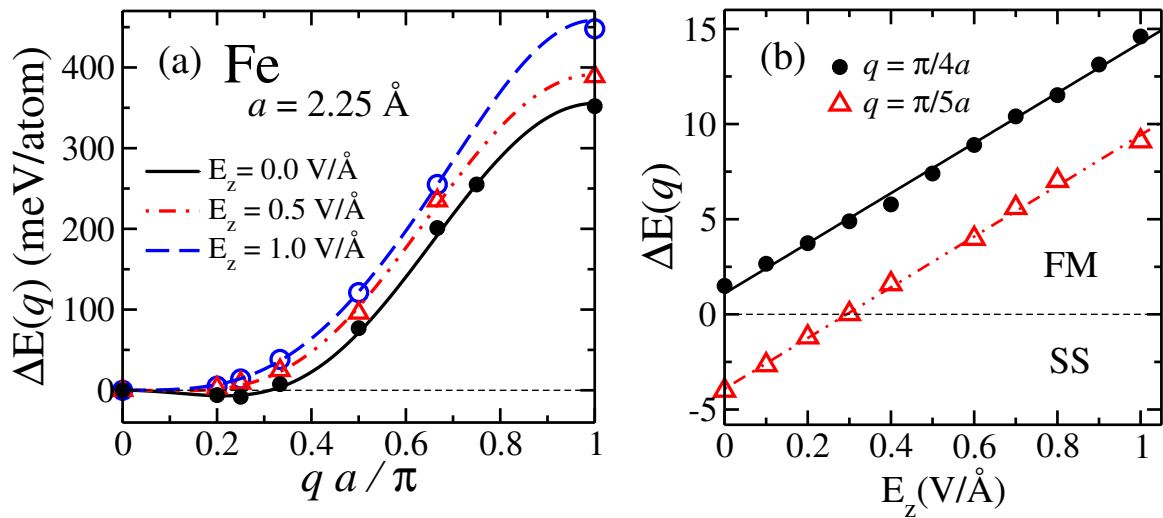


**Figure 6.6:** (a) Magnon dispersion relation  $\Delta E(q) = E(q) - E(0)$  in Fe chains for different values of the applied electric field  $E_z$ . The lattice parameter  $a = 2.25 \text{ \AA}$  is the equilibrium bond length corresponding to the FM order in the absence of  $E_z$ . The symbols refer to the *ab initio* calculations and the curves to the fit using a the classical Heisenberg with exchange couplings  $J_{0\delta}$  (3.16). (b) The energy difference  $\Delta E(q)$  as a function of  $E_z$  for two representative values of  $q$  is presented. The dashed lines are linear fit to the calculated results.

into two regions: one refers to FM and second spin spiral magnetic states. Our results

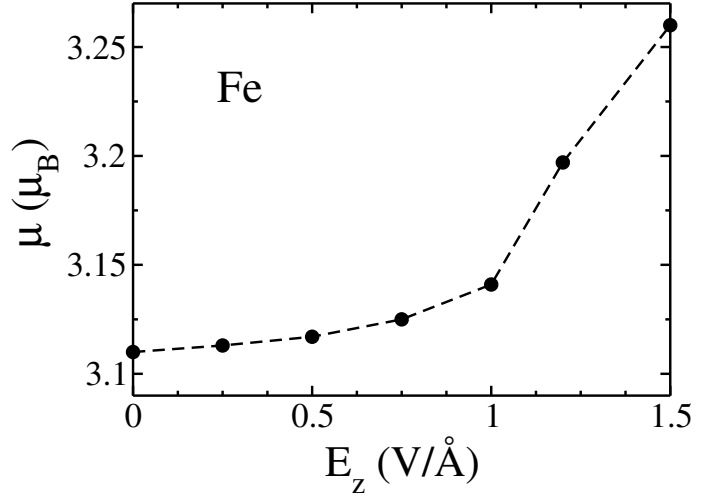


**Figure 6.7:** The local magnetic moment  $\mu$  within WS as a function of the electric field.

explore that the total energy of spiral SDWs is reduced linearly with the strengthen of  $E_z$ . For the sake of comparison, we consider an other magnetic arrangements with  $q = \pi/4a$  and calculate the energy  $\Delta E(q = \pi/4a)$  as a function of  $E_z$ . Here, the symbols refer to the *ab initio* calculations and the lines to the linear fit.

Fig. 6.7 shows that the change in the local moment  $\mu$  of Fe chains within the WS spheres as a function of EF strength. When an external EF is exposed to Fe chain atoms, the charge redistribution occurs within the orbitals. Such redistributions of charge density as usually accompanied by strong changes in the local magnetic moments. We notice that the  $\mu$  increases almost linearly when applied EF strength is  $E_z \leq 1$  V/Å. A considerable changes in  $\mu$  occur for  $E_z \geq 1$  V/Å.

To further gain insight into the influence of external EF on the relative stability of spiral SDWs and changes in the local properties, we have studied the spin-polarized local 3d-electron DOS  $\rho_{i\sigma}^d(\varepsilon)$  of Fe chains at NN distance  $a = 2.25$  Å for some representative wave numbers  $q$  ( $q = 0$ ,  $q = \pi/2a$  and  $q = \pi/a$ ) in the presence of the external EF. In Fig. 6.8, we display that the majority and minority spin components along the direction of a local moment  $\vec{\mu}$  for  $E_z = 0$  (full) and  $E_z = 1.5$  (dashed) curves, respectively. Appreciable changes occur in the electronic density of states, for example, in the case of  $q = 0$  for  $E_z = 1.5$  V/Å, the majority-spin states peak is shifted by  $\sim 229$  meV towards lower energies with respect to the peak of  $E_z = 0$ , while a little shift is observed in the minority-spin states. A very similar trend of shifting the majority-states has been observed for  $q = \pi/2a$  and  $q = \pi/a$ . Thus, the large exchange splitting between the majority and minority states (i.e.,  $n_\uparrow - n_\downarrow = \mu$ ) enhances the local moment  $\mu$  as shown in Fig. 6.7. A theoretical studies have recently revealed that unbalanced occupation of the majority- and minority-spin orbitals in the presence of an external EF results an enhancement in the local magnetic moment and MAE of iron

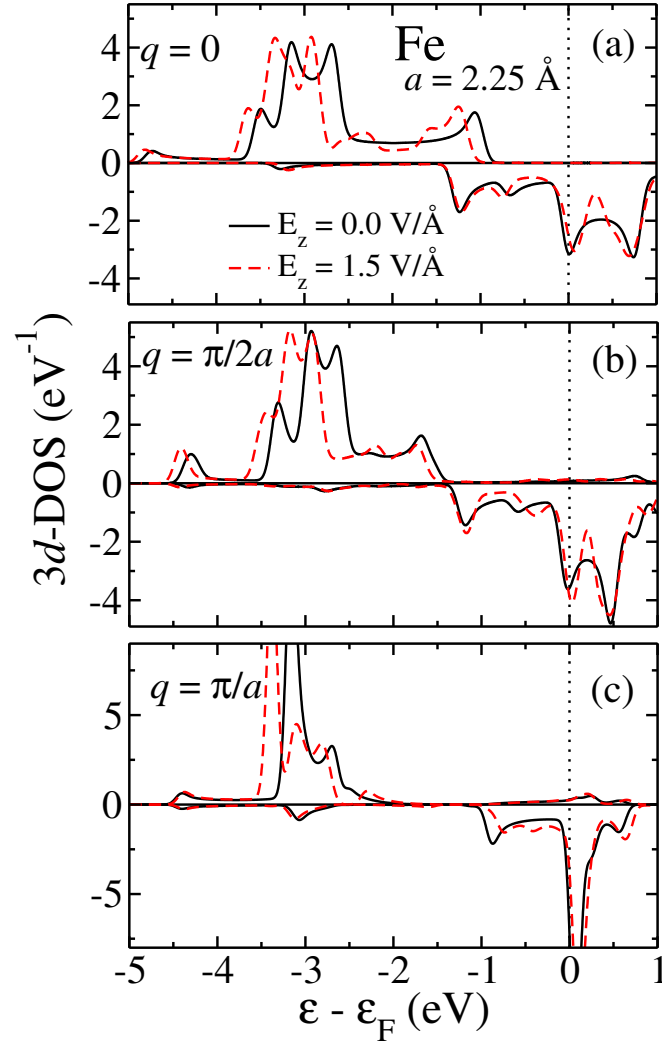


**Figure 6.8:** Spin-polarized 3d-electron local density of states (DOS) of Fe chains at the FM equilibrium NN distance 2.25 Å. Results are given for (a) FM order, (b)  $\pi/2a$  spiral and (c) AF order. The spin quantization axis is taken along the direction of the local magnetic moment  $\vec{\mu}_i$ . Positive (negative) values refer to major (minority) spin, while full (dashed) correspond to  $E_z = 0$  ( $E_z = 1$  V/Å).

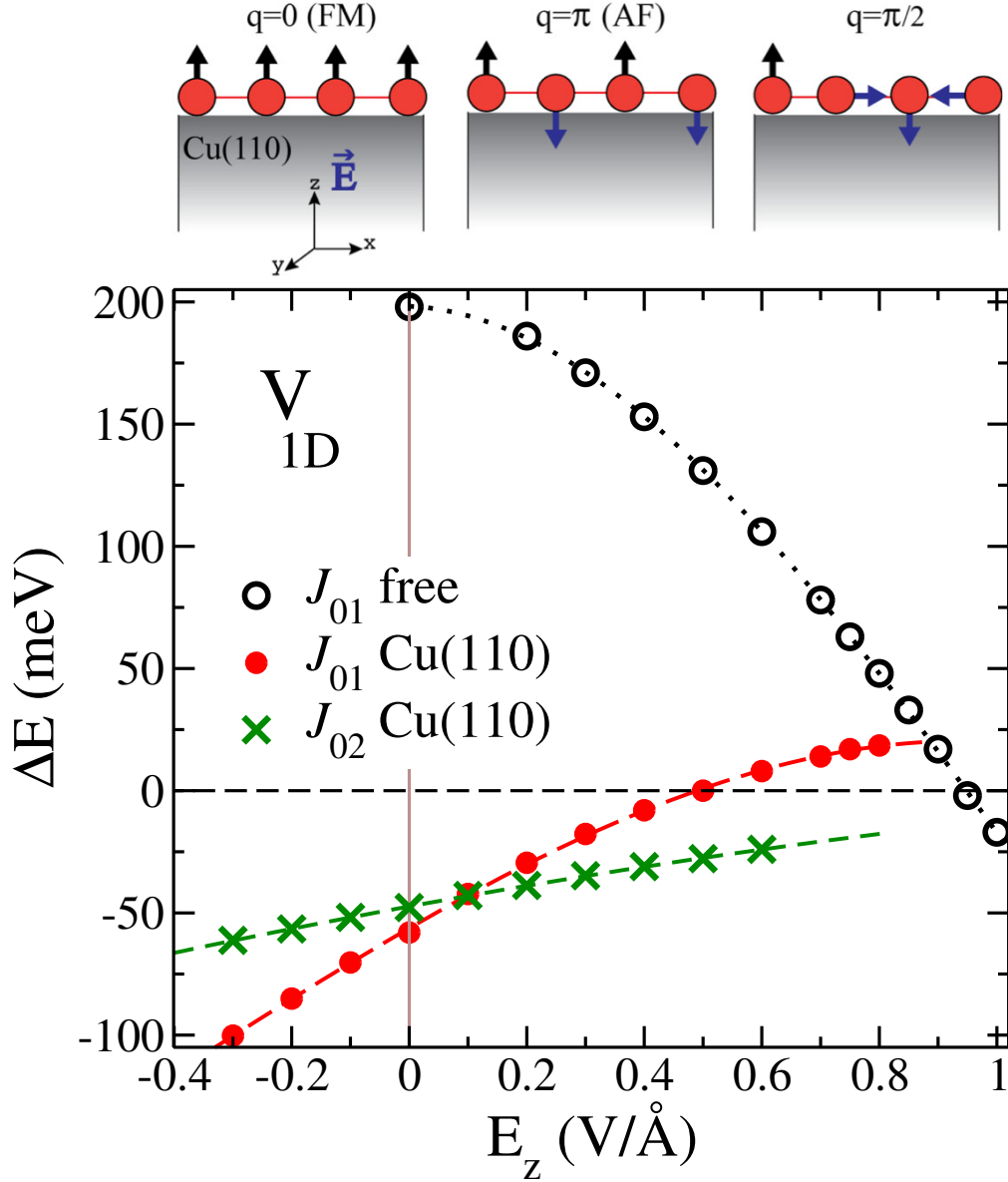
chain [118]. They explained the charge density distribution within the Fe orbitals by plotting the electron dispersion relation for different strength of electric field.

## 6.4 Vanadium chains deposited on Cu(110) surface

In order to interplay between the ground-state magnetic order of freestanding and deposited V chains on Cu(110) substrate as a function of the external EF ( $E_z$ ), we determine the exchange couplings  $J_{01} = E(\pi/a) - E(0)$  and  $J_{02} = E(\pi/2a) - E(0)$  as display in Fig. 6.9. Here,  $J_{01} > 0$  and  $J_{01} < 0$  correspond to the FM and AF orders, respectively. It is interesting to notice that the free-standing V chain exhibits FM order with a large exchange energy  $J_{01} \simeq 200$  meV, whereas the coupling between the deposited chain-atoms becomes AF with the exchange energy  $J_{01} \simeq -58$  meV. This effect causes due to the hybridization interaction. Remarkably, we notice that the magnetic order of the V chains is more sensitive due to the substrate effect [44]. Furthermore, large reduction of the local moment  $\mu$  yields from  $\mu = 3.4\mu_B$  to  $\mu = 2.21\mu_B$ , which is around 32% small in magnitude with respect to free-standing chain.

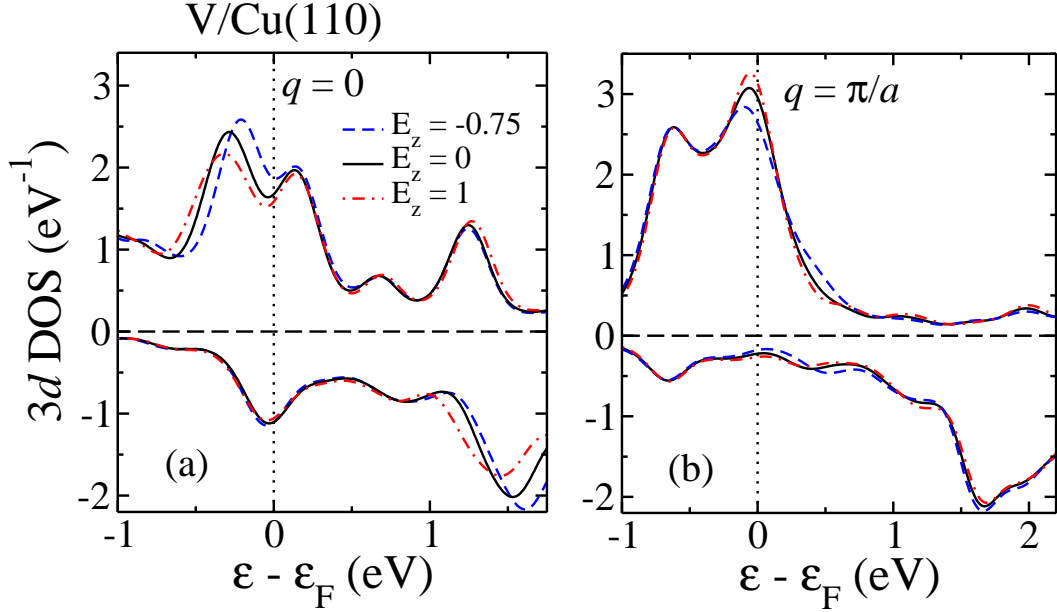
In the presence of the external EF the exchange coupling  $J_{01}$  continuously decreases (oppositely) for both freestanding and deposited wires [see Fig. 6.9]. Positive value ( $E_z > 0$ ) tends to reduce the strength of the FM coupling in the freestanding case. In contrast,  $E_z > 0$  tends to reduce the strength of the AF coupling in the case of deposit V chains. As a result, a transition from AF to FM order yields at  $E_z \simeq 0.5$  V/Å. The effect of an external EF on the stability of noncollinear spin structure having  $q = \pi/2a$  in deposited chains is also taken into account. The calculated results of  $J_{02}$  as a function of field is represented with blue curve in Fig. 6.9. For  $E_z = 0$  V/Å, we find that the spiral arrangements are not favorable over the AF order and the energy difference is found to be  $J_{02} - J_{01} \simeq 11$  meV. Remarkably, the NC spiral solution become more stable over the AF order under the influence of EF at  $E_z \geq 0.1$  V/Å. Moreover,  $J_{02}$  changes almost linearly in the whole regime of  $E_z$ . Our findings reveal that the external EF has a significant effect on  $J_{01}$  in both (free-standing as well as deposited V chains) cases as compared to the exchange coupling  $J_{02}$  of the NC spiral configurations.

Fig. 6.10 shows the spin-polarized  $3d$  local DOS of deposited chains with different strength of the external EFs for  $q = 0$  (FM) and  $q = \pi/2a$  (AF). In the presence of the EF, significant changes have been observed in preferentially occupied states (majority spin components) in the energy region between  $-1$  eV and  $0$  eV near the Fermi level for  $q = 0$ . Field  $E_z = 1$  V/Å tends to decrease the intensity of  $3d$ -states and pushes them to the lower energies, whereas  $E_z = -0.75$  V/Å increases the intensity and shifts



**Figure 6.9:** Upper panel: Illustration of three different magnetic arrangements (ferromagnetic, antiferromagnetic and spin-spiral) in the presence of applied electric field. Lower panel: Effective exchange couplings  $J_{0\delta}$  between the local magnetic moments in V chains deposited on the Cu(110) as a function of the electric field  $E_z$ , which is applied perpendicular to the surface. Results are given for nearest-neighbor ( $\delta = 1$ , dots) and next-nearest neighbor interactions ( $\delta = 2$ , crosses). For the sake of comparison the values obtained for freestanding V chains are also shown. In all cases the NN distance  $a = 2.55 \text{ \AA}$  within the V chains corresponds to an epitaxial growth on Cu(110).

the states toward higher energies. The shift in  $3d$ -states towards lower energies due to positive EF leads to higher the total energy of FM order which results an instability



**Figure 6.10:** Spin-polarized 3d local density of states (DOS) of V chains deposited on the Cu(110). Results are given for (a) FM and (b) AF order. The spin quantization axis is taken along the direction of the local magnetic moment  $\vec{\mu}_i$ . Positive (negative) values refer to major (minority) spin. Dashed, full and dotted lines correspond to  $E_z = -0.75$ , 0 and 1 V/Å, respectively.

towards the AF order, while negative EF shifts the states towards higher energies leads to lower the total energy. The overall energy shift in majority spin states is observed around  $\sim 0.1$  eV at the extreme value of applied EF ( $E_z = 1$  V/Å). That could be a reason for the instability of the AF magnetic order. In contrast, for  $q = \pi/2a$  (AF), the change in the intensities of 3d DOS at Fermi level are observed for  $E_z = -0.75$  and 1 V/Å. Moreover, the external EF gives rise to the redistribution of charges in the V chain atoms, and also responsible for the change in the intensity and shift in the 3d-states.

### 6.4.1 Charge and magnetization densities

An applied external EF distributes uniformly the charges on the metal surface. A sufficient large field alters the electron charge density due to the change in the number of electrons (occupation) at the surface of V/Cu(110) substrate. This change can affect the intrinsic properties of the system such as magnetic orders [90] and MAEs [109,119]. The induced charge density  $\Delta\rho = \rho(E_z) - \rho(0)$  is define to be the difference between the densities in the presence and absence of the external EF. Fig. 6.11 (a)-(b) shows

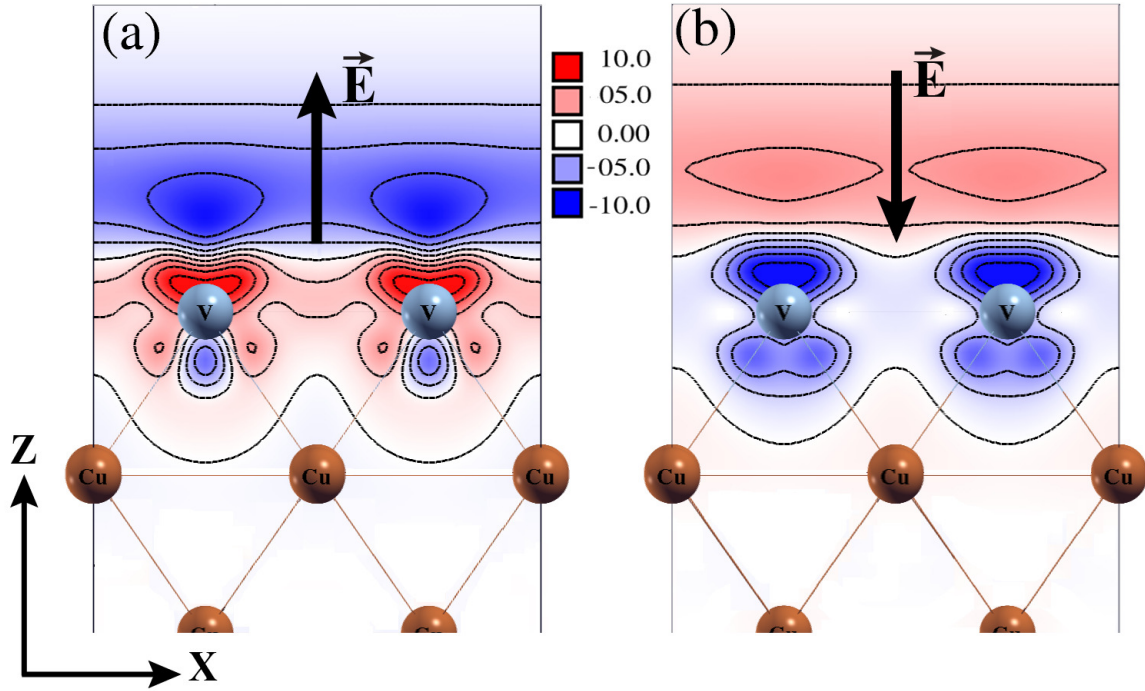


**Figure 6.11:** Difference between the spatial distribution of the screening charge densities: (a)  $\Delta\rho = \rho(-0.75) - \rho(0)$ , and (b)  $\Delta\rho = \rho(0.75) - \rho(0)$  of V chains on the Cu(110) substrate. The blue and red colors indicate depletion and accumulation of electrons, respectively. The positive (negative) electric field is defined to be pointed in (out) from the V/Cu(110) system. The red and blue surfaces represent  $10 \times 10^{-3} e/\text{\AA}^3$  and  $-10 \times 10^{-3} e/\text{\AA}^3$ , respectively.

that charge densities profile with respect to zero field. Here, positive and negative EFs are represented by outward and inward directions to the Cu(110) surface.

From the inspection of this plot, we find two alternating regions: the charge accumulation ( $\Delta\rho > 0$ ) region and charge depletion region ( $\Delta\rho < 0$ ). The depletion and accumulation regions are represented by blue and red contours, respectively. It is interesting to notice that the charge distribution across the V chains atoms is not symmetric in the presence of positive (negative) EF. For instance, in the case of positive field the electrons penetrate into the vacuum and produce deficiency of charges across the V atoms [see Fig. 6.11 (b)]. This deficiency of charges lower the total energy of the system and stabilized the AF state. Similarly, negative EF pushes the electrons from the V atoms to the Cu(110) substrate [see Fig. 6.11 (a)], which are responsible to higher the total energy and stability of the FM order.

For the further analysis, we compute the planar-averaged charge density by integrating the charge density of the  $xy$ -plane at each  $z$  coordinates as  $\Delta\rho_{\text{avg}} = \int \int_A \rho(x, y, z) dx dy$ . Fig. 6.12 illustrates  $\Delta\rho_{\text{avg}}$  as a function of the  $z$ -coordinate



for two representative values of  $E_z$ . Here, the first and second vertical dotted lines refer to the position of the upper most Cu layer and V chain atoms, respectively. It is seen that the amplitude of the depletion charge densities on the V atoms increases with the strengthen of  $E_z$ . Moreover, the screening charges indicate that the bulk electrons play a major role in the presence of the external EF. The main purpose is to evaluate the displaced (injected) numbers of electrons in the present system. Our results suggest that around  $q \simeq 0.59|e|$  electrons are removed from the system at  $E_z = 0.5 \text{ eV/\AA}$  when a magnetic order transition from AF to FM takes place.

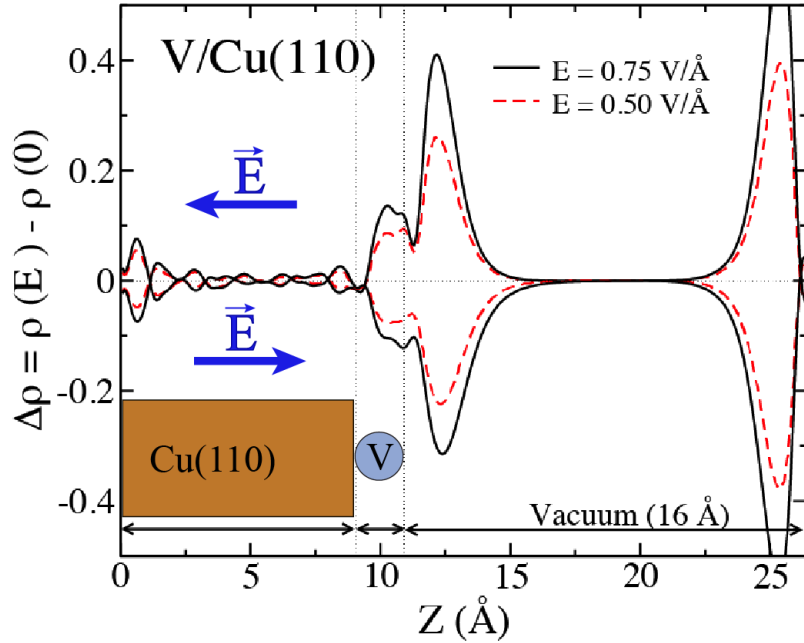


**Figure 6.12:** Average screened charge density difference,  $\Delta\rho_{\text{avg}} = \rho(E_z) - \rho(0)$ , in a parallel plane to the surface ( $xy$ -plane) along the  $z$ -direction, which is normal to the Cu(110) substrate for positive and negative electric fields. Positive and negative values of  $\Delta\rho_{\text{avg}}$  refer to remove and add the electrons to the system in the presence of the external fields.

## 6.5 Conclusion

Our first-principles investigations showed that the magnetic properties of one-dimensional V and Fe chains can be tuned in the presence of the external electric field. The stability of spiral SDWs has been analyzed by determining the magnon dispersion relations  $\Delta E(q)$ . Our results revealed that the magnetic ground-state of free-standing V chains switches from the stable FM order to spiral SDWs in the presence of an applied external EF at the equilibrium interatomic distance  $a = 2.6 \text{ \AA}$ . Moreover, the stability of

NC spiral configurations further enhanced with the strengthen of the external EF at both FM and AF NN distances. In contrast to V, the ground-state magnetic order of Fe chains has been switched from spin-spiral to FM state at  $E_z \geq 0.3 \text{ V/\AA}$ .

To investigate the hybridizational effect between the wires and metallic surface, which can be appreciably modified the couplings between the local moments  $\mu$  and the electric properties of the wires [43]. We have performed calculations of V chains deposited on the Cu(110) substrate as a perspective example. In the absence of EF ( $E_z = 0 \text{ V/\AA}$ ), similar to other studied, we found that the magnetic solution is AF ( $J_{01} < 0$ ). Interestingly, the strength of AF coupling decreases with the increase of the strength EF towards positive values. At  $E_z \geq 0.5 \text{ V/\AA}$ , a transition of magnetic order from AF to FM coupling have been observed. Moreover, we noticed that the EF has in general a strong influence on the FM state of deposited wire than the AF one. In contrast, negative applied EF stabilize AF magnetic arrangement. Furthermore, spin-spiral magnetic structure having  $q = \pi/2a$  become more favorable at  $E_z \geq 0.25 \text{ V/\AA}$ .

As a conclusion, it is demonstrated that the external EF modifies the ground-state magnetic orders in both freestanding and deposited  $3d$  chains. Thus, it can be used as a promising tool for tuning the electric and magnetic properties of novel magnetic materials.

# Noncollinear magnetism in 3d transition metal chains on graphene

The substrate hybridization effect on the magnetic properties of TM chains is crucial for the stability of the magnetic orders as well as magnetic anisotropy energy like properties. Therefore, choice of a suitable substrate is extremely challenging. In fact, in the present work, we are interested to investigate the stability of spiral SDWs in 3d TM chains, which are strongly dependent on the NN distance as we have discussed in earlier studies [41, 117].

In the present study, we explore the structural, electronic and magnetic properties of 3d TM (V, Cr, Mn, Fe and Co) monoatomic chains deposited on a graphene nanosheet and TM-terminated zigzag graphene nanoribbons (GrNRs). The favorable magnetic structures are investigated by the analysis of corresponding binding energies  $E_B$  for TM chains deposited at various positions on the graphene sheet. The stability of NC spiral configurations are quantified by computing the frozen-magnon dispersion relation  $\Delta E(q)$  as a function of  $q$ . Remarkably, it is found that Mn chains on a graphen sheet develop a spontaneously spin-spiral structure, whereas V, Cr, Fe, and Co chains show collinear ground-state magnetic order. In the case of TM-terminated GrNRs, V and Fe wires stabilize spiral arrangements. Effective exchange interactions  $J_{ij}$  between the local magnetic moments  $\mu$  are derived by mapping the *ab initio* results to a classical Heisenberg model. The stability in the NC magnetic arrangements are explained as the result of the interplay between competing  $J_{ij}$  NN interactions. Finally, we include the spin-orbit interaction in the calculations and determine the magnetic anisotropy energy (MAE). The results show that Fe and Co chains yield significant magnetic anisotropy energies and orbital magnetic moments of the order of few meV. They are,

thus, potential candidates for high-density magnetic storage. Moreover, the calculated MAEs for V, Cr, and Mn chains are relatively small in magnitude.

## 7.1 Introduction

Graphene is a 2D material made of carbon atoms strongly bonded in a honeycomb-like lattice. It become promising in materials science including physics, chemistry, and biology due to its numerous intriguing properties [49]. Graphene monolayers are often used as a substrate because of their high-room-temperature carrier mobility [46], quantum Hall effect [47,48] and easy growth. Moreover, the electronic structure of the graphene monolayer shows a linear energy dispersion, near Fermi energy  $E_F$  i.e., massless Dirac fermions, which offers new exciting opportunities for spintronic devices [50]. Graphene is a particularly promising field for spintronics devices due to the weak spin-orbit and hyperfine interactions, which in other materials field significant spin relaxation and decoherence [120]. Tuning the electronic structure of graphene and at the same time realizing the desired spintextures is a challenging task. The electronic and magnetic behavior of graphene can be tuned to some extent by some chemical adsorbates [121,122], by varying the thickness of graphene monolayers [123,124], by means of interactions with substrates [125], introducing contact with metals [126], by suitable metal impurities [127,128], or by means of external applied electric fields [51].

A few studies of metal impurity including single magnetic adatom, 1D chains and small clusters deposited on the graphene sheet have been performed in the past [129–131]. In introducing TM impurities in graphene systems has become a popular choice to enhance the interactions and give rise to magnetic moments. Therefore, it is important to understanding the interaction between adsorbates and graphene for fabricating new electronic devices for technological applications and transport experiments [129,130]. Recently, a significant progress from both experimentally and theoretically points of view has been advanced in this direction in order to give a nanoscale understanding of the interactions between the TM adatoms and graphene [132,133]. Especially, 3d TM magnetic impurities have gained much attention due to their possibility of inducing spin polarization and magnetic properties in graphene. These studies mainly investigated the stable structural arrangements of metal adatoms on graphene [131,134].

The physics of magnetic nanostructures, particularly low-dimensional systems including small particles of various size, 1D nanowires etc, is remarkably interesting from both fundamental and technological prospective [3]. Now a days, experimentally, it has been demonstrated that arrays of atoms can be formed by manipulating individual atoms using a STM-tip on various magnetic and nonmagnetic monolayers [102]. A vast

variety of magnetic adatoms interaction with graphene have been investigated both experimentally using spin polarized STM as well as theoretically [127, 129, 130]. These studies have opened the new exciting possibilities to address the electric and magnetic properties locally of these system. This includes particular the Kondo effect in Co adatoms on GrNR [135]. The isolated  $3d$  TM adatoms on graphene sheet have been intensively investigated both experimentally and theoretically. However, monoatomic wires and small clusters including few atoms have remains unexplored so far [128, 131].

In general, an isolated graphene sheet is nonmagnetic. It usually become magnetic in the vicinity of doping magnetic impurities, due to hydrogenation or through defect control such as vacancies or forming nanoribbons [136–138]. Now a days, it is experimentally possible to construct GrNRs with both sharp edges zigzag and armchair by cutting the graphene along two high-symmetry crystallographic directions. The TM-terminated GrNRs with armchair or zigzag can be excellent candidates for spintronic related applications due to *flat-band magnetism* induces by peculiar localized electronic state at each edge [139, 140].

Further investigations are important in order to understand how the electronic and magnetic properties of GrNRs can be affected by TM termination. Very recently, TM terminated GrNRs have been shown large spin polarizations and magnetoresistance. Another similar study focused on the change in magnetic order or inter-edge magnetic coupling of Fe-, Co-, and Ni-terminated GrNRs as a function of ribbons widths  $w$  [141, 142]. They found that the total energy difference between the FM and AF orders decreases with increasing the width of zigzag nanoribbons, whereas a nonlinear behavior is observed in the case of armchair nanoribbons. In our present chapter, we are interested in both inter-edge couplings as well as in the stability of NC magnetic structures in TM chain atoms which are directly attached on both sides of nanoribbons [see Fig. 7.1 (b)].

Another essential property of magnetic systems, especially in low-dimensional nanostructures, is the MAE which originates from SOC and describes the tendency of saturated magnetization to align along specific high symmetry directions. The MAE is defined as the energy difference  $\Delta E$  between two symmetrically inequivalent directions of magnetization: a low-energy axis (easy axis) and a high-energy axis (hard axis). It depends on the geometry and electronic structure of the system. However, most bulk material posses little MAE due to the quenching of orbital angular momentum. For instance, bulk Co in hexagonal closed-packed (hcp) structure yields the largest MAE among ferromagnetic elements ( $\Delta E \simeq 0.06$  meV/atom). Reduced dimensionality plays an important role in order to enhance the MAE of TM systems. For example, an isolated Co atom shows zero MAE due to its spherical symmetry, while TM chains or dimers have much larger MAE then the corresponding solids. For example, the Co

dimer has a MAE of 7–50 meV/atom [143,144]. Moreover, the MAE can also be tuned by the deposition of low-dimensional TM nanostructures on suitable highly-polarizable substrates (e.g., Pd, Pt, and Ir) [4,45,145]. However, other deposition processes may dramatically reduce the MAE due to changes in symmetry and electronic structure. Therefore, in order to utilize the giant MAE of low-dimensional TM nanostructures, a suitable combination of nanostructures with substrate must be found out.

Considerable theoretical work on this subject has been done, in this context focused on the adsorption of adatoms on carbon nanostructures. Nevertheless, in our knowledge, the NC magnetic structures of 3d TM chains have not been investigated yet. In this chapter, we investigate the structural, electronic, and magnetic properties of V, Cr, Mn, Fe and Co monatomic chains, including collinear and noncollinear magnetic configurations, deposited on a single graphene sheet and terminated GrNRs. The remainder of the chapter is organized as follows. In section 7.2, we present the computational procedure along with the structural models of simulated systems. An overview of theoretical methods (DFT) may be found in section 2.1. The structural, electronic, and magnetic properties of the deposited TM chains are discussed in section 7.3. The stability of chains is analyzed by calculating the binding energy  $E_B$ . In section 7.4, we perform NC spin spiral calculations and analyze the magnetic ground-states in terms of the corresponding frozen-magnon dispersion relations for TM chains deposited on the Gr sheet and TM-terminated GrNRs. Relativistic effects, in particular SOC effects, are discussed in section 7.5. Finally, in section 7.6, we summarize our results.

## 7.2 Computational details

Fig. 7.1(a) illustrates a simulation unit cell and the geometrical structure of TM wires deposited on the Gr sheet. The chain graphene system is modulated using a periodic  $2 \times 6$  graphene supercell having  $4.98 \times 12.86 \times 16$  Å and periodic boundary conditions along  $x$ - and  $y$ -direction. The supercell contains 24 C atoms and 2 of TM atoms. A 16 Å wide vacuum in the  $z$ -direction is chosen to avoid the interaction between the neighboring images. We employ the optimized graphene lattice parameter  $a = 2.467$  Å (i.e., C-C distance 1.425 Å) which is in good agreement with others theoretical and experimental studies. In order to find the most favorable adsorption position of TM chain atoms on the Gr sheet, we optimize the structure of geometry of TM chains at three different sites such as at the top of the C atom ( $T$  site), center of a hexagon ( $H$  site) and at the middle of C-C bond ( $B$  site).

A second example of carbon nanostructures are zigzag GrNRs which are periodic only in  $x$  direction and have a finite width ( $w$ ). The width  $w$  of a nanoribbon consists

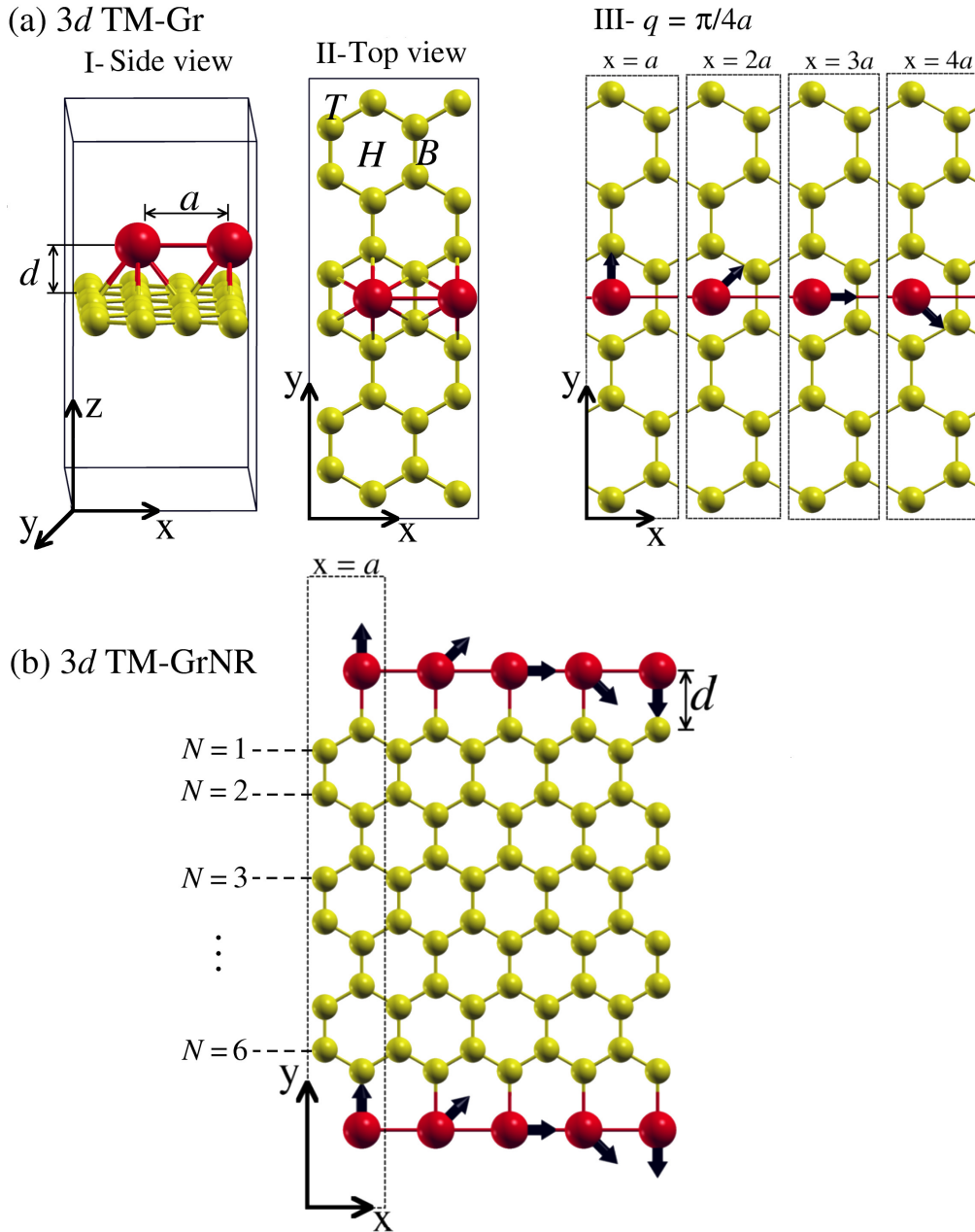


**Figure 7.1:** (a) Relaxed atomic structures of TM chains deposited on a graphene sheet: I side view, II top view, and III a model of spiral SDW in which the direction of local magnetic moment  $\mu_i$  having a wave vector  $q = \pi/4a$  is depicted. The leftmost unit cell [III-  $x = a$ ] is used for the calculation of dispersion relation  $\Delta E(q)$  and the others are merely represent the propagation of the spiral throughout the lattice. The lattice sites are attached with a translational periodic length  $a$  along the  $x$ -direction. Here,  $a$  and  $d$  are the NN distances between the TM-TM and TM-C atoms, respectively. The TM chain atoms are located at hollow position ( $H$  site). (b) Illustration of the unit cell of TM-terminated GrNRs for spiral SDW calculations. Red and yellow spheres represent the TM and graphene atoms, respectively.

of a number of dimer lines  $N$  [see Fig. 7.1 (b)], where the TM atoms are directly attached to the NN carbon atoms on both sides of the ribbon. The chain atoms are repeated in  $x$ -direction, whereas a space of  $14 \text{ \AA}$  is used between two edges ( $y$ -direction) and perpendicular to the plane of the graphene sheet ( $z$ -direction) in order to prevent the interaction between neighboring images. In the present calculations, we consider nanoribbons having width  $w \simeq 11.5 \text{ \AA}$  ( $N = 6$ ) which is sufficient large enough distance to avoid the interaction between the TM atoms. The nanoribbon width larger than  $11.5 \text{ \AA}$  or ( $N > 6$ ) is not playing a significant changes on the properties of our systems [see Fig. 7.1 (b)].

The structural, electronic and magnetic properties of TM chains deposited on graphene nanostructures has been investigated within the PAW formalism, as implemented in VASP [78]. The considered XC energy-functional is Perdew and Wang's spin-polarized GGA PW91) [71]. The KS wave functions are expanded in the interstitial region in plane wave basis set with a cut-off energy of  $E_{max} = 500 \text{ eV}$ . The BZ integrations are performed by using Monkhorst-Pack scheme with k-mesh of  $20 \times 5 \times 1$  and  $50 \times 1 \times 1$  for Gr sheet and nanoribbon, respectively. All atomic positions and lattice parameters are optimized by using the conjugate gradient method where total energy and atomic forces are minimized. We use a Gaussian smearing with a width of  $\sigma = 0.05 \text{ eV}$ , this value ensure an entropy contribution to the free energy less than  $1 \text{ meV/atom}$ . The local magnetic moment  $\vec{\mu}_i$  at atom  $i$  is calculated by integrating the magnetization density inside the corresponding atomic WS sphere. The radius of WS spheres considered in the calculations are  $R_{WS} = 1.323 \text{ \AA}$  for V, Cr, and Mn,  $R_{WS} = 1.302 \text{ \AA}$  for Fe and Co, and  $R_{WS} = 0.868 \text{ \AA}$  for C. Convergence of the calculation is assumed when the total energy difference of the two last consecutive steps is less than  $10^{-5} \text{ eV}$  and the Hellmann-Feynman forces on each atoms are less than  $10^{-2} \text{ eV/\AA}$ .

We performed fully unconstrained NC magnetic calculations within the PAW formalism, as implemented in VASP [80]. In this framework density functional theory is formulated in terms of a  $2 \times 2$  density matrix. The frozen-magnon dispersion relations are calculated by applying the generalized Bloch theorem [85]. This approach is computationally much more efficient, because we do not need a very large supercell in order to compute the total energy for very small value of  $q$  [section 3.1.3 for further details]. In order to get advantage of this approach, we construct a supercell with  $1 \times 6$  dimension containing 12 atoms for both Gr sheet and GrNR. In the case of Gr sheet, 1 TM atom is located at the  $H$  site. The periodic boundary conditions along the  $x$ -direction yields a linear chain. In the case of GrNR, 2 TM atoms are directly attached with NN C atoms on both edges. Fig. 7.1 illustrates a model of a spiral SDW with wave vector  $\vec{q} = (q, 0, 0)$  for both the Gr sheet and the GrNR. The Brillouin zone integrations are sampled using  $30 \times 10 \times 1$  and  $50 \times 1 \times 1$  Gamma-centered Monkhorst-Pack grids for



the calculations of the Gr sheet and GrNR, respectively. A number of tests have been performed in order to improve (minimize) the numerical accuracy (error) of the calculations. We have found that cut-off energy and  $k$ -mesh larger than  $E_{max} = 500$  eV and  $30 \times 10 \times 1$  ( $50 \times 1 \times 1$ ) for both systems yield a total energy difference of less than 1 meV/atom [see Fig. 7.1 (a–III) and (b)]. In order to get most favorable magnetic configurations with lowest energy structures, we performed structural relaxation calculations by relaxing the TM atoms as well as the Gr sheet.

The calculation of MAE of TM chains deposited on the Gr sheet is performed by using the magnetic force theorem where MAE is related to the energy difference for different magnetization axes by introducing the SOC in a non-selfconsistent way. The MAE is calculated by using the supercell as shown in Fig. 7.1 (a–II) with large cut-off  $E_{max} = 500$  eV and  $30 \times 10 \times 1$   $k$ -mesh. The considered parameters ensure the total energy difference less than 0.5 meV/atom.

### 7.3 Structural and electronic properties of TM chains deposited on the graphene and terminated nanoribbons

The binding energy  $E_B$  as the difference between the total energy of the relaxed TM chains on the Gr sheet ( $E_{chain/Gr}$ ) and that of the isolated perfect Gr sheet  $E_{Gr}$  and the energy  $E_{iso}$  of the corresponding isolated TM atom is given by

$$E_B = [E_{chain/Gr} - E_{Gr} - nE_{iso}]/n$$

and, similarly for graphene nanoribbons (GrNR)

$$E_B = [E_{chain/GrNR} - E_{GrNR} - nE_{iso}]/n .$$

where  $n$  is the number of TM atoms in chains. In order to minimize the errors in the binding energy, we employ with same supercell dimension, the  $k$ -mesh and cutoff energy for the calculations of the TM-chain deposited on the graphene sheet (TM-terminated nanoribbons) and isolated graphene (nanoribbons).

As a first step, we optimize the structures of TM chains at various positions such as on top of C atoms ( $T$  site), in the middle of a graphene hexagons or hollow sites ( $H$  site) and at a bridge site ( $B$  site) which correspond to TM atoms located above C-C bonds.

A possible adsorption or migration pathway along  $T \rightarrow H \rightarrow B$  sites on the Gr sheet along with the calculated binding energy  $E_B$  is presented in Fig. 7.2. Note that,

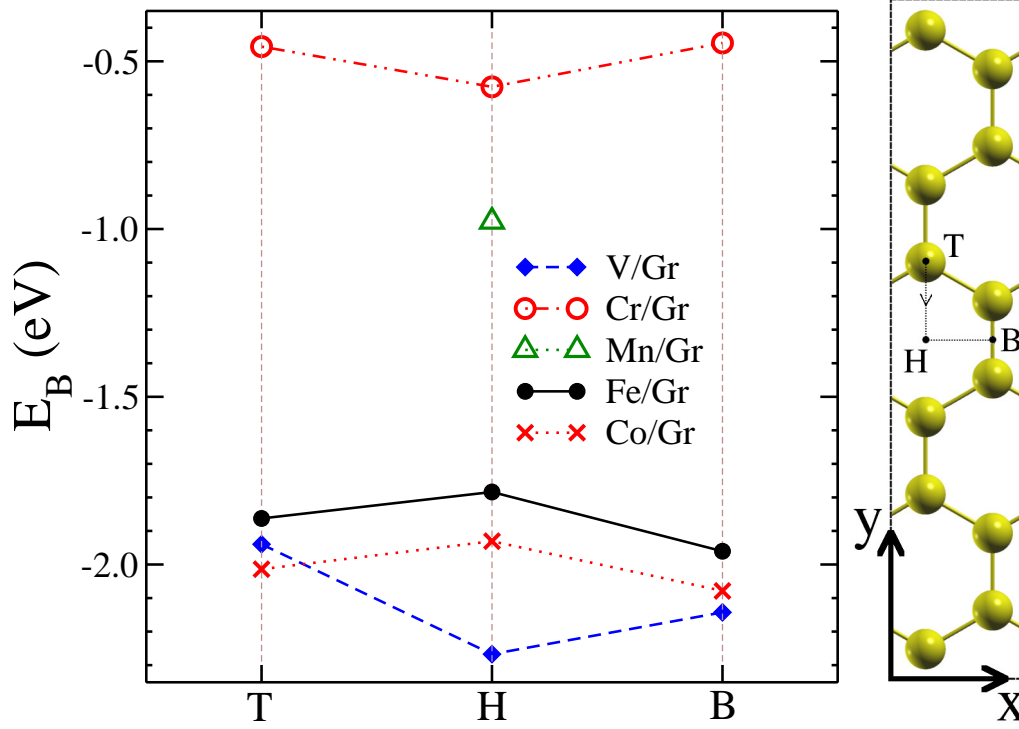


**Figure 7.2:** The variation of binding energy  $E_B$  of TM chains at different adsorption positions such as top (T), hollow (H) and bridge (B) sites on the graphene (Gr) sheet).

in the energy profile presented in Fig. 7.2, the minimum binding energy points refer to the most favorable binding sites for all considered NWs. During the geometrical optimization, the TM chains atoms are kept fixed at a particular position (along  $x$ -,  $y$ -direction), whereas its vertical position along  $z$ -direction (the height from the graphene plane) is relaxed. The C-C bonds near the TM chains atoms are slightly modified and the Gr sheet is slightly bulged towards the carbon atoms. In Table. 7.I, we present the magnetic orders (FM and AF), the wire-carbon interatomic distance  $d_{TM-C}$ , local moments  $\mu$  of TM atom within the WS sphere, binding energy  $E_B$ , and the exchange  $\Delta E_X = E_{AF} - E_{FM}$  between the antiferromagnetic and ferromagnetic states for 3d-TM monoatomic chains. Positive (negative) values of  $\Delta E_X$  correspond to a stable FM (AF) configurations.

Concerning to the binding energy of adsorbed TM chains on the Gr sheet at various sites [see Fig. 7.2 (a)], we conclude that the  $H$  position is energetically favorable one for V, Cr and Mn chains with distance  $d_{TM-C}$  equal to 1.85, 1.94, and 2.02 Å, respectively. Moreover, the top and bridge positions are found to be unstable for Mn chain. The Fe and Co chains prefer  $B$  site adsorption with  $d_{TM-C}$  equal to 1.94, and 2.02 Å, respectively. One notices that  $d_{TM-C}$  increases with increasing number of valence  $d$ -electrons. Our results Fe chains deposited on graphene are in good agreement with

earlier DFT studied [146, 147]. For instance, Zanella *et al.* reported that the most favorable position of Fe chains on the graphene having linear and zigzag geometries is the *B* site [147]. Furthermore, they found that Fe zigzag chains are the most stable on graphene monolayer with FM alignment than the linear one. A very similarly investigation explored that the Fe zigzag wires on the CNT(9,0) exhibit ferromagnetic state [146]. In the case of TM terminated GrNRs, the calculated  $d_{TM-C}$  are 1.98, 1.97, 1.92, 1.85, and 1.82 Å for V, Mn, Cr, Fe, and Co, respectively. Our results are consistent with recent DFT calculations [141, 142]. In general, the binding energies of TM terminated GrNR are higher compared to the deposited on Gr, which indicate that the strong bonding between the chains and GrNR.

As expected the interaction between the TM chains and graphene is crucial for the stability of the magnetic ground-state. In comparison to the freestanding V chain, we notice a significant shift in the exchange energy  $\Delta E_X$ . In the case of V deposited chain on graphene at *H* site, the obtained exchange energy is around  $\Delta E_X \simeq 207$  meV, which is around two times large in magnitude than the energy ( $\Delta E_X \simeq 80$  meV) calculated in the case of freestanding chain at the same NN distance. We observe that deposit V chains strengthen the FM order. In contrast to deposit chain, V terminated GrNR stabilize AF order and the corresponding exchange energy is around  $\Delta E_X \simeq -34$  meV lower than the FM order.

All TM chains, in both cases Gr sheet and terminated GrNR, exhibit a reduction of  $\mu$  as compared to the local moments of freestanding chains as presented in brass. For example, local moment  $\mu$  of V chain is found to be  $2.4 \mu_B$ , which is small in magnitude with respect to the  $\mu = 3.5 \mu_B$  of freestanding chain at the same NN distance. In order to analyze the reduction of  $\mu$ , we calculate the charge transfer between the TM chain and C atoms by integration of the electronic density within the Bader cells [148]. The Bader method takes properly into account the spill-off and interstitial contributions of the charge density. Our results, based on the Bader analysis, show that a significant amount of charge around  $\sim 0.48 |e|$  per V atom is transferred from V chain atoms to the Gr sheet. Similarly, the calculated charge transfer in Fe and Co chain atoms to Gr is  $0.29 |e|$  and  $0.27 |e|$  per atom, respectively. From the Table. 7.I, one notices that the local moments of V and Co chains are notably decreased  $\Delta\mu = 1.1 \mu_B$  and  $\Delta\mu = 0.61 \mu_B$ , respectively, whereas no significant change observes in Mn, Cr, and Fe chains.

In TM chains on Gr sheet and terminated GrNRs, the valence *d*-electron states of TM chain are coupled with the *p*-states of the NN C atoms [see Figs. 7.3 – 7.4], which result the covalent bond between the TM and C atoms. This bonding reduces the number of unpaired *d*-electrons and become a cause of reduction of local moment compared to the freestanding wires [142].

**Table 7.I:** Magnetic orders (FM and AF), distances between the TM chains and carbon atoms of graphene  $d_{TM-C}$ , local moments  $\mu$  of TM atom, binding energy  $E_B$ , and energy difference  $\Delta E_X = E_{AF} - E_{FM}$  between the antiferromagnetic and the ferromagnetic orders. Results are given for the most stable optimized geometry. In parentheses, the local moments of the constitute chains atoms are presented.

3d TM chains	Magnetic order	$d_{TM-C}$ (Å)	$\mu$ ( $\mu_B$ )	$E_B$ (eV/atom)	$\Delta E_X$ (meV/atom)
V/Gr	FM	1.85	2.39(3.43)	<b>-2.265</b>	207
	AF	–	2.19	-2.058	
V/GrNR	FM	1.98	2.59	-4.452	-34.3
	AF	–	2.03	-4.558	
Cr/Gr	FM	1.94	3.52(4.8)	-0.576	-257
	AF	–	3.60	<b>-0.838</b>	
Cr/GrNR	FM	1.97	3.58	-3.259	-360
	AF	–	3.39	-3.619	
Mn/Gr	FM	2.02	3.83(3.95)	-0.981	-4
	AF	–	2.85(3.88)	<b>-0.985</b>	
Mn/GrNR	FM	1.92	3.155	-3.5805	-135
	AF	–	3.19	-3.7163	
Fe/Gr	FM	1.92	2.9(3.21)	-1.783	162
	AF	–	–	-1.621	
B	FM	2.05	2.92	<b>-1.906</b>	251
	AF	–	–	-1.655	
Fe/GrNR	FM	1.85	2.28	-4.611	126
	AF	–	2.23	-4.485	
Co/Gr	FM	1.75	1.55(2.21)	-1.966	106
	AF	–	1.44	-1.860	
B	FM	1.95	1.74	<b>-2.09</b>	173
	AF	–	–	-1.916	
Co/GrNR	FM	1.82	1.273	-4.909	205
	AF	–	0.766	-4.704	

To gain further insight in the magnetic coupling mechanism of deposited chains on the Gr sheet, we calculate the total and partial density of states  $\rho_{i\sigma}^d(\varepsilon)$  of the TM chains and NN carbon atoms as display in Figs. 7.3–7.4. Here, we consider V, Fe and Co chains as prospective examples and investigate the hybridizational effect of graphene on the magnetic properties of TM chains. Moreover, the local  $d$ -DOS of freestanding TM chains at the same NN distance are plotted for the sake of comparison, which are represented by bold blue lines.

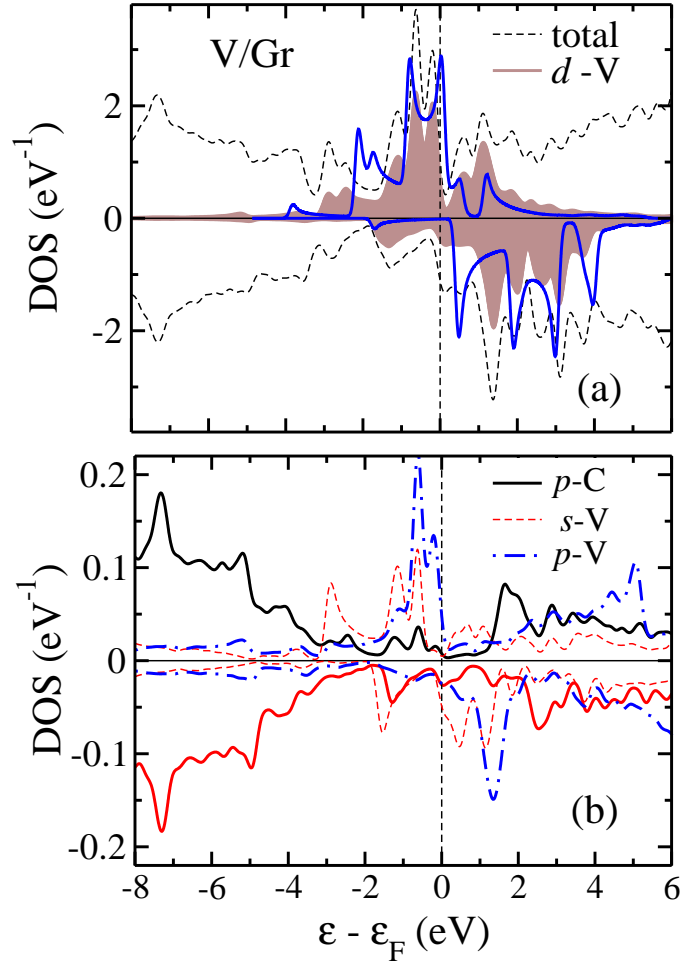


**Figure 7.3:** (a) Total and local  $d$ -electron partial density of states  $\rho_{i\sigma}^d(\varepsilon)$  of a V chain at the most favorable  $H$  position on the graphene having FM order. Shaded areas represent the  $d$ -DOS of the deposited chain, whereas, in comparison, solid blue lines indicate the  $d$ -DOS of the freestanding chain. The blue lines refer to total  $d$ -DOS of free-standing V chain at the same NN distance. (b)  $s$ - and  $p$ -states of a V chain and  $p$ -states of the NN carbon atoms. Results are given for the majority-spin (positive sign) and minority-spin (negative sign) components along the direction of the local magnetic moment  $\vec{\mu}_i$ . The Fermi energy  $\varepsilon_F$  is indicated by the vertical dashed lines.

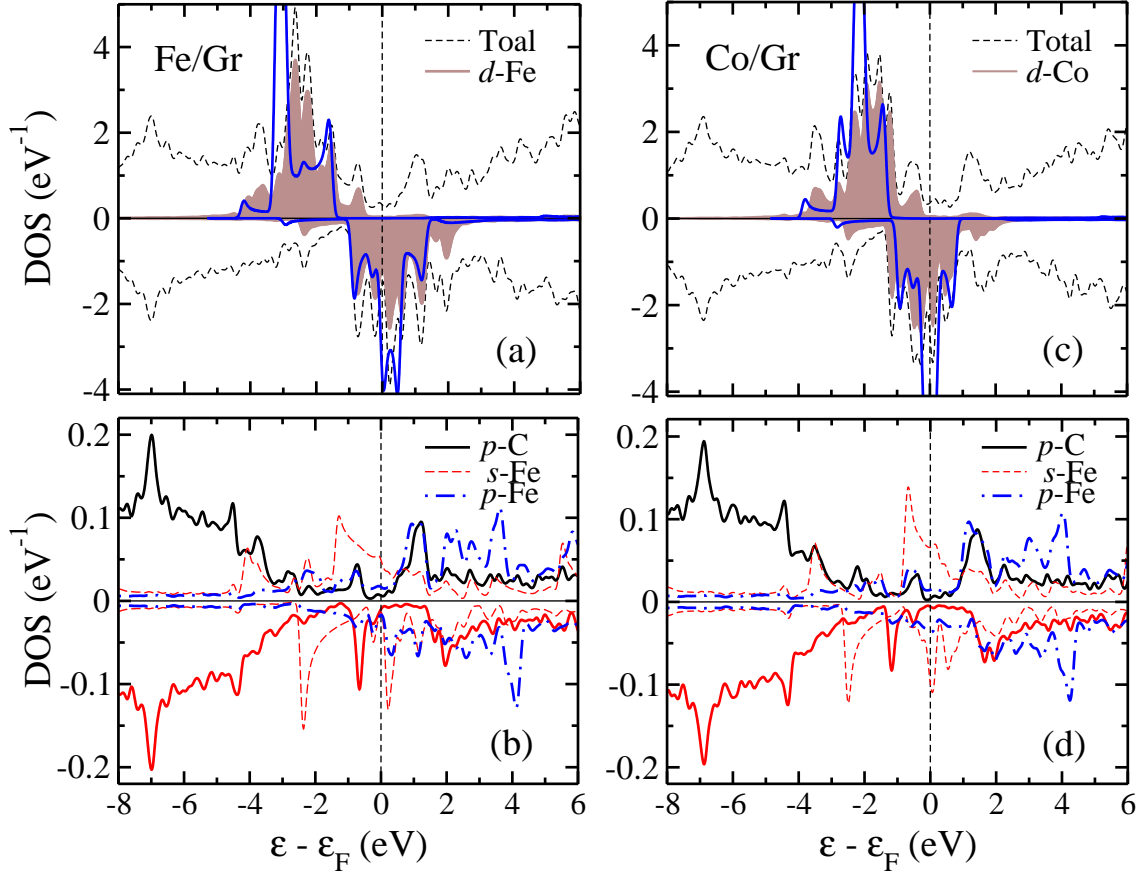


**Figure 7.4:** (a) and (c) Total and local  $d$ -electron partial density of states  $\rho_{i\sigma}^d(\varepsilon)$  of Fe and Co chains at the most favorable  $B$  position on the graphene having FM order, respectively. Shaded areas represent the  $d$ -DOS of the deposited chain, whereas, in comparison, solid blue lines indicate the  $d$ -DOS of the freestanding chain. The blue lines refer to total  $d$ -DOS of free-standing Fe and Co chains at the same NN distance. (b) and (d)  $s$ - and  $p$ -states of Fe and Co chains and  $p$ -states of the NN carbon atoms, respectively. Results are given for the majority-spin (positive sign) and minority-spin (negative sign) components along the direction of the local magnetic moment  $\vec{\mu}_i$ . The Fermi energy  $\varepsilon_F$  is indicated by the vertical dashed lines.

First, in Fig. 7.3 (a)–(b), we analyze the DOS of V chain at the most favorable adsorption  $H$  site along with the  $d$ -DOS of freestanding chains in order to demonstrate the change in the electronic structures after deposition on a Gr sheet. We notice that the majority-spin peak of DOS appears at the position  $\sim -0.61$  eV just below the Fermi energy  $\varepsilon_F$ , which mainly originates from the contribution of the  $s$ -,  $p$ -, and  $d$ -states of V and to a much lesser extent from  $p$ -states of NN carbon atom. Indeed, there is hybridization interaction between these states. We can describe this effect as follows: isolated graphene (carbon atoms) is nonmagnetic and exhibits no exchange

splitting between the orbitals, where it becomes spin-polarized and shows spin-splitting of  $p$ -states around the Fermi energy in the presence of  $3d$  TM impurity [see Fig. 7.3 (b)].

One notices that there is considerable overlapping in the majority states of V and NN C atoms within  $-2.0$  eV to  $\varepsilon_F$  window. This overlapping produces hybridization interaction between these states and reduces the broadening of the orbitals with respect to  $d$ -DOS of free-standing chain atom. Moreover, the hybridization effect between the  $s$ -,  $p$ -, and  $d$ -states of V-chain and  $p$ -states of NN C atoms reduces the exchange splitting, which results the reduction of  $\mu$  around 30% [see Table. 7.I]. We may justify the reduction of local moment by calculating the charge transfer between the chain and carbon sheet atoms. From Bader analysis, we find that a large amount of charge around  $\sim 0.48 |e|$  transfer from V to C atom. Similarly, the total and partial DOS of Fe and Co chains adsorbed at the most favorable  $B$  positions on the Gr sheet are shown in Fig. 7.4 (a)–(d). We notice that the Fe  $d$ -states and NN C  $p$ -states around  $\varepsilon_F$  are overlapped and give rise the phenomena of hybridization. Therefore, NN C atoms close to the chain possess a small amount of negative moments. Its value is around  $-0.035 \mu_B$ . Here, like V chain, we do not find any significant contribution of  $p$ -states of Fe and Co chains in the total DOS.

## 7.4 Spin-density wave spectra

In this section, we are going to investigate the stability of spiral SDWs in the V, Cr, Mn and Fe chains. We find that V, Mn and Fe chains show a tendency to stabilize spin-spiral solution on the Gr sheet and terminated GrNRs, whereas the ground-state magnetic orders of Cr and Co chains are found to be AF and FM, respectively [see Table. 7.I]. All the spin-spiral calculations have been performed by means of GBT as discussed in the above section 7.2.

### 7.4.1 Vanadium chains

In order to determine the ground state magnetic order and its stability, we calculate the magnon dispersion relation of V monoatomic chain deposited on a Gr sheet as shown in the Fig. 7.5 (a). Our results show that the FM arrangement is the most favorable one. For the sake of comparison, we display the dispersion relation of freestanding V chain having the same NN distance  $a = 2.47 \text{ \AA}$ , which exhibits a stable NC spin spiral configurations having  $q_{min} \simeq 0.5\pi/a$  and the corresponding energy is around 33 meV/atom lower than the FM order.

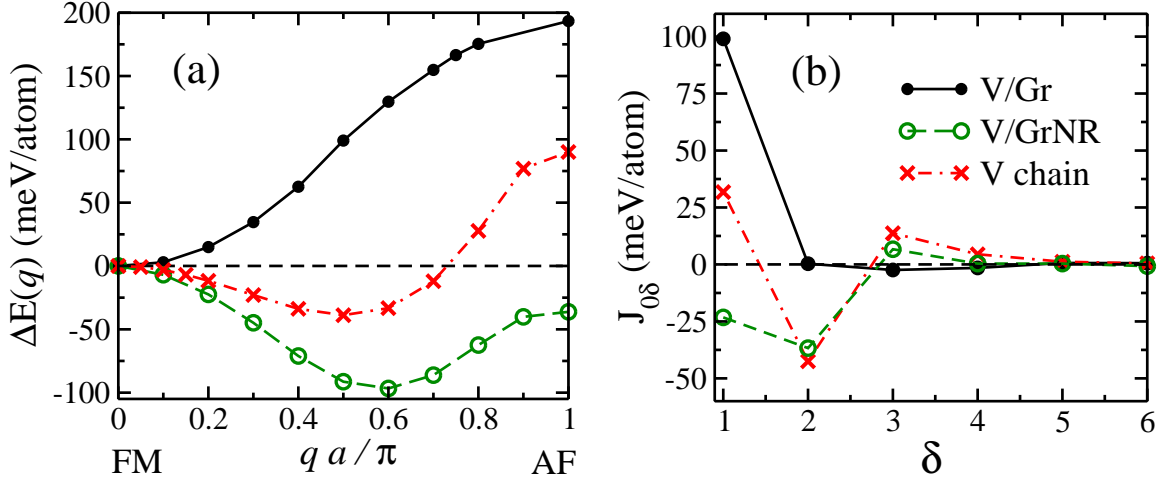


**Figure 7.5:** (a) First principles results for the frozen-magnon dispersion relation  $\Delta E(q) = E(q) - E(0)$  of a V monatomic wire deposited on a graphene sheet as a function of the spin density-wave vector  $q$  (full circles), V-terminated zigzag graphene nanoribbon (GrNR) having a width  $N = 6$  (open circles) [see Fig. 7.1 (b)], and a freestanding V wire (cross) with the lattice parameter of  $a = 2.47 \text{ \AA}$ . The spin spiral wave vector  $q$  is given in unit of  $\pi/a$ . (b) The effective exchange interactions  $J_{0\delta}$  derived from  $\Delta E(q)$  as a function of  $\delta$ .

V-terminated GrNR allows us to analyze the effect of change in coordination numbers and hybridization with the NN carbon atoms on the magnetic orders. Remarkably, we find that the magnetic order of V-terminated GrNR is spin spiral [Fig. 7.1 (b)]. However, the FM solution ( $q = 0$ ) is the less stable one, in context to the V/Gr case. The spin spiral energy minimum occurs at  $q_{min} \simeq 0.6\pi/a$  [open circles in Fig. 7.1 (a)] and the corresponding energy is around 100 meV/atom lower than the FM order and about 70 meV/atom lower than AF order. Thus change in magnetic stability can be quantitatively interpreted as a consequence of the reduction of coordination numbers and hybridization with the C atoms. The local moment is slightly enhanced ( $\mu = 2.6 \mu_B$ ) in comparison with the sheet ( $\mu = 2.4 \mu_B$ ). It remains to be investigated to what extent these results depend on the width  $w$  of the GrNR, since the present calculation only concern  $N = 6$ .

Fig. 7.5 (b) displays the calculated exchange interactions  $J_{0\delta}$  as a function of NN distances  $\delta$ , which were obtained by fitting the corresponding *ab-initio* dispersion relations of Fig. 7.5 (a) to a classical Heisenberg model (3.17). In the case of V/Gr, the magnetic coupling between first NNs is FM ( $J_{01} > 0$ ) and dominates over all other exchange interactions in both freestanding as well as deposited systems. Therefore, the most preferable magnetic ground order is FM. In case of V-terminated GrNR, the first and second NN interactions  $J_{01}$  and  $J_{02}$  are negative showing the tendency to AF coupling, whereas, in contrast,  $J_{03}$  is positive and exhibit FM coupling. Therefore, the NC



spiral configurations are stabilized by the competing interactions within the chains. In other words, the system is said to be magnetically frustrated. Quite surprising results are obtained in both cases: V chains adsorbed on Gr and V-terminated GrNR. In our all considered cases, we find that the magnetic ground state of V chains are known to be quite sensitive to the geometrical structures and interatomic distance [41, 42].

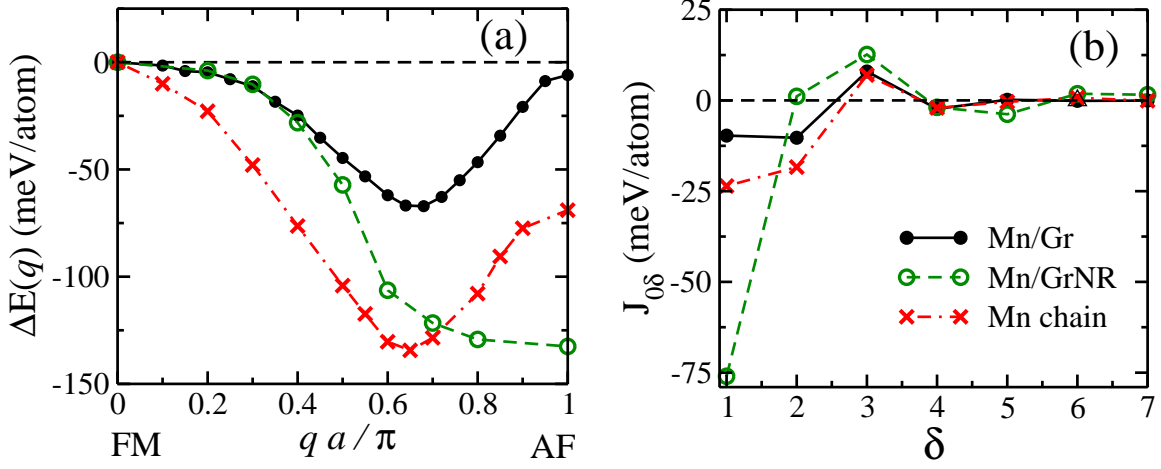
### 7.4.2 Manganese chains

Fig. 7.6 (a) shows the excitation energy spectra of Mn chains for various geometrical structures of graphene such as deposited on a Gr sheet and GrNR. The dispersion curves show that the local energy minimum appears at  $q_{min} \simeq 0.65\pi/a$  for deposited Mn chain on a Gr sheet which is shallower than the case of freestanding wire. The energy difference between the most favorable spin spiral structures and the FM order is found to be approximately 60 meV. A physical quantitative explanation for the occurrence of the energy minimum at finite  $q$  may be found in the band structure or density of states of the Mn chain. We have discussed this situation, briefly, in the section 4.3.2, where the majority- and minority-spin states show remarkable changes in the presence of spin density wave vector  $q$ . In the presence of  $q$ , the majority-spin states below the Fermi energy  $E_F$  move to lower energies and the minority-spin states above  $E_F$  to higher energies. These energy shifting lead to lowering of the total energy. In the case of Mn-terminated GrNR, we do not observe any energy minimum between the FM and AF orders.

The calculated exchange interactions  $J_{0\delta}$  are presented in Fig. 7.6 (b) as a function of NN distance  $\delta$ . We notice that the strength of  $J_{01}$  and  $J_{02}$  reduce in comparison with freestanding wires, but the NC spiral magnetic order still remains most favorable. In the case of Mn-terminated GrNR,  $J_{01}$  is negative and very large in absolute value, and clearly dominates the exchange interactions beyond nearest neighbors. In other words, AF state is the lowest energy among all the explored configurations with respect to different values of  $q$ .

### 7.4.3 Iron chains

The magnon dispersion relations of Fe chains deposited on the Gr sheet and terminated GrNR are shown in the left panel of Fig. 7.7. In order to illustrate the role of the TM-C hybridization on the stability of the magnetic order within the TM chains, we consider different adsorption positions of Fe chain atoms mainly  $T$ ,  $H$ , and  $B$  sites.



**Figure 7.6:** (a) First principles results for the frozen-magnon dispersion relation  $\Delta E(q) = E(q) - E(0)$  of a Mn chain deposited on a graphene sheet as a function of the spin density-wave vector  $q$  (full circles), Mn-terminated zigzag graphene nanoribbon (GrNR) having a width  $N = 6$  (open circles) [see Fig. 7.1 (b)], and a freestanding Mn wire (cross) with the lattice parameter of  $a = 2.47 \text{ \AA}$ . The spin spiral wave vector  $q$  is given in unit of  $\pi/a$ . (b) The effective exchange interactions  $J_{0\delta}$  derived from  $\Delta E(q)$  as a function of  $\delta$ .

In the case of Fe chain deposited at  $T$  position the NC spin arrangements with  $q_{min} \simeq 0.2\pi/a$  are the most stable. However, the energy minimum is very shallow, only about 5 meV/atom below the FM state. In the case of Fe deposited at  $H$  and  $B$  sites, the ground state magnetic solution is found to be FM [see Fig. 7.7 (b-c)]. Remarkably, we observe an energy minimum at  $q_{min} \simeq 0.3\pi/a$  in the case of GrNR, which lies around 8 meV/atom below the FM order. Notice that the wavelength  $\lambda$  of the spin spiral wave is here nearly 8 NN distance, which is substantially shorter than in the deposited case at the  $T$  position of the Gr sheet or in the case of freestanding chains ( $\lambda = 10$ ).

The stability of spiral SDWs when the Fe chain atoms are directly attached to the NN carbon atoms of GrNR seems to be analogous to the situation found in Fe ladders. Indeed, our previous results have demonstrated the formation of spiral SDW in bi-atomic rectangular ladders (two parallel Fe-Fe chains) while keeping the FM couplings in the perpendicular direction [117]. Here, the scenario is similar, since Fe-C pairs repeat along the chains direction. We may further speculate that the  $d$ -orbitals of Fe chain favor the NC magnetism or at least competing interaction couplings  $J_{0\delta}$  when they are directly overlapping in the perpendicular direction.

In the right panel of Fig. 7.7, we present the effective exchange interactions  $J_{0\delta}$  as a function of  $\delta$ th NNs for all considered geometries of Fe wires, which reflect the strength of the interaction between neighboring spins. Notice that the interactions are

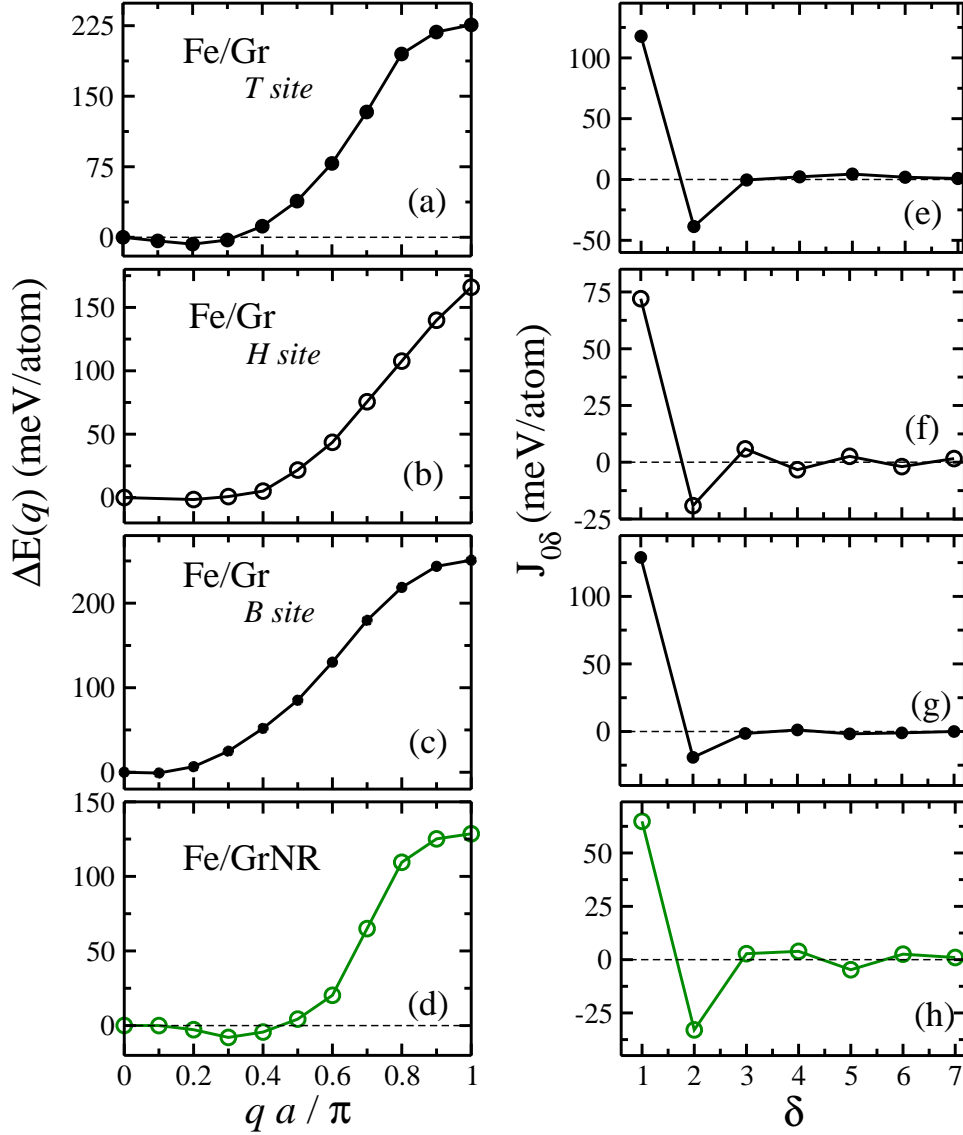


**Figure 7.7:** (a) First principles results for the frozen-magnon dispersion relation  $\Delta E(q) = E(q) - E(0)$  of a Fe chain deposited on a graphene sheet as a function of the spin density-wave vector  $q$  deposited at various positions: (a)  $T$ ,  $H$ , and  $B$  sites on a graphene sheet. Fe-terminated zigzag graphene nanoribbon (GrNR) having a width  $N = 6$  [see Fig. 7.1 (b)]. The spin spiral wave vector  $q$  is given in unit of  $\pi/a$ . (b) The effective exchange interactions  $J_{0\delta}$  derived from  $\Delta E(q)$  as a function of  $\delta$ .

almost negligible beyond the third or farther neighbors. Therefore, we only focus on the dominate couplings  $J_{01}$  and  $J_{02}$ . For instance, in the case of  $H$  and  $B$  sites, the first NN exchange interaction clearly dominates. Therefore, FM arrangements are most favorable one. In contrast, at the  $T$  site and the GrNR, the second NN interaction  $J_{02}$  gains a considerable importance and becomes comparable in magnitude to  $J_{01}$ . Thus, the competing trend between first and second NN interactions seem to be the main factor that stabilizes the spin spiral configuration.

The magnetic phase-diagrams of a classical Heisenberg model have been used to elucidate the results of spin spiral calculations by taking the first-two and the first-three NN exchange interactions  $J_{0\delta}$  into account [see Figs. 4.14 and 4.13]. In practice, these phase-diagrams are useful to predict the complex magnetic orders of freestanding TM chains as well as deposited on graphene. First, we consider the case of Fe chain adsorbed at  $T$  position, the calculated values of  $J_{01}$  and  $J_{02}$  are 116 and  $-39$  meV/atom, respectively. One uses these values in the phase-diagram [see Figure 4.14]. We deduce that Fe has indeed a stable spin spiral configuration. Because, first and second NN interactions satisfy the condition of spin spiral region i.e.,  $4J_{02} < -|J_{01}|$ . Fe chains at  $H$  and  $B$  sites do not fulfil specific criteria for spiral SDWs, therefore in both cases the most favorable solution is FM. Similarly, for Fe terminated GrNR, the calculated  $J_{01} = 64$  and  $J_{02} = -32$  meV/atom values suggest that the possibility to forming a spiral SDW structure is significantly large.

## 7.5 Spin-orbit coupling effects

In this section, we investigate MAE, which is induced by SOC, of TM chains adsorbed on the Gr sheet. Previous investigations have shown that the reduced dimensionality such as 1D and 2D nanostructures deposited on the metal-substrates are often enhanced the MAE as compared to 3D bulk materials [1–3]. Therefore, investigations of the MAEs of the TM chains on the graphene are of interest. The MAE is calculated by the difference of energies

$$\Delta E^{xz} = E^x(\theta = 90, \phi = 0) - E^z(\theta = 0, \phi = 0), \quad (7.1)$$

and

$$\Delta E^{yz} = E^y(\theta = 90, \phi = 0) - E^z(\theta = 0, \phi = 0). \quad (7.2)$$

where  $\theta$  and  $\phi$  refers to the polar and azimuthal angles of the magnetization  $\vec{M}$ . According to the definition of  $\Delta E^{xz}$ , positive (negative) values of  $\Delta E^{xz}$  correspond to as out-of-plane (in-plane) easy axis.

**Table 7.II:** Magnetic order, magnetic anisotropy energies  $\Delta E^{xz}$  and  $\Delta E^{yz}$ , spin and orbital moments of 3d TM chains deposited on the graphene sheet. Results are given only for the chains showing FM ground state order.

3d TM chains	magnetic order	$\Delta E^{xz}$ (meV/atom)	$\Delta E^{yz}$ (meV/atom)	$\mu_s(\mu_B)$		$\mu_L(\mu_B)$	
				$x$	$z$	$x$	$z$
V/Gr H	FM	0.177	–	2.394	2.397	0.021	0.012
Cr/Gr H	FM	-0.21	–	3.513	2.352	0.033	0.015
Mn/Gr H	FM	0.15	–	3.831	3.829	0.012	0.033
Fe/Gr H B	FM	-3.54	0.37	2.901	2.903	0.191	0.098
	FM	-3.61	0.51	2.921	2.917	0.248	0.139
Co/Gr H B	FM	-3.98	-1.875	1.555	1.555	0.208	0.106
	FM	-3.42	-0.360	1.750	1.748	0.198	0.094

In order to provide a local perspective to our results, in Table. 7.II we present the calculated values of  $\Delta E^{xz}$  and  $\Delta E^{yz}$  along with the spin moments  $\mu_s$  and orbital moments  $\mu_L$  determined within the WS spheres for the considered TM chains on the Gr sheet. We find that 3d TM elements up to the half band filling, such as V, Cr and Mn, yield very small value of magnetic anisotropy energy. For example, the calculated anisotropy energies of V, Cr and Mn chains are around 0.177,  $-0.21$ , and 0.15 meV/atom, respectively. These values are however more than 100-times larger than typical bulk values for cubic symmetry. Remarkably, Fe and Co chains at most favorable  $B$  position show relatively larger MAEs as compared to others considered wires. The calculated MAEs are around  $\Delta E^{xz} = -3.61$  meV and  $-3.42$  meV/atom for Fe and Co chains, respectively. Our results show that Fe and Co chains exhibit (in-plane) easy magnetization axis with positive sign. Furthermore, only Fe and Co chains yield considerable orbital magnetic moments of  $\mu_L = 0.24$  and  $0.198 \mu_B$ , respectively. In both cases,  $\mu_L$  is in general larger along the chain direction. It should be, however, noted that the differences among the  $\mu_{Lx}$  and  $\mu_{Lz}$  are very small (e.g.,  $\mu_{Lx} - \mu_{Lz} = 0.108 \mu_B$  for Fe and  $\mu_{Lx} - \mu_{Lz} = 0.104 \mu_B$  for Co chains at the most favorable  $B$  position).

It is interesting to notice that the calculated MAE of TM chains deposited on graphene is quantitatively comparable with a very recent study of 3d TM chains on

the grephyne monolayer [149], Co-dimer on graphene [143, 150] and Fe doped carbon nanotubes [151], and Co chain on Pt(111) [115].

At less favorable  $H$  site for Fe chain, where the TM chain atom is surrounded by six carbon atoms, a reduction of MAE is found due to the increase in coordination number as compared to the  $B$  site. In contrast, Co chain show the opposite trend: the MAE is large at the  $H$  site but the magnetization axis remains in-plane ( $x$ -axis).

## 7.6 Conclusions

In summary, we have studied the structural stability and magnetic coupling of one-dimensional TM (V, Cr, Mn, Fe and Co) chains deposited on a graphene (Gr) sheet and TM-terminated graphene nanoribbons (GrNRs) in the framework of a generalized-gradient approximation to density-functional theory. From the analysis of binding energies, we found that the hexagonal ( $H$ ) centre sites are energetically favorable for V, Cr and Mn chains, whereas the Fe and Co chains prefer the bridge ( $B$ ) adsorption site on the graphene sheet. The electronic structures have been analyzed by calculating the total and local density of states of V, Fe and Co chains at the most favorable adsorption sites on graphene. In V chains, we found that the magnetic coupling mediated by hybridization between the  $s$ -,  $p$ - and  $d$ -states of V chain atoms and the  $p$ -states of the NN carbon atoms which gives rise to robust long range FM order.

The stability of spiral SDWs in TM chains deposited on graphene and terminated GrNRs has been investigated by computing the magnon dispersion relations. Our finding showed that the Mn chains preserve stable spin-spiral structures on the graphene as in the freestanding case, in contrast, V chains favor a FM alignment. In the case of TM terminated GrNRs, V and Fe chains revealed a pronounced tendency to stabilize spiral SDWs at spin wave vector  $q_{min} \simeq 0.6\pi/a$  and  $q_{min} \simeq 0.3\pi/a$ , respectively. In contrast, Cr and Mn chains favor the AF order ( $q = \pi/a$ ). The effective exchange interactions  $J_{\delta 0}$  between the local moments have been derived from the *ab initio* results in the framework of a classical Heisenberg model. The stability of the different magnetic orders has been discussed from a local perspective, in particular as the result of competing first and second NN interactions.

Taking the SOC into account, we showed that Fe and Co chains on the graphene exhibit important spin magnetic moments as well as significant orbital magnetic moments and magnetic anisotropy energy (MAE). The results showed that V, Cr, Mn and Fe chains on the graphene have an out-of-plan easy axis, whereas Co chain has an in-plan easy axis.

# Bibliography

- [1] P. Gambardella, A. Dallmeyer, K. Maiti, M. C. Malagoli, W. Eberhardt, K. Kern, and C. Carbone, *Ferromagnetism in one-dimensional monatomic metal chains*, Nature **416**, 301 (2002).
- [2] P. Gambardella, M. Blanc, H. Brune, K. Kuhnke, and K. Kern, *One-dimensional metal chains on Pt vicinal surfaces*, Phys. Rev. B **61**, 2254 (2000).
- [3] J. Honolka, T. Y. Lee, K. Kuhnke, D. Repetto, V. Sessi, P. Wahl, A. Buchsbaum, P. Varga, S. Gardonio, C. Carbone, S. R. Krishnakumar, P. Gambardella, M. Komelj, R. Singer, M. Fähnle, K. Fauth, G. Schütz, A. Enders, and K. Kern, *Complex magnetic phase in submonolayer Fe stripes on Pt(997)*, Phys. Rev. B **79**, 104430 (2007).
- [4] J. Dorantes-Dávila and G. M. Pastor, *Magnetic anisotropy of one-dimensional nanostructures of transition metals*, Phys. Rev. Lett. **81**, 208 (1998).
- [5] V. S. Stepanyuk, L. Niebergall, R. C. Longo, W. Hergert, and P. Bruno, *Magnetic nanostructures stabilized by surface-state electrons*, Phys. Rev. B **70**, 075414 (2004).
- [6] R. Félix-Medina, J. Dorantes-Dávila, and G. M. Pastor, *Ground-state magnetic properties of  $Co_N$  clusters deposited on Pd(111): spin moments, orbital moments, and magnetic anisotropy*, Phys. Rev. B **67**, 094430 (2003).
- [7] R. N. Igarashi, A. B. Klautau, R. B. Muniz, B. Sanyal, and H. M. Petrilli, *First-principles studies of complex magnetism in Mn nanostructures on the Fe(001) surface*, Phys. Rev. B **85**, 014436 (2012).
- [8] S. Lounis, P. H. Dederichs, and S. Blügel, *Magnetism of nanowires driven by novel even-odd effects*, Phys. Rev. Lett. **101**, 107204 (2008).

- [9] J. Lagoute, C. Nacci, and S. Fölsch, *Doping of monoatomic Cu chain with single Co atom*, Phys. Rev. Lett. **98**, 146804 (2007).
- [10] J. Lagoute, X. Liu, and S. Fölsch, *Electronic properties of straight, kinked, and branched Cu/Cu(111) quantum wires: A low-temperature scanning tunneling microscopy and spectroscopy study*, Phys. Rev. B **74**, 125410 (2006).
- [11] C. Liu, T. Uchihashi, and T. Nakayama, *Self-alignment of Co adatoms on In atomic wires by quasi-one-dimensional electron-gas-mediated interactions*, Phys. Rev. Lett. **101**, 146104 (2008).
- [12] X. D. Ma, D. I. Bazhanov, O. Fruchart, F. Yildiz, T. Yokoyama, M. Przybylski, V. S. Stepanyuk, W. Hergert, and J. Kirschner, *Strain relief guided growth of atomic nanowires in a Cu<sub>3</sub>N-Cu(110) molecular network*, Phys. Rev. Lett. **102**, 205503 (2009).
- [13] G. A. Prinz, *Magnetolectronics*, Science **282**, 1660 (1998).
- [14] S. A. Wolf, D. D. Awschalom, R. A. Buhrman, J. M. Daughton, S. von Molnár, M. L. Roukes, A. Y. Chtchelkanova, and D. M. Treger, *Spintronics: A spin-based electronics vision for the future*, Science **294** 1488 (2001).
- [15] F. Silly, M. Pivetta, M. Ternes, F. Patthey, J. P. Pelz, and W. D. Schneider, *Creation of an atomic superlattice by immersing metallic adatoms in a two-dimensional electron sea*, Phys. Rev. Lett. **92**, 016101 (2004); M. Ternes, C. Weber, M. Pivetta, F. Patthey, J. P. Pelz, T. Giamarchi, F. Mila, and W. D. Schneider, *Scanning-tunneling spectroscopy of surface-state electrons scattered by a slightly disordered two-dimensional dilute "Solid": Ce on Ag(111)*, Phys. Rev. Lett. **93**, 146805 (2004).
- [16] N. D. Mermin and H. Wagner, *Absence of ferromagnetism or antiferromagnetism in one- or two-dimensional isotropic Heisenberg models*, Phys. Rev. Lett. **17**, 1133 (1966).
- [17] P. Bruno, *Absence of spontaneous magnetic order at nonzero temperature in one- and two-dimensional Heisenberg and XY systems with long-range interactions*, Phys. Rev. Lett. **87**, 137203 (2001).
- [18] C. F. Hirjibehedin, C. P. Lutz, and A. J. Heinrich, *Spin coupling in engineered atomic structures*, Science **312**, 1021 (2006).
- [19] R. H. M. Smit, C. Untiedt, A. I. Yanson, and J. M. van Ruitenbeek, *Common origin for surface reconstruction and the formation of chains of metal atoms*, Phys. Rev. Lett. **87**, 266102 (2001).



- [20] O. Fruchart, J.-C. Toussaint, P.-O. Jubert, W. Wernsdorfer, R. Hertel, J. Kirschner, and D. Mailly, *Angular dependence of magnetization switching*, Phys. Rev. B **70**, 172409 (2004); W. Wernsdorfer, N. E. Chakov, and G. Christou, *Determination of the magnetic anisotropy axes of single-molecule magnets*, Phys. Rev. B **70**, 132413 (2004); M. Jamet, W. Wernsdorfer, C. Thirion, V. Dupuis, P. Mélinon, A. Pérez, and D. Mailly, *Magnetic anisotropy in single clusters*, Phys. Rev. B **69**, 024401 (2004).
- [21] P. Ruiz-Díaz, T. R. Dasa, and V. S. Stepanyuk, *Tuning magnetic anisotropy in metallic multilayers by surface charging: An ab initio study*, Phys. Rev. Lett. **110**, 267203 (2013).
- [22] L. M. Sandratskii, *Noncollinear magnetism in itinerant-electron systems: Theory and applications*, Adv. Phys. **47**, 91 (1998).
- [23] E. Sjöstedt and L. Nordström, *Non-collinear full-potential studies of  $\gamma$ -Fe*, Phys. Rev. B **66**, 014447 (2002).
- [24] K. Knöpfle, L. M. Sandratskii, and J. Kübler, *Spin spiral ground state of  $\gamma$ -Fe*, Phys. Rev. B **62**, 5564 (2000).
- [25] R. Hafner, D. Spišák, R. Lorenz, and J. Hafner, *Magnetic ground state of Cr in density-functional theory*, Phys. Rev. B **65**, 184432 (2002).
- [26] R. Lizárraga, L. Nordström, L. Bergqvist, A. Bergman, E. Sjöstedt, P. Mohn, and O. Eriksson, *Conditions for non-collinear instabilities of ferromagnetic materials*, Phys. Rev. Lett. **93**, (2004).
- [27] P. Ferriani, K. von Bergmann, E. Y. Vedmedenko, S. Heinze, M. Bode, M. Heide, G. Bihlmayer, S. Blügel, and R. Wiesendanger, *Atomic-scale spin spiral with a unique rotational sense: Mn monolayer on W(001)*, Phys. Rev. Lett. **101**, 027201 (2008).
- [28] C. Grazioli, D. Alfé, S. R. Krishnakumar, S. S. Gupta, M. Veronese, S. Turchini, N. Bonini, A. D. Corso, D. D. Sarma, S. Baroni, and C. Carbone, *Spin-flop ordering from frustrated ferro- and antiferromagnetic interactions: A combined theoretical and experimental study of a Mn/Fe(100) monolayer*, Phys. Rev. Lett. **95**, 117201 (2005).
- [29] K. Nakamura, N. Mizuno, T. Akiyama, T. Ito, and A. J. Freeman, *Spin-spiral structures in free-standing Fe(110) monolayers*, J. Appl. Phys. **99**, 08N501(2006); T. Shimada, J. Okuno, and T. Kitamura, *Ab initio study of spin-spiral noncollinear magnetism in a free-standing Fe(110) monolayer under in-plane strain*, Phys. Rev. B **85**, 134440 (2012).

- [30] F. Bloch, Phys. **74**, 295 (1932).
- [31] L. Néel, Cahiers de Physique **25**, 1 (1944)
- [32] G. Chen, J. Zhu, A. Quesada, J. Li, A. T. N Diaye, Y. Huo, T. P. Ma, Y. Chen, H. Y. Kwon, C. Won, Z. Q. Qiu, A. K. Schmid, and Y. Z. Wu, *Novel chiral magnetic Domain wall structure in Fe/Ni/Cu(001) films*, Phys. Rev. Lett. **110**, 177204 (2013).
- [33] A. Kubetzka, M. Bode, O. Pietzsch, and R. Wiesendanger, *Spin-polarized scanning tunneling microscopy with antiferromagnetic probe tips*, Phys. Rev. Lett. **88**, 057201 (2002); M. Heide, G. Bihlmayer, and S. Blügel, *Dzyaloshinskii-Moriya interaction accounting for the orientation of magnetic domains in ultrathin films: Fe/W(110)*, Phys. Rev. B **78**, 140403 (2008).
- [34] F. Freimuth, S. Blügel, and Y. Mokrousov, *Berry phase theory of Dzyaloshinskii Moriya interaction and spin orbit torques*, J. Phys.: Condens. Matter **26**, 104202 (2014).
- [35] K.-S. Ryu, L. Thomas, S.-H. Yang, and S. Parkin, *Chiral spin torque at magnetic domain walls*, Nature Nanotechnology **8**, 527 (2013).
- [36] M. Menze, Y. Mokrousov, R. Wieser, J. Bickel, E. Y. Vedmedenko, S. Blügel, S. Heinze, K. von Bergmann, A. Kubetzka and R. Wiesendanger, *Information transfer by vector spin chirality in finite magnetic chains*, Phys. Rev. Lett. **108**, 197204 (2012).
- [37] I. Dzyaloshinskii, *A thermodynamic theory of "Weak" ferromagnetism of antiferromagnets*, J. Phys. Chem. Solids **4**, 24 (1958).
- [38] T. Moriya, *Anisotropic superexchange interaction and weak ferromagnetism*, Phys. Rev. **120**, 91 (1960).
- [39] M. Heide, G. Bihlmayer, and S. Blügel, *Describing Dzyaloshinskii-Moriya spirals from first principles*, Physica B **404**, 2678 (2009).
- [40] M. Zelený, M. Šob, and J. Hafner, *Non-collinear magnetism in manganese nanostructures*, Phys. Rev. B **80**, 144414 (2009).
- [41] M. Saubanère, M. Tanveer, P. Ruiz-Díaz, and G. M. Pastor, *First principles theoretical study of complex magnetic order in transition-metal nanowires*, Phys. Status Solidi B **247**, 2610 (2010).
- [42] J. C. Tung and G. Y. Guo, *Ab initio studies of spin-spiral waves and exchange interactions in 3d transition metal atomic chains*, Phys. Rev. B **83**, 144403 (2011).

- [43] F. Schubert, Y. Mokrousov, P. Ferriani, and S. Heinze, *Non-collinear magnetism in freestanding and supported monatomic Mn chains*, Phys. Rev. B **83**, 165442 (2011).
- [44] Y. Mokrousov, G. Bihlmayer, S. Blügel, and S. Heinze, *Magnetic order and exchange interactions in monoatomic 3d transition-metal chains*, Phys. Rev. B **75**, 104413 (2007).
- [45] Y. Mokrousov, A. Thiess and S. Heinze, *Structurally driven magnetic state transition of biatomic Fe chains on Ir(001)*, Phys. Rev. B **80**, 195420 (2009).
- [46] V. Fálko<sup>1</sup>, *Graphene: Quantum information on chicken wires*, Nature Physics **3**, 151 (2007).
- [47] Y. W. Son, M. L. Cohen, and S. G. Louie, *Half-metallic graphene nanoribbons*, Nature **444**, 347 (2006).
- [48] Y. Zhang, Y.-W. Tan, H. L. Stormer and P. Kim, *Experimental observation of the quantum Hall effect and Berry's phase in graphene*, Nature **438**, 201 (2005)
- [49] A. K. Geim and K. S. Novoselov, *The rise of graphene*, Nat. Mater. **6**, 183 (2007); A. K. Geim, *Graphene: Status and Prospects*, Science **324**, 1530 (2009).
- [50] K. S. Novoselov, A. K. Geim, S. V. Morozov, D. Jiang, M. I. Katsnelson, I. V. Grigorieva, S. V. Dubonos, and A. A. Firsov, *Two-dimensional gas of massless Dirac fermions in graphene*, Nature **438**, 197 (2005).
- [51] H. X. Da, Z. Li, and L. Z. Sun, *Electronic and Magnetic manipulation in graphene absorption by the electric filed*, J. Comput. Theor. Nanosci. C **10**, 515 (2013).
- [52] M. Born and R. Oppenheimer, Ann. Phys. **84**, 457, (1927).
- [53] V. Fock, Z. Phys. **61**, 126, (1930).
- [54] J. Slater, Phys. Rev. **81**, 385, (1951).
- [55] P. Hohenberg and W. Kohn, *Inhomogeneous electron gas*, Phys. Rev. **136**, B864 (1964).
- [56] <http://NEWTon.ex.ac.uk/research/qsystems/people/jenkins/mbody/mbody3.html>
- [57] W. Kohn and L. J. Sham, *Self-Consistent equations including exchange and correlation effects*, Phys. Rev. **140**, A1133 (1965).
- [58] H. Eschrig, *Lectures notes in physics*, Vol **7**, 642, (2004).
- [59] J. Hafner, C. Wolverton and G. Ceder, MRS Bulletin **31**, 659 (2006).

- [60] W. Kohn, 1995, *Density functional theory*, chapter 21, Euroconference on computer simulation in condensed matter physics and chemistry, Italian Physical Society.
- [61] W. Kohn, A. D. Becke, and R. G. Parr, *Density functional theory of electronic structure*, J. Phys. Chem. **100**, 12974, (1996).
- [62] O. Heinonen, M. I. Lubin, and M. D. Johnson, *Ensemble density functional theory of the fractional quantum Hall effect*, Phys. Rev. Lett., **75**, 4110 (1995).
- [63] W. Töws and G. M. Pastor, *Spin-polarized density-matrix functional theory of the single-impurity Anderson model*, Phys. Rev. B **86**, 245123 (2012); W. Töws, M. Saubanère and G. M. Pastor, *Density-matrix functional theory of strongly correlated fermions on lattice models and minimal-basis Hamiltonians*, Theor Chem Acc. **133**, 1422 (2014).
- [64] A. Gross, *Theoretical surface science: A microscopic perspective*, Springer, (2002).
- [65] P. A. M. Dirac, *Note on exchange phenomena in the thomas atom*, Mathematical Proceedings of the Cambridge Philosophical Society, **26**, 376 (1930).
- [66] D. M. Ceperley and B. J. Alder, *Ground state of the electron gas by a stochastic method*, Phys. Rev. Lett. **45**, 566 (1980).
- [67] J. P. Perdew and A. Zunger, *Self-interaction correction to density-functional approximations for many-electron systems*, Phys. Rev. B **23**, 5048, (1981).
- [68] U. von Barth, L. Hedin, *A local exchange-correlation potential for the spin polarized case: I*, J. Phys. C **5**, 1629 (1972).
- [69] M. Payne, M. Teter, D. Allan, T. Arias and J. Joannopoulos, *Iterative minimization techniques for ab initio total-energy calculations: molecular dynamics and conjugate gradients*, Rev. Mod. Phys. **64**, 1045 (1992).
- [70] J. P. Perdew, Y. Wang, *Accurate and simple density functional for the electronic exchange energy: Generalized gradient approximation*, Phys. Rev. B **33**, 8800 (1986).
- [71] Y. Wang and J. P. Perdew, *Correlation hole of the spin-polarized electron gas, with exact small-wave-vector and high-density scaling*, Phys. Rev. B **44**, 13298 (1991); J. P. Perdew and Y. Wang, *Accurate and simple analytic representation of the electron-gas correlation energy*, Phys. Rev. B **45**, 13244 (1992).
- [72] J. P. Perdew, K. Burke, M. Ernzerhof, *Generalized gradient approximation made simple*, Phys. Rev. Lett. **77**, 3865 (1996).

- [73] B. Hammer, L. B. Hansen, J. K. Norskov, *Improved adsorption energetics within density-functional theory using revised Perdew-Burke-Ernzerhof functionals*, Phys. Rev. B **59**, 7413 (1999).
- [74] F. Bloch, Z. Physik **52**, 555 (1928).
- [75] P. E. Blöchl, *Projector augmented-wave method*, Phys. Rev. B, **50**, 17953 (1994).
- [76] H. Hellmann, *Einführung in die Quantenchemie*, Franz Deuticke, Leipzig, (1937).
- [77] R. P. Feynman, *Forces in molecules*, Phys. Rev. **56**, 340 (1939).
- [78] G. Kresse and J. Furthmüller, *Efficient iterative schemes for ab initio total-energy calculations using a plane-wave basis set*, Phys. Rev. B **54**, 11169 (1996); G. Kresse and D. Joubert, *From ultrasoft pseudopotentials to the projector augmented-wave method*, Phys. Rev. B **59**, 1758 (1999).
- [79] H. J. Monkhorst and J. D. Pack, *Special points for Brillouin-zone integrations*, Phys. Rev. B **13**, 5188 (1976).
- [80] D. Hobbs, G. Kresse, and J. Hafner, *Fully unconstrained non-collinear magnetism within the projector augmented-wave method*, Phys. Rev. B **62**, 11556 (2000).
- [81] J. Neugebauer and M. Scheffler, *Adsorbate-substrate and adsorbate-adsorbate interactions of Na and K adlayers on Al(111)*, Phys. Rev. B **46**, 16067 (1992).
- [82] P. Kurz. *Non-collinear magnetism at surfaces and in ultrathin films*, PhD thesis, (2000).
- [83] P. H. Dederichs, S. Blügel, R. Zeller, and H. Akai, *Ground states of constrained systems: Application to cerium impurities*, Phys. Rev. Lett. **53**, 2512 (1984).
- [84] P. D. Haynes and M. C. Payne, *Corrected penalty-functional method for linear-scaling calculations within density-functional theory*, Phys. Rev. B, **59**, 12173, (1999).
- [85] L. M. Sandratskii, *Energy band structure calculations for crystals with spiral magnetic structure*, Phys. Status Solidi B **136**, 167 (1986)
- [86] J. C. Tung and G. Y. Guo, *Systematic ab initio study of the magnetic and electronic properties of all 3d transition metal linear and zigzag nanowires*, Phys. Rev. B **76**, 094413 (2007).
- [87] N. N. Negulyaev, J. Dorantes-Dávila, L. Niebergall, L. Juárez-Reyes, G. M. Pastor and V. S. Stepanyuk, *Alloying route to tailor giant magnetic anisotropy in transition-metal nanowires*, Phys. Rev. B **87**, 054425 (2013).

- [88] P. Bruno, *Tight-binding approach to the orbital magnetic moment and magnetocrystalline anisotropy of transition-metal monolayers*, Phys. Rev. B **39**, 865 (1989).
- [89] S. Zhang, *Spin-dependent surface screening in ferromagnets and magnetic tunnel junctions*, Phys. Rev. Lett. **83**, 640 (1999).
- [90] N. N. Negulyaev, V. S. Stepanyuk, W. Hergert, and J. Kirchner, *Electric field as a switching tool for magnetic states in atomic-scale nanostructures*, Phys. Rev. Lett. **106**, 037202 (2011).
- [91] D. A. Allwood, G. Xiong, C. C. Faulkner, D. Atkinson, D. Petit, and R. P. Cowburn, *Magnetic domain-wall logic*, Science **309**, 1688 (2005).
- [92] A. J. Read, R. J. Needs, K. J. Nash, L. T. Canham, P. D. J. Calcott, and A. Qteish, *First-principles calculations of the electronic properties of silicon quantum wires*, Phys. Rev. Lett. **69**, 1232 (1992).
- [93] L. Hammer, W. Meier, A. Schmidt, and K. Heinz, *Submonolayer iron film growth on reconstructed Ir(100)-(5 × 1)*, Phys. Rev. B **67**, 125422 (2003); L. Hammer, W. Meier, W. Klein, P. Landfried, A. Schmidt, and K. Heinz, *Hydrogen-induced self-organized nanostructuring of the Ir(100) surface*, Phys. Rev. Lett. **91**, 156101 (2003).
- [94] K. Tsukagoshi, B. W. Alphenaar, and H. Ago, *Coherent transport of electron spin in a ferromagnetically contacted carbon nanotube*, Nature **401**, 572 (1999).
- [95] V. Rodrigues, J. Bettini, P. C. Silva, and D. Ugarte, *Evidence for spontaneous spin-polarized transport in magnetic nanowires*, Phys. Rev. Lett. **91**, 096801 (2003).
- [96] M. Marsman and J. Hafner, *Broken symmetries in the crystalline and magnetic structures of gamma-iron*, Phys. Rev. B **66**, 224409 (2002).
- [97] C. Ataca, S. Cahangirov, E. Durgun, Y. R. Jang, and S. Ciraci, *Structural, electronic, and magnetic properties of 3d transition metal monatomic chains: First-principles calculations*, Phys. Rev. B **77**, 214413 (2008).
- [98] M. Bode, M. Heide, K. von Bergmann, K. Ferriani, S. Heinze, G. Bihlmayer, A. Kubetzka, O. Pietzsch, S. Blügel, and R. Wiesendanger, *Chiral magnetic order at surfaces driven by inversion asymmetry*, Nature **447**, 190 (2007).
- [99] O. N. Mryasov, V. A. Gubanov, and A. I. Liechtenstein, *Spiral-spin-density-wave states in fcc iron: Linear-muffin-tin-orbitals band-structure approaching*, Phys. Rev. B **45**, 12330 (1992).

- [100] M. Zelený, M. Šob, and J. Hafner, *Ab initio density functional calculations of ferromagnetism in low-dimensional nanostructures: From nanowires to nanorods*, Phys. Rev. B **79**, 134421 (2009).
- [101] S. A. Wolf, A. Y. Chtchelkanova, and D. M. Treger, *Spintronics: A retrospective and perspective*, IBM J. Res. and Dev. **50**, 101(2006).
- [102] N. N. Negulyaev, V. S. Stepanyuk, L. Niebergall, P. Bruno, W. Hergert, J. Repp, K. H. Rieder, and G. Meyer, *Direct evidence for the effect of quantum confinement of surface-state electrons on atomic diffusion*, Phys. Rev. Lett. **101**, 226601 (2008).
- [103] A. Delin and E. Tosatti, *Magnetic phenomena in 5d transition metal nanowires*, Phys. Rev. B **68**, 144434 (2003).
- [104] H. Ohno, *A window on the future of spintronics*, Nature Materials **9**, 952 (2010).
- [105] E. Y. Tsymbal, *Spintronics: Electric toggling of magnets*, Nature Mater. **11**, 12 (2012).
- [106] D. Chiba, M. Sawiki, Y. Nishitani, Y. Nakatani, F. Matsukura, and H. Ohno, *Magnetization vector manipulation by electric fields*, Nature **455**, 515 (2008).
- [107] S. J. Gamble, M. H. Burkhardt, A. Kashuba, R. Allenspach, S. S. P. Parkin, H. C. Siegmann, and J. Stöhr, *Electric field induced magnetic anisotropy in a ferromagnet*, Phys. Rev. Lett. **102**, 217201 (2009).
- [108] K. Nakamura, T. Ito, M. Weinert, and A. J. Freeman, *Role of an interfacial FeO layer in the electric-field-driven switching of magnetocrystalline anisotropy at the Fe/MgO interface*, Phys. Rev. Lett. **102**, 187201 (2009).
- [109] M. Tsujikawa and T. Oda, *Finite electric field effects in the large perpendicular magnetic anisotropy surface Pt/Fe/Pt(001): A first-principles study*, Phys. Rev. Lett. **102**, 247203 (2009).
- [110] P. Borisov, A. Hochstrat, X. Chen, W. Kleemann, and C. Binek, *Magnetoelectric switching of exchange bias*, Phys. Rev. Lett. **94**, 117203 (2005).
- [111] T. Maruyama, Y. Shiota, T. Nozaki, K. Ohnta, N. Toda, M. Mizuguchi, A. A. Tulapurkar, T. Shinjo, M. Shiraishi, S. Mizukami, Y. Ando, and Y. Suzuki, *Large voltage-induced magnetic anisotropy change in a few atomic layers of iron*, Nature Nanotechnol. **4**, 158 (2009).
- [112] Y. Shiota, T. Nozak, F. Bonell, S. Murakami, T. Shinjo, and Y. Suzuki, *Induction of coherent magnetization switching in a few atomic layers of FeCo using voltage pulses*, Nature Mater. **11**, 39 (2012).

- [113] H. Ohno, D. Chiba, F. Matsukura, T. Ohno, E. Abe, T. Dietl, T. Ohno, and K. Ohtani, *Electric-field control of ferromagnetism*, Nature **408**, 944 (2000).
- [114] L. Juárez-Reyes, V. S. Stepanyuk and G. M. Pastor, *Electric-field-modulated exchange coupling within and between magnetic clusters on metal surfaces: Mn dimers on Cu(111)*, J. Phys.: Condens. Matter **26**, 176003 (2014).
- [115] T. R. Dasa, P. A. Ignatiev, and V. S. Stepanyuk, *Effect of the electric field on magnetic properties of linear chains on a Pt(111) surface*, Phys. Rev. B **85**, 205447 (2013).
- [116] W. Töws and G. M. Pastor, *Theoretical study of the temperature dependence of the magnon dispersion relation in transition-metal wires and monolayers*, Phys. Rev. B **86**, 054443 (2012).
- [117] M. Tanveer, P. Ruiz-Díaz, and G. M. Pastor, *Environment-dependent non-collinear magnetic orders and spin-wave spectra of Fe chains and stripes*, Phys. Rev. B **87**, 075426 (2013).
- [118] M. Tsujikawa and T. Oda, *Electronic structure and magnetic anisotropy of a constrained Fe chain in an electric field*, J. Phys.: Condens. Matter **21**, 064213 (2009).
- [119] C. G. Duan, J. P. Velev, R. F. Sabirianov, Z. Q. Zhu, J. H. Chu, S. S. Jaswal, and E. Y. Tsymbal, *Surface magnetoelectric effect in ferromagnetic metal films*, Phys. Rev. Lett. **101**, 137201 (2008).
- [120] N. Tombros, C. Jozsa, M. Popinciuc, H. T. Jonkman, and B. J. van Wees, *Electronic spin transport and spin precession in single graphene layers at room temperature*, Nature (London) **448**, 571 (2007).
- [121] F. Schedin, A. K. Geim, S. V. Morozov, E. W. Hill, P. Blake, M. I. Katsnelson, and K. S. Novoselov, *Detection of individual gas molecules adsorbed on graphene*, Nature Mater. **6**, 652 (2007).
- [122] J. Berashevich and T. Chakraborty, *Tunable band gap and magnetic ordering by adsorption of molecules on graphene*, Phys. Rev. B **80**, 033404 (2009).
- [123] J. B. Oostinga, H. B. Heersche, X. Liu, A. F. Morpurgo, and L. M. K. Vander-sypen, *Gate-induced insulating state in bilayer graphene devices*, Nature Mater. **7**, 151 (2008)
- [124] T. Ohta, A. Bostwick, T. Seyller, K. Horn, and E. Rotenberg, *Controlling the electronic structure of bilayer graphene*, Science **313**, 951 (2006).



- [125] S. Y. Zhou, G.-H. Gweon, A. V. Fedorov, P. N. First, W. A. de Heer, D.-H. Lee, F. Guinea, A. H. Castro Neto, and A. Lanzara, *Substrate-induced bandgap opening in epitaxial graphene*, Nature Mater. **6**, 770 (2007).
- [126] G. Giovannetti, P. A. Khomyakov, G. Brocks, V. M. Karpan, J. van den Brink, and P. J. Kelly, *Doping graphene with metal contacts*, Phys. Rev. Lett. **101**, 026803 (2008).
- [127] F. M. Hu, T. Ma, H.-Q. Lin, and J. E. Gubernatis, *Magnetic impurities in graphene*, Phys. Rev. B **84**, 075414 (2011).
- [128] K. T. Chan, J. B. Neaton, and M. L. Cohen, *First-principles study of metal adatom adsorption on graphene*, Phys. Rev. B **77**, 235430 (2008).
- [129] T. Eelbo, M. Waśniowska, M. Gyamfi, S. Forti, U. Starke, and R. Wiesendanger, *Influence of the degree of decoupling of graphene on the properties of transition metal adatoms*, Phys. Rev. B **87**, 205443 (2013).
- [130] T. Eelbo, M. Waśniowska, P. Thakur, M. Gyamfi, B. Sachs, T. O. Wehling, S. Forti, U. Starke, C. Tieg, A. I. Lichtenstein, and R. Wiesendanger, *Adatoms and clusters of 3d transition metals on graphene: Electronic and magnetic configurations*, Phys. Rev. Lett. **110**, 136804 (2013).
- [131] F. Donati, Q. Dubout, G. Autés, F. Patthey, F. Calleja, P. Gambardella, O. V. Yazyev, and H. Brune, *Magnetic moment and anisotropy of individual Co atoms on graphene*, Phys. Rev. Lett. **111**, 236801 (2013).
- [132] A. V. Krasheninnikov, P. O. Lehtinen, A. S. Foster, P. Pyykkö, and R. M. Nieminen, *Embedding transition-metal atoms in graphene: Structure, bonding, and magnetism*, Phys. Rev. Lett. **102**, 126807 (2009).
- [133] C. Cao, M. Wu, J. Jiang, and H.-P. Chen, *Transition metal adatom and dimer adsorbed on graphene: Induced magnetization and electronic structures*, Phys. Rev. **81**, 205424 (2010).
- [134] Y. Wang, V. W. Brar, A. V. Shytov, Q. Wu, W. Regan, H. Z. Tsai, A. Zettl, L. S. Levitov, and M. F. Crommie, *Mapping Dirac quasiparticles near a single coulomb impurity on graphene*, Nature Phys. **8**, 653 (2012).
- [135] D. Krychowski, J. Kaczkowski, and S. Lipinski, *Kondo effect of a cobalt adatom on a zigzag graphene nanoribbons*, Phys. Rev. B **89**, 035424 (2014).
- [136] P. O. Lehtinen, A. S. Foster, Y. Ma, A. V. Krasheninnikov, and R. M. Nieminen, *Irradiation-induced magnetism in graphite: A density functional study*, Phys. Rev. Lett. **93**, 187202 (2004).

- [137] J. J. Palacios, J. Fernández-Rossier, and L. Brey, *Vacancy-induced magnetism in graphene and graphene ribbons*, Phys. Rev. B **77**, 195428 (2008).
- [138] J. H. Chen, L. Li, W. G. Cullen, E. D. Williams, and M. S. Fuhrer, *Tunable Kondo effect in graphene with defects*, Nature Phys. **7**, 535 (2011).
- [139] M. Fujita, K. Wakabayashi, K. Nakada, and K. Kusakabe, *Peculiar localized state at zigzag graphite edge*, J. Phys. Soc. Jpn. **65**, 1920 (1996).
- [140] K. Nakada, M. Fujita, G. Dresselhaus, and M. S. Dresselhaus, *Edge state in graphene ribbons: Nanometer size effect and edge shape dependence*, Phys. Rev. B **54**, 17954 (1996).
- [141] Y. Wang and H.-P. Cheng, *Interedge magnetic coupling in transition-metal terminated graphene nanoribbons*, Phys. Rev. B **83**, 113402 (2011).
- [142] Y. Wang, C. Cao, and H.-P. Cheng, *Metal-terminated graphene nanoribbons*, Phys. Rev. **82**, 205429 (2010).
- [143] P. Bloński and J. Hafner, *Magnetic anisotropy of transition-metal dimers: Density functional calculations*, Phys. Rev. B **79**, 224418 (2009).
- [144] T. O. Strandberg, C. M. Canali, and A. H. MacDonald, *Transition-metal dimers and physical limits on magnetic anisotropy*, Nat. Mater. **6**, 648 (2007); T. O. Strandberg, C. M. Canali, and A. H. MacDonald, *Calculation of chern number spin Hamiltonians for magnetic nano-clusters by DFT methods*, Phys. Rev. B **77**, 174416 (2008); D. Fritsch, K. Koepf, M. Richter, and H. Eschrig, *Transition metal dimers as potential molecular magnets: A challenge to computational chemistry*, J. Comput. Chem. **29**, 2210 (2008).
- [145] R. Félix-Medina, J. Dorantes-Dávila, and G. M. Pastor, *Spin moments, orbital moments, and magnetic anisotropy of finite-length Co wires deposited on Pd(110)*, New J. Phys. **4**, 100 (2002).
- [146] H. Shiroishi, T. Oda, H. Sakashita, and N. Fujima, *Structure and magnetism in carbon nanotubes including magnetic wires*, Eur. Phys. J. D **43**, 129 (2007); M. Shiroishi, T. Oda, and N. Fujima, *Electronic structure and magnetism of Fe wire in carbon nanotubes*, J. Magn. Mater. **310**, 1640 (2007).
- [147] I. Zanella, S. B. Fagan, R. Mota, and A. Fazzio, *Electronic and magnetic properties of Ti and Fe on graphene*, J. Phys. Chem. C **112**, (2008).
- [148] R. Bader, *Atoms in molecules: A quantum theory*, Oxford University Press, New York, (1990).

- [149] J. He, P. Zhou, N. Jiao, S. Y. Ma, K. W. Zhang, R. Z. Wang, and L. Z. Sun, *Magnetic exchange coupling and anisotropy of 3d transition-metal nanowires on graphene*, Sci. reports **4**, 4014 (2014).
- [150] R. A. Xiao, D. Fritsch, M. D. Kuzmín, K. Koepernik, H. Eschrig, M. Richter, K. Vietze, and G. Seifert, *Co dimers on hexagonal carbon rings proposed as subnanometer magnetic storage bits*, Phys. Rev. Lett. **103**, 187201 (2009).
- [151] X. Zou, G. Zhou, J. Li, B. Yan, J. Wu, B.-L. Gu, and W. Duan, *Preparing spin-polarized scanning tunneling microscope probes on capped carbon nanotubes by Fe doping: A first-principles study*, Appl. Phys. Lett. **94**, 193106 (2009).
- [152] E. Durgun and S. Ciraci, *Spin-dependent electronic structure of transition-metal atomic chains adsorbed on single-wall carbon nanotubes*, Phys. Rev. B **74**, 125404 (2006).
- [153] L. Yu, W.-X. Li X. Pan and X. Bao, *In and out-dependent interactions of Iron with carbon nanotubes*, J. Phys. Chem. C **116**, 16461 (2012).



---

## Glossary

### Abbreviations

1D	One-dimensional
2D	Two-dimensional
AF	Antiferromagnetic
APW	Augmented plane wave method
ANC	Alternative noncollinear
BZ	Brillouin zone
DFT	Density functional theory
EF	Electric Field
Eq.	Equation
FM	Ferromagnetic
GGA	Generalized gradient approximation
GrNRs	Graphene nanoribbons
HK	Hohenberg-Kohn
IBZ	Irreducible Brillouin zone
KS	Kohn-Sham
LDOS	Local density of states
LC	Linear chain
LDA	Local density approximation
NC	Noncollinear
NW	Nanowire
NN	Nearest neighbor
MAE	Magnetic anisotropy energy
PNC	Periodic noncollinear

Ref.	Reference
RL	Ladder
SDW	Spin-density wave
STM	Scanning tunneling microscope
STS	Scanning tunneling spectroscopy
SOC	Spin-orbit coupling
TM	Transition-metal
VASP	Vienna <i>ab-initio</i> simulation package
XC	Exchange-correlation
XMCD	X-ray magnetic circular dichroism
ZZ	Zig-zag

## Physical constants

$\mu_B$	Bohr magneton
$k_B$	Boltmann constant
$e$	Electron charge
$\hbar$	Reduced Planck constant

## Symbols

$\vec{R}$	Atomic position
$\vec{E}$	Electric field
$J_{ij}$	Exchange interaction
$\varepsilon_F$	Fermi energy
$a$	Interatomic distance
$\vec{\mu}$	Magnetic moment
$N_a$	Number of atoms
$\vec{q}$	Spin-wave vector
$\sigma$	Spin index
$\hat{e}$	Unit vector

---

## List of publications

- *First principles theoretical study of complex magnetic order in transition metal nanowires*  
M. Saubanère, M. Tanveer, P. Ruiz-Díaz, and G. M. Pastor  
Phys. Status Solidi B **247**, 2610 (2010).
- *Environment-dependent non-collinear magnetic orders and spin-wave spectra in iron chains and stripes*  
M. Tanveer, P. Ruiz-Díaz, and G. M. Pastor  
Phys. Rev. B **87**, 075426 (2013).
- *Tuning spin-density waves in nanowires by means of external electric fields*  
M. Tanveer and G. M. Pastor  
(To be submitted to PRB).
- *Magnetic Exchange Coupling in 3d Transition Metal Nanowires on Graphene*  
M. Tanveer and G. M. Pastor  
(To be submitted to PRB).
- *Electronic and magnetic properties of spiral spin-density-wave states in transition-metal chains*  
M. Tanveer, P. Ruiz-Díaz and G. M. Pastor  
(To be submitted to J. Phys.: Condens. Matter).

## Presentations and conferences

- *Introduction to the programming and usage of the supercomputing resources in Jülich*, Jülich Supercomputing Centre (JSC), Forschungszentrum Jülich, Germany (10 – 11 August, 2009).
- *Deutsche Physikalische Gesellschaft (DPG) Spring Meeting*, Regensburg, Germany (22 – 26 March, 2010) [poster].
- *Stability of Spin-spiral waves in free-standing 3d transition-metal (TM) monoatomic wires*, University of Kassel, Germany (21 Jun, 2011) [talk].
- *Deutsche Physikalische Gesellschaft (DPG) Spring Meeting*, Berlin, Germany (26 – 30 March, 2012) [talk].

- *Stability of noncollinear magnetism in 3d transition metal nanowires*, University of Kassel, Germany (05 Jun, 2012) [talk].
- 62<sup>th</sup> *Lindau Noble Laureate Meeting (Physics)*, Lindau, Germany (1 – 6 July, 2012) [talk].
- *Center for Interdisciplinary Nanostructure Science and Technology (CINSat) Spring Meeting*, Friedrichroda, Germany (28 Feb – 02 March, 2013) [poster].



## Curriculum vitae

### Personal information

Name	Muhammad Tanveer
Nationality	Pakistani
Place of birth	Okara
Email	tanvir_phy@yahoo.com
Contact	Universtät Kassel, Institut für Theoretische Physik, Heinrich Plett Strae 40, D-34132 Kassel, Germany.

